

TRANSPORT AND RESONANCES IN KICKED BOSE-EINSTEIN  
CONDENSATES

By

ISHAN TALUKDAR

Master of Science  
University of Delhi  
Delhi, India  
2003

Master of Science  
Oklahoma State University  
Stillwater, Oklahoma, USA  
2006

Submitted to the Faculty of the  
Graduate College of  
Oklahoma State University  
in partial fulfillment of  
the requirements for  
the Degree of  
DOCTOR OF PHILOSOPHY  
December, 2010

COPYRIGHT ©

By

ISHAN TALUKDAR

December, 2010

TRANSPORT AND RESONANCES IN KICKED BOSE-EINSTEIN  
CONDENSATES

Dissertation Approved:

Dr. Gil S. Summy

---

Dissertation Advisor

Dr. Girish S. Agarwal

---

Dr. John W. Mintmire

---

Dr. Nicholas F. Materer

---

Dr. Mark E. Payton

Dean of the Graduate College

## ACKNOWLEDGMENTS

I would like to begin by expressing my gratitude to my advisor Gil Summy. Gil has taught me much of what I know of this field today, patiently answering my questions and showing me new, creative ways of looking at scientific problems. His enthusiasm and words of encouragement guided me during the difficult times and will remain invaluable in the years to come. In the lab it has always amazed and inspired me how Gil finds a way to simply make things work.

I would like to thank my committee members, Prof. G. Agarwal, Prof. J. Mintmire, and Prof. N. Materer for their time, help and advice.

Without the love and continued support from my parents Kanteswar and Mohini Talukdar, I would not be where I am today. They showed me the importance of aiming high and working hard. I wish to thank them and my sister Shruti for her cheer and motivation.

I have had the good fortune of meeting some incredible people during my stay at OSU. Peyman had defended his thesis when I joined the group. An exceptional physicist and a great individual, he has remained a good friend and mentor throughout these years. Ghazal cheerfully introduced me to the experiments and helped me adjust to my new lab. Vijay, who was my room-mate as well, explained the nitty gritty of the experiments and gladly fielded my incessant questions. It has been a nice experience working with Raj who joined our lab later and brought a refreshing way of doing things.

Part of my physics family were our department staff members, Susan, Cindy, Stephanie, Danyelle, and recently Tamara. Besides their helpful and supportive atti-



tude, they are among the nicest people I have met in my life. Melissa has been a kind and understanding lab-coordinator. Thanks also to Warren, our technical support. He is a one man army, handling all kinds of requests from the students. Mike and his staff at the machine shop have the special ability to bring any model design to life, only better.

I would like to thank the physics faculty for providing me with the knowledge and guidance that has helped me pursue my research. Especially, I wish to thank Prof. Paul Westhaus, our former graduate coordinator and Prof. R. Hauenstein, our current graduate coordinator for their support during my years at the physics department.

Thanks are also due to my former professors at the University of Delhi, Prof. Seshadri and Prof. Annapoorni for having shown me the path of research.

Finally, I would like to express my thanks to all my friends at Stillwater, especially DJ (Deok Jin Yu), Prem and Amit.

## TABLE OF CONTENTS

Chapter	Page
<b>1 INTRODUCTION</b>	<b>1</b>
1.1 Organization . . . . .	3
<b>2 Delta-Kicked Rotor : Theory and Experiments</b>	<b>5</b>
2.1 Classical kicked rotor . . . . .	5
2.2 Atom optics $\delta$ -kicked rotor . . . . .	6
2.2.1 Quantum resonances and anti-resonances . . . . .	9
2.2.2 Dynamical Localization . . . . .	10
2.2.3 Quantum Transport . . . . .	12
2.3 Bose-Einstein Condensation . . . . .	15
2.3.1 Laser Cooling and Trapping . . . . .	15
2.3.2 Limits of laser cooling . . . . .	17
2.3.3 Evaporative cooling . . . . .	17
2.4 Experimental Configuration . . . . .	19
<b>3 Quantum transport with a kicked BEC</b>	<b>27</b>
3.1 High-order resonances of a quantum accelerator mode . . . . .	27
3.1.1 Rephasing theory . . . . .	27
3.1.2 $\epsilon$ -classical theory . . . . .	28
3.1.3 Experiment . . . . .	33
3.2 A quantum ratchet . . . . .	40
3.2.1 Experiment . . . . .	42

<b>4</b>	<b>Sub-Fourier resonances of the kicked rotor</b>	<b>48</b>
4.1	A fidelity measurement on the QDKR . . . . .	49
4.1.1	Effect of ‘gravity’ . . . . .	50
4.2	Experimental Configuration and Results . . . . .	53
<b>5</b>	<b>Photoassociation of a <math>^{87}\text{Rb}</math> BEC</b>	<b>64</b>
5.1	Photoassociative spectroscopy . . . . .	65
5.2	Ultracold Collisions . . . . .	68
5.3	Scattering length and Feshbach Resonances . . . . .	69
5.3.1	Optical Feshbach Resonance . . . . .	73
5.4	Experiment and Results . . . . .	75
5.5	Conclusion and Outlook . . . . .	82
<b>6</b>	<b>CONCLUSIONS</b>	<b>91</b>
6.0.1	Summary . . . . .	91
6.0.2	Future work . . . . .	92
	<b>BIBLIOGRAPHY</b>	<b>94</b>
<b>A</b>	<b>Publications</b>	<b>108</b>

## LIST OF FIGURES

Figure		Page
2.1	Classical $\delta$ -kicked rotor phase space for different kick strengths $K$ . Onset of stochastic regions can be seen in (c) while (d) is predominantly chaotic. . . . .	7
2.2	(a) and (b), A quadratic growth in the mean energy at a quantum resonance at the Talbot time, and (c) and (d), an oscillatory mean energy at an anti-resonance at $T = T_{1/2}$ . . . . .	11
2.3	Quantum suppression of classical chaos. Simulation of the QDKR near the Talbot time with $\phi_d=3.0$ shows the onset of dynamical localization after six kicks. Also shown is the classical momentum diffusion (solid line). . . . .	13
2.4	Evolution of thermodynamic quantities as a function of the trap truncation parameter. . . . .	20
2.5	A schematic of the rubidium D2 transition. . . . .	22
2.6	Set-up of the optical table for the BEC experiments. Not shown is a final 80 MHz AOM for both the MOT Slave beams before the optical fibers. . . . .	23
2.7	Alignment of beams for the Magneto-Optic Trap and the FORT inside the vacuum chamber. . . . .	26

3.1	Phase space of quantum accelerator modes generated by the map of (3.22) for $\tau = 5.744$ and $\phi_d = 1.4$ . Mode (a) with $(\mathbf{p}, j) = (1, 0)$ for $\eta = 2.1459$ . is a primary QAM. Higher order modes are seen in (b) with $(\mathbf{p}, j) = (2, 1)$ , $\eta = 2.766$ , and (c) $(\mathbf{p}, j) = (5, 1)$ , $\eta = 4.1801$ . . . . .	32
3.2	Set-up for the kicking experiments. Two counterpropagating beams formed the standing wave oriented at an angle of $52^\circ$ to the vertical. AOM <sub>2</sub> was driven by an RF signal with a fixed frequency, $\omega/2\pi = 40\text{MHz}$ . . . . .	34
3.3	Quantum accelerator modes at (a) $T=22.68 \mu s$ close to $(2/3)T_{1/2}$ , (b) $T=17.1 \mu s$ which is close to $(1/2)T_{1/2}$ , and (c) $T=72.4 \mu s$ close to $2T_{1/2}$ . a value of $g'=6 \text{ ms}^{-2}$ was used in these scans. The arrows in (a) and (b) show orders separated by $b\hbar G$ which participate in the QAMs. Dashed lines correspond to the $\epsilon$ -classical theory of Eq. (3.27) . . . . .	36
3.4	Horizontally stacked momentum distributions across (a) $(1/2)T_{1/2}$ for 40 kicks, $\phi_d = 1.4$ and effective acceleration $g' = 6 \text{ ms}^{-2}$ ; and (b) $(1/3)T_{1/2}$ for 30 kicks, $\phi_d = 1.8$ , and $g'=4.5 \text{ ms}^{-2}$ . The dashed curve is a fit to the theory in Eq. (3.27) . . . . .	38
3.5	Initial momentum scans for QAMs near (a) $(1/2)T_{1/2}$ ( $T=17.1 \mu s$ ) for 30 kicks and $g'=6 \text{ ms}^{-2}$ ; and (b) $(2/3)T_{1/2}$ ( $T=22.53 \mu s$ ) with 40 kicks and $g'=4.5 \text{ ms}^{-2}$ . The dashes indicate QAMs at the resonant $\beta$ . . . . .	39
3.6	Dependence of the mean momentum of the quantum ratchet on the offset angle $\gamma$ for 5 kicks and $\beta = 0.5$ . The dashed and solid lines represent Eqs. (3.33) and (3.36) respectively. The inset shows the offset $\gamma$ created between the symmetry centers of the initial distribution (blue curve) and the kicking potential $V$ (red curve). . . . .	43

3.7	The ratchet effect. This time of flight image shows growth of mean momentum with each standing wave pulse applied with a period of $T_{1/2}$ and a maximum offset ( $\gamma = \pi/2$ ) between the standing wave and the initial state. . . . .	44
3.8	Mean momentum as a function of kicks. The data and error bars are from experiments with $\phi_d = 1.4, \gamma = \pi/s$ and $\beta = 0.5$ . The solid line is Eq. (3.33) while the dashed line corresponds to Eq. (3.36). . . . .	45
3.9	Change in mean momentum vs the quasimomentum $\beta$ for $\phi_d = 1.4$ and (a) $\gamma = -\pi/2$ , (b) $\gamma = \pi/2$ . Shown are the fits of Eqs. (3.33), dashed line and (3.36), solid line respectively to the experimental data (filled circles). . . . .	47
4.1	Momentum distributions of a sequence of 8 kicks of strength $\phi_d$ followed by a final $\pi$ -phase reversed kick of strength $N\phi_d$ , with a time period equal to the Talbot time $106.5\mu s$ . . . . .	54
4.2	(a) Horizontally stacked time-of-flight images of a fidelity scan around the Talbot time. Each TOF image was the result of 5 kicks with $\phi_d = 0.8$ followed by a $\pi$ -phase shifted kick at $5\phi_d$ . (b) Mean energy distribution of the 5 kick rotor with the same $\phi_d$ . (c) The measured fidelity distribution (circles) from (a). The mean energy of the scan in (b) is shown by the triangles. Numerical simulations of the experiment for a condensate with momentum width $0.06 \hbar G$ are also plotted for fidelity (blue-dashed line) and mean energy (red-solid line). The amplitude and offset of the simulated fidelity were adjusted to account for the experimentally imperfect reversal phase. . . . .	56

4.3	Experimentally measured fidelity (circles) and mean energy (triangles) widths (FWHM) as a function of (a) the number of pulses, and (b) the kicking strength $\tilde{\phi}_d$ scaled to $\phi_d$ of the first data point. In (a), the data are for 4 to 9 kicks in units normalized to the 4 <sup>th</sup> kick. Error bars in (a) are over three sets of experiments and in (b) $1\sigma$ of a Gaussian fit to the distributions. Dashed lines are linear fits to the data. Stars are numerical simulations for an initial state with a momentum width of $0.06\hbar G$ . . . . .	58
4.4	Variation of the fidelity peak width around $\beta=0$ as a function of kick number $N(N+1)_s = N(N+1)/20$ scaled to the 4 <sup>th</sup> kick. The straight line is a linear fit to the data with a slope of $-0.92 \pm 0.06$ . Error bars as in Fig. 2(b). . . . .	59
4.5	(a) Momentum width of the reversed zeroth order state as a function of kick number. Error bars are an average over three experiments. (b) Optical density plots for the initial state (red,solid) and kick numbers 2 (magenta,dot-dashed),4 (black,dotted), and 6 (blue,dashed) after summation of the time-of-flight image along the axis perpendicular to the standing wave. . . . .	60
4.6	Dependence of the acceleration resonance peak width as a function of the kick number in units scaled to the 4 <sup>th</sup> kick. Error bars are over three sets of experiments. . . . .	62
5.1	Schematic of a photoassociation process. Two atoms colliding along the ground state potential (S+S) absorb a photon and get excited to the (S+P) molecular potential. The excited molecule can subsequently decay to free atoms or a ground state molecule. . . . .	66

5.2	Centrifugal energy term $\hbar^2 l(l+1)/2\mu r^2$ of the Hamiltonian for three partial waves, $l=0,1,2$ . For low energy scattering all partial waves $l > 0$ are blocked by the centrifugal barrier. . . . .	70
5.3	Variation of the scattering length $a$ as a function of $\lambda = \sqrt{mV_0/\hbar^2}$ . As the well depth $V_0$ increases ((a) to (c)) a bound state is formed (dashed line) and the scattering length passes through a divergence and changes sign. . . . .	72
5.4	A Feshbach resonance occurs when an excited state has a bound state close to the collisional threshold. Changing the detuning $\Delta$ by an external field can couple the collisional to the bound state and change the scattering length. . . . .	74
5.5	Schematic of the optical set-up for the photoassociation light. . . . .	77
5.6	Flowchart of the locking for the photoassociation master laser. . . . .	78
5.7	Experimental configuration for photoassociation. Shown are the CO <sub>2</sub> laser FORT and the photoassociation beams. The Bragg (kicking) beams were aligned such that a horizontal standing wave was created along the long axis of the FORT. . . . .	84
5.8	Photoassociation spectrum of the $1_g(P_{3/2}), v = 152$ state. 0 MHz on this scale corresponds to a point 713 GHz below the $^{87}\text{Rb}$ D <sub>2</sub> line. The states $a$ through $e$ correspond to $ 2, -2, 3, -3\rangle,  3, -2, 3, -3\rangle,  1, -1, 3, -2\rangle,  2, -1, 3, -2\rangle,  1, 0, 1, -1\rangle$ of Ref. [118] labeled by the $ F, f, I, i\rangle$ quantum numbers. . . . .	85
5.9	Photoassociation of the $0_g^-(\sim S_{1/2} + P_{3/2}), v = 1$ state showing the J=0 and J=2 rotational levels. Each point is separated by 5 MHz. . . . .	86



5.10	(a) First order Bragg diffraction as a function of the frequency difference between the beams used to create the standing wave. (b) Percentage of Bragg diffracted atoms for two photoassociation light detunings, $\Delta/2\pi = +10\text{MHz}$ (red) and $-10\text{MHz}$ (blue). . . . .	87
5.11	Measured inelastic collision rate coefficients for the $0_g^-(P_{3/2}), v = 1, J = 2$ state. Also shown is a lorentzian fit to the data from which values of $\Gamma_{\text{spont}}$ and $\Gamma_{\text{stim}}$ are obtained. . . . .	88
5.12	Plot of the scattering length $a$ in units of $a_0 = 0.53\text{\AA}$ , the Bohr radius, calculated from the data in Fig. 5.11. The dashed line is the background scattering length of $100a_0$ and the detuning is with respect to the $0_g^-(P_{3/2}), v = 1, J = 2$ state. . . . .	89
5.13	Interference between condensates as a measure of mean field energy. Please refer to text for details. . . . .	90

## CHAPTER 1

### INTRODUCTION

Since its birth, quantum mechanics has stood the test of experiment. It has made remarkable progresses from theory to practice in the form of devices like atom interferometers, scanning tunneling microscopes and atomic clocks, to name a few.

Despite the success of quantum theory, subtle issues still remain in our understanding. According to Bohr's *Correspondence Principle* quantum mechanics reduces to Newtonian dynamics when the classical unit of action  $S$  becomes larger than the Planck's constant  $\hbar$ . However, the exact nature and causes for this transition is an open subject for discussion. This is perhaps best seen in the problem of quantizing chaos, noticed by none other than Einstein [1].

The existence of classical chaos was first shown by the French mathematician-physicist Henri Poincaré. Attempting to find an analytical solution to the dynamics of three gravitationally interacting bodies, he discovered the possibility of irregular motion, where slight changes in initial conditions could lead to vastly different trajectories. This was chaos in a deterministic system, without any random parameters. The problem was revisited in the mid-twentieth century. The result was the Kolmogorov-Arnold-Moser (KAM) theorem [2]. It quantified the amount of perturbation necessary for an integrable system to develop chaotic motion.

Carrying this concept of chaos over to the quantum realm runs into difficulties however. The overlap integral of two initially close wave packets undergoes unitary evolution to remain preserved over time. A better way of finding the quantum mechanical equivalent of chaos might be to look at the overlap of two similar states

evolving under slightly different Hamiltonians, as suggested by Peres [3]. These strategies for governing the evolution in phase space necessitate a deeper understanding of quantum transport in a classically chaotic system.

One of the widely researched systems of quantum transport in momentum or energy space is the multi-photon ionization of Rydberg atoms under periodic microwave driving [4, 5]. This was the first demonstration of the  $\delta$ -kicked rotor, a paradigm for studying classical and quantum chaos. Raizen's group at Austin demonstrated a much more experimentally manageable version with atom optics. Here, cold atoms were subjected to periodic flashes from an optical standing wave [6, 7]. In general, one-dimensional autonomous Hamiltonian systems are integrable as a result of the conservation of energy. There is therefore no chaos and the dynamics is regular. However, the energy periodically pumped into the kicked rotor breaks the time-invariance of the Hamiltonian and makes chaotic dynamics possible in this one dimensional classical system. Surprisingly, the quantum kicked rotor, despite the inherent non-integrability, was found to suppress classical chaotic motion. This was termed dynamical localization [6, 8–11], since it was reminiscent of Anderson localization in disordered solids. Decoherence introduced into the system for instance via spontaneous emissions or noise added to the kicking strength was found to destroy dynamical and restore classical diffusion [12–15]. Dynamical localization to this day remains an invaluable resource in investigating quantum-classical correspondence.

Such atom optical systems have also proved their versatility in modeling other physical phenomena in the spirit of Feynman's quantum simulator [16]. Cold atoms in accelerating optical lattices were found to exhibit Bloch oscillations, Wannier-Stark ladders and tunneling, transport behavior normally associated with solid state physics [17–22]. Variants of the kicked rotor have enabled the demonstrations of a quantum accelerator and quantum ratchet [23–27]. The sensitivity of momentum transport to the underlying classical chaos in this system also offers possibilities for

precision measurements. A group in France observed sub-Fourier resonances in a kicked rotor subject to two kicking frequencies [28]. Another study looked at the prospect of exploiting quantum rotor resonances to improve atom interferometric measurements of physical constants like the photon recoil frequency [29, 30].

The creation of a Bose-Einstein condensate by Cornell and Wieman in 1995 heralded a new era of experiments [31, 32]. Unprecedented control over quantum state preparation and manipulation was now possible. A BEC has a momentum width less than that of a photon recoil. In the context of the quantum kicked rotor and accelerator, it allowed a close look at their phase spaces. The first BEC was achieved by evaporative cooling of already cold atoms in a magnetic trap. Condensates in our lab are produced in an optical trap, which has proved to be a simple yet robust method [33].

## 1.1 Organization

Two important aspects of the atom optics kicked rotor are investigated in this thesis - transport and resonance width scaling. Experiments were also conducted to observe an Optical Feshbach resonance in a  $^{87}\text{Rb}$  Bose-Einstein Condensate, which could be useful for further kicked rotor research. To provide a theoretical and experimental backdrop for these studies, we begin with Chapter 2 which introduces the quantum delta-kicked rotor and discusses properties exhibited by it and its variants. The laboratory realization of the quantum rotor is in the form of a Bose-Einstein Condensate subjected to a periodically pulsed standing wave of light detuned far from any atomic resonances. An account of the theoretical background, from laser cooling techniques to evaporative cooling, necessary in achieving a phase space transition to a BEC is given. This is followed by a description of the experimental techniques which we employ in order to create such a condensate and perform experiments on it.

Chapter 3 reviews two kinds of quantum transport behavior made possible by this

system. The first one details the observation and properties of quantum accelerator modes, specifically higher order resonances of such a mode. Two models, an interference model based on the re-phasing of wavefronts, and a classical-like model can explain the occurrences of such modes and are discussed. The momentum evolution predicted by the two theories is then compared with experiment. Next we see how preparation of a special initial state of the rotor can establish a momentum current even in the absence of a net bias force. The directed current appears in the absence of dissipation and is an example of a quantum ratchet. Its realization will be described next. The effect of the finite momentum width of a condensate on the ratchet current is also investigated.

The relatively nascent topic of applying the quantum kicked rotor towards precision measurements is the subject of Chapter 4. This system exhibits resonances in the mean energy at specific combinations of the kicking period and initial momentum. It is shown that the fidelity or quantum mechanical overlap of an off-resonant state with one that is on resonance scales at a sub-Fourier rate, with respect to the measurement time. The existence of resonances at particular values of the acceleration of the standing wave is also analyzed and verified by experiment. These resonances are also shown to have sub-Fourier widths.

Interactions among atoms in a Bose-Einstein condensate can be strongly tuned near a Feshbach resonance. Presence of such interactions can introduce nonlinearity into the kicked rotor, thereby enabling a probe at quantum chaos. Chapter 5 details photoassociation spectroscopy performed on a Bose-Einstein condensate for the  $1_g$  and  $0_g^-$  long range molecular states. Bragg spectroscopy was employed to detect optically induced changes in the elastic scattering length near one of these molecular states, the sign of an Optical Feshbach resonance.

Finally, the conclusions are laid out in chapter 6 including the outlook for future research.

## CHAPTER 2

### Delta-Kicked Rotor : Theory and Experiments

For more than three decades the delta kicked rotor has been at the centerstage in the study of quantum chaos. The relative ease with which it can be handled analytically has drawn many researchers to it. It is the basic model for studying dynamical chaos [34] and is described classically by the Standard Map. In this chapter we review this model and its quantum analogue. Along the way we examine some of the rich features this simple system has revealed so far. Finally, we look at the implementation of this model in our lab in an atom optics setting.

#### 2.1 Classical kicked rotor

The kicked rotor is a pendulum exposed to a periodic constant force like gravity. Its Hamiltonian is

$$H = \frac{p^2}{2I} + V_0 \cos(\theta) \sum_N \delta(t - NT) \quad (2.1)$$

$p$  is the angular momentum,  $\theta$  the angular displacement,  $I$  the moment of inertia and  $V_0$  the kick strength.  $t$  is the time and  $N$  counts the kicks which are switched on at time intervals of  $T$ . Choosing  $I = 1$ , we can write Hamilton's equation's of motion as

$$\begin{aligned} \frac{\partial H}{\partial \theta} &= -\dot{p} = -V_0 \sin(\theta) \delta(t - NT) \\ \frac{\partial H}{\partial p} &= \dot{\theta} = p \end{aligned} \quad (2.2)$$

Integrating Eqs. (2.2) over one period between  $t = N$  and  $t = N + 1$ ,

$$\begin{aligned} p_{N+1} &= p_N + V_0 \sin(\theta_N) \\ \theta_{N+1} &= \theta_N + p_{N+1} T \end{aligned} \quad (2.3)$$

Using the rescaled variables  $\rho = pT$  and  $K = V_0T$ , (2.3) can be written as

$$\begin{aligned}\rho_{N+1} &= \rho_N + K \sin(\theta_N) \\ \theta_{N+1} &= \theta_N + \rho_{N+1}\end{aligned}\tag{2.4}$$

This is known as the *Standard* or *Taylor-Chirikov Map* where the dynamics is completely determined by the ‘stochasticity parameter’  $K$  [35]. As seen in the  $\rho - \theta$  phase space (modulo  $2\pi$ ) of Fig. 2.1, the islands of stability at small  $K$  give way to chaotic regions with increasing  $K$ . Numerical analysis showed that the transition to global stochasticity occurs at a value of  $K \approx 0.9716$  [36].

At the end of ‘ $t$ ’ kicks,

$$\langle (\rho_t - \rho_0)^2 \rangle = K^2 \sum_{q,r}^{t-1} (\sin \theta_q \sin \theta_r)\tag{2.5}$$

Ignoring the correlation terms for large  $K$ , we get

$$\langle \rho_t^2 \rangle \cong \frac{1}{2} K^2 t\tag{2.6}$$

Thus the chaotic domain of the classical  $\delta$ -kicked rotor is characterized by a diffusive growth of the mean energy.

## 2.2 Atom optics $\delta$ -kicked rotor

Study of the quantum version of the  $\delta$ -kicked rotor was made possible by remarkable advances in atom optics. Its experimental realization can be described in terms of the center of mass Hamiltonian of an atom of mass  $M$  exposed to short periodic pulses of far detuned light [6, 7, 37],

$$\hat{H} = \frac{\hat{P}^2}{2M} + \hbar \phi_d \cos(G \hat{X}) \sum_{N=-\infty}^{\infty} \delta(t' - NT)\tag{2.7}$$

$G = 4\pi/\lambda$  is the grating vector of the standing wave formed from a laser of wavelength  $\lambda$ . It is convenient to convert this Hamiltonian to dimensionless units. This can be

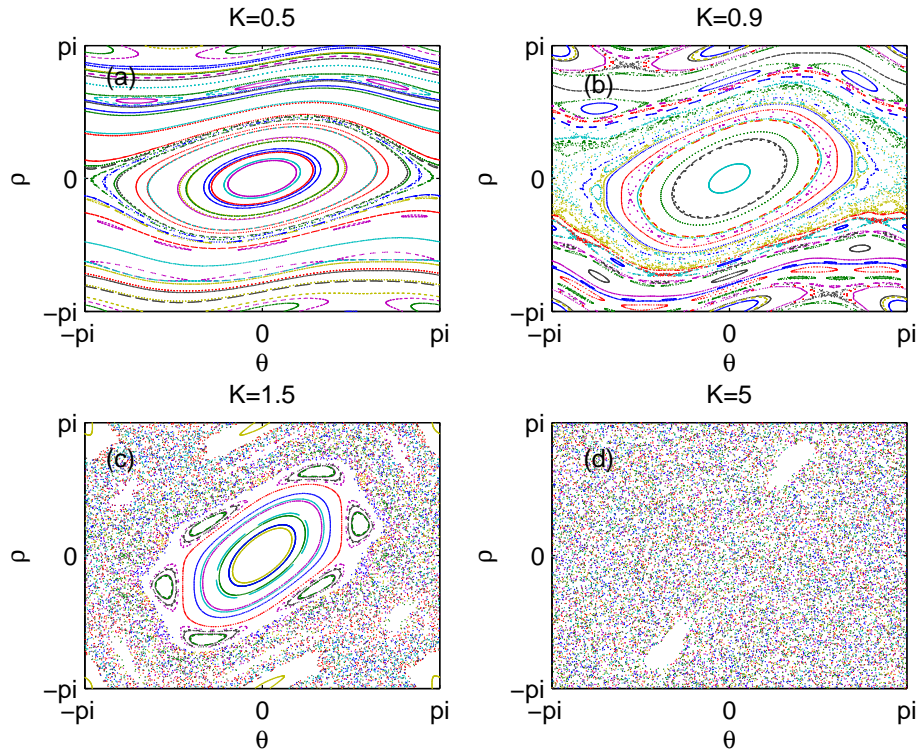


Figure 2.1: Classical  $\delta$ -kicked rotor phase space for different kick strengths  $K$ . Onset of stochastic regions can be seen in (c) while (d) is predominantly chaotic.



done by expressing position in units of  $G^{-1}$ ,  $\hat{x} = G\hat{X}$  and momentum in units of  $\hbar G$ ,  $\hat{p} = \hat{P}/\hbar G$ .

$$\hat{\mathcal{H}} = \frac{\hat{p}^2}{2} + \phi_d \cos(\hat{x}) \sum_N \delta(t - N\tau) \quad (2.8)$$

The scaled period is  $\tau = 2\pi T/T_{1/2}$ , time is measured in  $t = 2\pi t'/T_{1/2}$  and  $\hat{\mathcal{H}} = (M/(\hbar G)^2)\hat{H}$ .  $T_{1/2} = 2\pi M/\hbar G^2$  is known as the half-Talbot time, the physical significance of which we shall soon see. The periodicity of the potential provides the connection between the particle propagating along it and the kicked rotor. The position of the particle can be folded into an angular coordinate  $\theta = x \bmod(2\pi)$ . From a quantum mechanical perspective, the periodicity of the potential allows us to use Bloch's theorem on the atomic de-Broglie wave. The solutions are then invariant under translations by one period of the potential [38]. A result of this invariance is the conservation of the particle *quasimomentum*. In terms of photon exchange, each atom absorbs a photon from one of the standing wave beams followed by its subsequent stimulated emission into the other beam. The net result is that the atom momentum changes by two photon recoils ( $2\hbar k$  or  $\hbar G$ ) while leaving the fractional part of its momentum (or the *quasimomentum*, in units of  $\hbar G$ ) unchanged.

The light shift of the atomic ground state in the presence of this optical potential is

$$\Delta E_g = \frac{\hbar \Omega^2}{4\delta} \cos^2(x/2) \quad (2.9)$$

where  $\Omega \equiv \frac{-eE_0}{\hbar} \langle e|r|g \rangle$  is the Rabi frequency between the excited and ground states.  $E_0$  is the amplitude of the potential and it is detuned  $\delta$  from the atomic transition. This sinusoidal energy shift leads to the standing wave acting as a phase grating on the atomic wave function. The strength of the kicks is therefore given by the phase modulation depth parameter,  $\phi_d = \Omega^2 \Delta t / 8\delta$ . Change in the kinetic energy of the atoms is negligible during the short time the potential is on (Raman-Nath regime). In this limit, the imprint of the thin phase-grating on an incident plane wave  $|0\rangle$

results in a final state

$$\begin{aligned}
|\psi(\Delta t)\rangle &= e^{-i\phi_d \cos(\hat{x})}|0\rangle \\
&= \sum_{n=-\infty}^{\infty} (-i)^n J_n(\phi_d) e^{-in\hat{x}}|0\rangle \\
&= \sum_{n=-\infty}^{\infty} (-i)^n J_n(\phi_d)|n\rangle
\end{aligned} \tag{2.10}$$

where the second line derives from the Jacobi-Anger expansion,  $J_n$  is the  $n^{\text{th}}$  order Bessel function of the first kind, and  $|n\rangle$  is a momentum order along the grating in units of  $\hbar G$ . After a free evolution for a period  $T$ , the wave function is

$$|\psi(t)\rangle = \sum_n (-i)^n J_n(\phi_d) e^{-i\frac{\hat{p}^2}{2}\tau} |n\rangle \tag{2.11}$$

### 2.2.1 Quantum resonances and anti-resonances

We can now write the one period evolution operator as

$$\hat{U} = e^{-i\phi_d \cos(\hat{x})} e^{-i\frac{\hat{p}^2}{2}\tau}. \tag{2.12}$$

When the time period  $\tau$  is an integer multiple of  $4\pi$ , the free evolution factor is unity.  $N$  consecutive kicks of strength  $\phi_d$  are then equivalent to one kick of strength  $N\phi_d$ . That is,

$$\hat{U}^N = e^{-iN\phi_d \cos(\hat{x})}. \tag{2.13}$$

From the initial state  $|0\rangle$ , we then have a momentum distribution

$$\begin{aligned}
p_n &= |\langle n|U^N|0\rangle|^2 \\
&= J_n^2(N\phi_d)
\end{aligned} \tag{2.14}$$

The mean energy at the end of  $N$  kicks is then

$$\begin{aligned}
\langle E \rangle &= \sum_{n=-\infty}^{\infty} n^2 p_n \\
&= \sum_n n^2 J_n^2(N\phi_d) \\
&= \frac{1}{2} N^2 \phi_d^2
\end{aligned} \tag{2.15}$$

This uniquely quantum effect, characterized by the quadratic growth of energy, is termed a *quantum rotor resonance*. It is the temporal equivalent of the Talbot effect in optics and the resonant time period is therefore called the Talbot time,  $T_T = 4\pi M/\hbar G^2$  [6, 39].

Next we look at a zero initial momentum state, exposed to a kick, and allowed to evolve for half of the Talbot time ( $T_{1/2}$ ). Now,  $\tau = 2\pi$  (or any odd integer multiple of it), and the phases acquired by the momentum orders are +1 or -1 depending on whether the order is even or odd. The state at the end of the half-Talbot time is,

$$\begin{aligned} |\psi(t = T_{1/2})\rangle &= \sum_{n=-\infty}^{\infty} (-i)^n J_n(\phi_d) e^{-i\pi n^2} e^{-in\hat{x}} |\psi_0\rangle \\ &= e^{i\phi_d \cos(\hat{x})} |\psi_0\rangle \end{aligned} \quad (2.16)$$

where we have used the property,  $e^{-i\pi n^2} = e^{-i\pi n}$ . A kick applied at this point will cancel out the spatial variation due to the first kick recreating the original state. This phenomenon is known as a *quantum anti-resonance*.

A numerical simulation of these two effects can be performed using a technique shown in Ref. [39]. Beginning with a zero momentum initial state (convoluted by a finite width Gaussian to account for the BEC momentum spread), the quantum delta-kicked rotor is realized by repeated application of the one period evolution operator of (2.12). Figure 2.2 shows a simulated quantum *resonance* and *anti-resonance*.

### 2.2.2 Dynamical Localization

We now turn our attention to the generic behavior of the quantum delta kicked rotor, away from these resonances, that is when  $\tau/2\pi$  is an irrational number. In Section 2.1 we saw how strong chaos dictates a diffusive energy growth of the classical kicked rotor. In order to investigate the behavior of its quantum counterpart, Casati, Chirikov, Ford and Izrailev [40, 41] in 1979 simulated the quantum kicked rotor. Contrary to expectations, however, they were surprised when the quantum rotor showed corre-

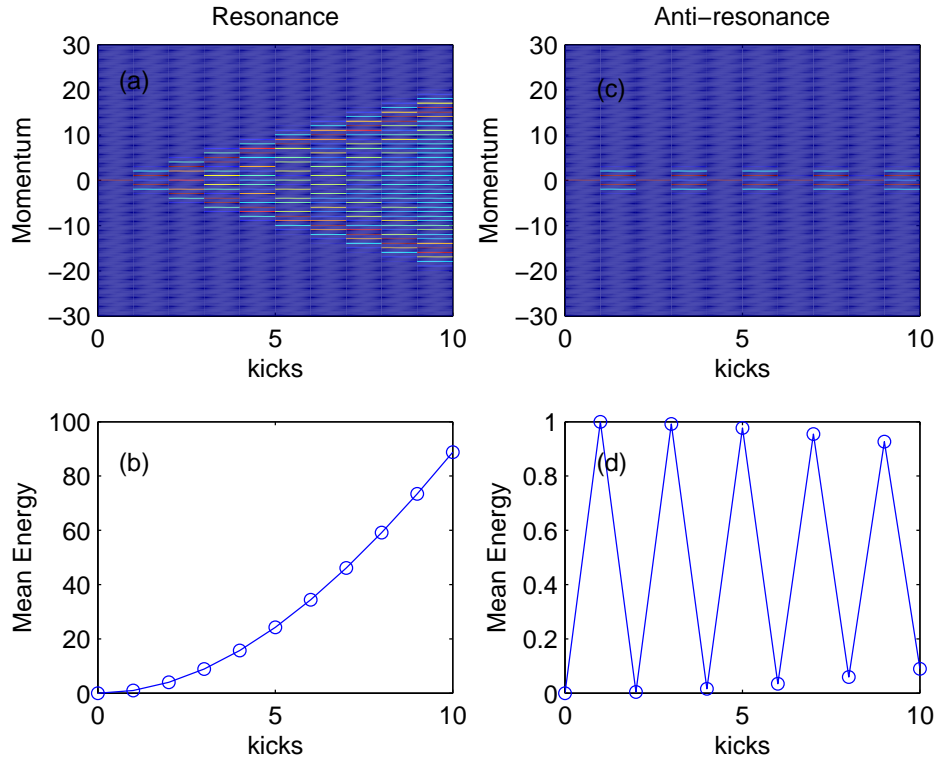


Figure 2.2: (a) and (b), A quadratic growth in the mean energy at a quantum resonance at the Talbot time, and (c) and (d), an oscillatory mean energy at an anti-resonance at  $T = T_{1/2}$ .

spondence with the classical case only upto a certain time even in the deeply chaotic domain ( $\phi_d \gg 1$ ). After this, quantum interference was found to suppress any further growth of momentum [42]. This phenomenon came to be known as *dynamical localization*, and was shown to be analogous to Anderson localization in disordered solids [34, 43]. In the rotor, destructive interference between momentum orders separated by irrational multiples of  $2\pi$  leads to a final eigenstate exponentially localized in momentum.

### 2.2.3 Quantum Transport

While the mean energy of the QDKR increases ballistically with kicks at a quantum resonance, the mean momentum  $\langle p \rangle$  remains fixed. Presence of a linear potential like gravity breaks the symmetry of the system. The momentum acquired by the  $q^{\text{th}}$  order at the end of  $N$  kicks is  $mv_i + q\hbar G + mgNT$ . The phase acquired by the momentum state  $|q\rangle$  therefore has a gravity dependent term,  $\phi_q = v_i GTq + \frac{\hbar G^2}{2m} Tq^2 + gGT^2 Nq$ . When the phase difference between  $|q\rangle$  and  $|q-1\rangle$ ,

$$\phi_q - \phi_{q-1} = \frac{\hbar G^2}{2m} T(2q-1) + v_i GT + gGT^2 N \quad (2.17)$$

is a multiple of  $2\pi$ , order  $|q-1\rangle$  can be perfectly coupled to  $|q\rangle$  by the next kick. This imposes two conditions on rephasing, one which depends on the kick number and another which does not.

$$\frac{\hbar G^2}{2m} T2q + gGT^2 N = 2\pi ql' \quad (2.18)$$

$$v_i GT - \frac{\hbar G^2}{2m} T = 2\pi l \quad (2.19)$$

Equation (2.18) can be solved to find the momentum at the end of  $N$  kicks,

$$q = \frac{N}{\gamma} \frac{\alpha^2}{l' - \alpha} \quad (2.20)$$

where  $\alpha = T/T_{1/2}$  and  $\gamma = \hbar^2 G^3 / 2\pi m^2 g$ . Therefore, near a resonance, a fixed momentum can be imparted to a section of the atoms by each kick. This is a *quantum accelerator mode* created with the quantum delta kicked accelerator (QDKA).

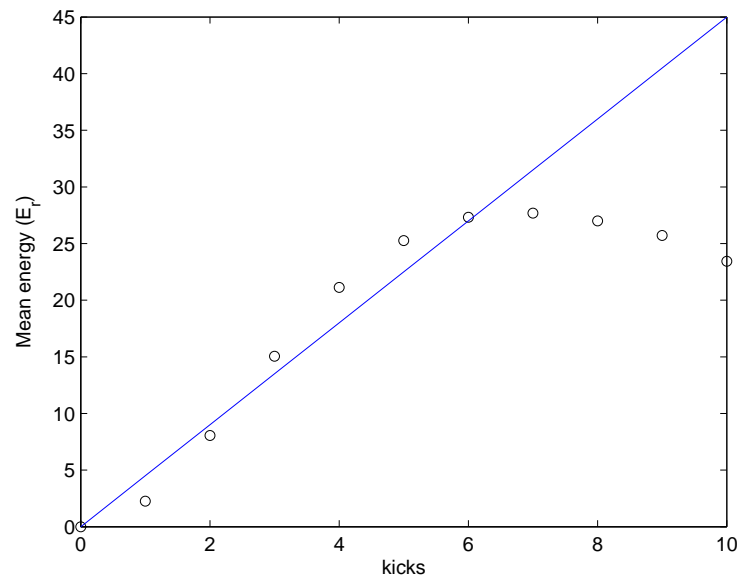


Figure 2.3: Quantum suppression of classical chaos. Simulation of the QDKR near the Talbot time with  $\phi_d=3.0$  shows the onset of dynamical localization after six kicks. Also shown is the classical momentum diffusion (solid line).

Among many possibilities, its use as a coherent beam splitter for an interferometer has brought it a great deal of attention among researchers since its discovery almost a decade ago in Oxford [44].

Another topic of recent focus in rectified transport is a *ratchet*, where a directed current of particles along a periodic potential can be established even in the absence of a biased force. A pure quantum ratchet was first demonstrated at a QDKR resonance by Sadgrove et al. [45]. It was realized with an initial state prepared in a superposition of a zeroth and first order momentum states (in units of  $\hbar G$ ),

$$|\psi\rangle_i = \frac{1}{\sqrt{2}}[|0\rangle + |1\rangle]. \quad (2.21)$$

After a time ‘ $t$ ’ of free evolution, the first order accumulates a phase  $\theta$ ,

$$|\psi(t)\rangle = \frac{1}{\sqrt{2}}[|0\rangle + e^{i\theta}|1\rangle]. \quad (2.22)$$

The state after application of a kick become,

$$\begin{aligned} |\psi(t^+)\rangle &= e^{-i\phi_d \cos(\hat{x})} |\psi\rangle_i \\ &= \frac{1}{\sqrt{2}} \sum_q (-i)^q [J_q(\phi_d) + e^{i\theta} J_{q-1}(\phi_d)] |q\rangle \end{aligned} \quad (2.23)$$

with a distribution,

$$p_q = \frac{1}{2} [J_q(\phi_d)^2 + J_{q-1}(\phi_d)^2 + 2 \cos \theta J_q(\phi_d) J_{q-1}(\phi_d)] \quad (2.24)$$

Recalling the Bessel function property,  $J_{-n}(x) = (-1)^n J_n(x)$ , we notice that the momentum distribution is asymmetric whether  $q$  is odd or even. This is a ratchet current, the strength of which can be tuned by the relative phase  $\theta$ .

Experiments on these and other exotic properties of the  $\delta$ -kicked rotor depend on an initial momentum state with a spread that is less than one photon recoil. The ideal atomic physics system for this is a Bose-Einstein condensate. The next sections outline the stages in reaching this quantum state of matter and its realization in our lab.

## 2.3 Bose-Einstein Condensation

In 1924, Satyendranath Bose proposed a statistical technique to evaluate the photon black body spectrum [46]. Einstein extended the theory to the general case of identical particles leading to the birth of Bose-Einstein statistics [47]. The distribution function for particles obeying this statistics is

$$N(E) = \frac{1}{e^{\beta(E-\mu)} - 1} \quad (2.25)$$

where  $\beta = 1/k_B T$  and  $\mu$  is the chemical potential. Einstein noticed a peculiarity, that below a certain critical temperature, these bosonic atoms would accumulate in the lowest energy quantum state: the onset of the Bose-Einstein Condensate (BEC) phase. In terms of the phase space density,  $\rho = n\lambda_{dB}^3$ , where  $n$  is the particle number density, a BEC phase transition happens when  $\rho = \zeta(\frac{3}{2}) = 2.612$ . In other words once a particle's thermal de-Broglie wavelength  $\lambda_{dB} = \left(\frac{2\pi\hbar^2}{mk_B T}\right)^{1/2}$  becomes greater than the interparticle separation,  $\lambda_{dB} > n^{-\frac{1}{3}}$ , this macroscopic quantum state starts appearing.

A subject of academic curiosity for more than half a century, achievement of a BEC was given serious thought when laser cooling of atoms was realized. This cooling scheme is based on using optical forces to reduce the thermal velocity distribution of atoms. An indepth discussion of BEC in the Summy lab at OSU can be found in the theses of Ahmadi, Timmons, and Behin Aein [48–50]. I shall therefore only outline the general principles involved.

### 2.3.1 Laser Cooling and Trapping

The light force on an atom in general comprises of two parts,  $F = F_{dip} + F_{sc}$ , a conservative dipole force,  $F_{dip}$  and a dissipative scattering force  $F_{sc}$ . The science of laser cooling was built primarily on the second kind, which is a result of absorption



of photons by atoms followed by spontaneous emission. This force is expressed as

$$F_{sc} = \hbar k \gamma \rho_{ee} \quad (2.26)$$

where  $\hbar k$  is the momentum transferred by a photon,  $\gamma$  is the rate of decay of the excited state of the atom and  $\rho_{ee}$  is the probability for the atoms to be in the excited state. Evaluating  $\rho_{ee}$  using the optical Bloch equations, one can show that,

$$F_{sc} = \hbar k \frac{s_0 \gamma / 2}{1 + s_0 + (2\delta / \gamma)^2}. \quad (2.27)$$

Here,  $s_0 = 2|\Omega|^2 / \gamma^2$  is the on-resonance saturation parameter and  $\delta = \omega_l - \omega_a$  is the detuning of the light from the atomic transition. We now consider the case of an atom with velocity  $\vec{v}$  placed in the light field of two beams counter-propagating along the z-axis. In addition we arrange a linearly inhomogeneous magnetic field  $B = Az$  formed by a magnetic quadrupole field. In the limit of low light intensity, the total force on the atom due to the two beams is,  $\vec{F} = \vec{F}_+ + \vec{F}_-$ , where

$$\vec{F}_{\pm} = \hbar \vec{k} \frac{s_0 \gamma / 2}{1 + s_0 + (2\delta_{\pm} / \gamma)^2}. \quad (2.28)$$

The detuning is  $\delta_{\pm} = \delta \mp \omega_D \pm \omega_Z$ , where we now have to include the Doppler shift  $\omega_D = \vec{k} \cdot \vec{v}$  and the Zeeman shift  $\omega_Z = \mu' B / \hbar$ ,  $\mu'$  being an effective magnetic moment [51]. In the limit of Doppler and Zeeman shifts that are small compared to  $\delta$ , we arrive at the total force,

$$\vec{F} = -\beta \vec{v} - \frac{\mu' A}{\hbar k} \beta \vec{r} \quad (2.29)$$

which is the motion of a damped harmonic oscillator with the damping constant  $\beta = -\frac{8\hbar k^2 \delta s_0}{\gamma \{1 + s_0 + (2\delta / \gamma)^2\}^2}$ . Thus with a configuration of three retroreflecting beams tuned below the atomic resonance, the Zeeman shift provides a confining potential for the atoms creating what is known as the Magneto-Optic Trap (MOT). The presence of a viscous damping force due to the Doppler effect leads to a significant reduction in the velocity distribution of the atoms forming an ‘‘Optical Molasses’’ [52, 53].

### 2.3.2 Limits of laser cooling

There is a limit to the temperatures that can be obtained in an optical molasses due to recoil heating. This effect results from a diffusion of the atoms in momentum space set off by the random nature of the photon scattering events. A steady state is reached when molasses cooling equals recoil heating which determines the limiting Doppler temperature,  $T_D$ ,

$$T_D = \frac{\hbar\gamma}{2k_B}. \quad (2.30)$$

For  $^{87}\text{Rb}$  the Doppler temperature is  $146 \mu\text{K}$ . Surprisingly, in one of the early experiments with Na atoms, temperatures 10 times lower than the Doppler temperature were observed [54]. Later, a theory which included the multilevel structure of the atomic states and the optical pumping among these sublevels was able to explain these sub-Doppler temperatures [55, 56]. This process became known as polarization gradient cooling. The next limit to the laser cooling temperature is set by the energy associated with a photon recoil,  $E_r = \hbar^2 k^2 / 2m$ . The recoil limit temperature,

$$T_r = \frac{\hbar^2 k^2}{mk_B} \quad (2.31)$$

has a value of 360 nK for  $^{87}\text{Rb}$ .

### 2.3.3 Evaporative cooling

The maximum phase space density possible with laser cooling is  $10^{-5} - 10^{-4}$ . Cold atom physicists soon realized that in order to increase it any further, evaporative cooling would be the way to go. Originally proposed by Hess [57] for atomic hydrogen, the method is based on the preferential removal of high energy atoms from a confined sample, followed by rethermalization of the remaining atoms by elastic collisions. The simultaneous decrease in the temperature and the volume leads to an increase in the phase space density.

Several models have been developed to explain the process of evaporative cooling. These include analytical and numerical treatments by Doyle and coworkers [58], Luiten *et al.*, and Wu and Foot [60] among a few. We shall here focus on a simple yet highly instructive analytical model due to Davis *et al.* [59]. In this model the trap depth is lowered in one single step to a finite value  $\eta k_B T$  and the effect of removal of high energy atoms on the thermodynamical quantities is calculated. The remaining fraction of atoms is  $\nu = N'/N$ . The decrease in temperature caused by the release of the hot atoms can be defined by the quantity,

$$\gamma = \frac{\log(T'/T)}{\log \nu}. \quad (2.32)$$

In a d-dimensional potential,  $U(r) \propto r^{d/\xi}$  and the volume  $V \propto T^\xi$  [61]. The value of  $\xi$  describes the type of the potential. For a linear potential like a spherical quadrupole trap,  $\xi = 3$  and for a harmonic potential as in an optical trap,  $\xi = 3/2$ . We thus have the scaling of the important thermodynamic quantities,  $N' = N\nu$ ,  $T' = T\nu^\gamma$ , and  $V' = V\nu^{\gamma\xi}$ . The phase space density  $\rho = n\lambda_{dB}^3$  scales as  $\rho' = \rho\nu^{1-\gamma(\xi+3/2)}$ . With the knowledge of  $\xi$ ,  $\nu(\eta)$ , and  $\gamma(\eta)$  one can track the evolution of these quantities with the lowering of the trap depth.

The density of states for atoms in a trapping potential  $U(x, y, z)$  is

$$D(E) = \frac{2\pi(2M)^{3/2}}{\hbar^3} \int_V \sqrt{E - U(x, y, z)} d^3\mathbf{r} \quad (2.33)$$

The fraction of atoms which remain in the trap after its depth has been decreased to  $\eta k_B T$  is

$$\nu(\eta) = \frac{1}{N} \int_0^{\eta k_B T} D(E) e^{-(E-\mu)/k_B T} dE. \quad (2.34)$$

The occupation number is given by the Maxwell-Boltzmann distribution  $e^{-(E-\mu)/k_B T}$  since the effects of quantum statistics can be neglected for a dilute gas.  $\mu$  is the chemical potential of the gas. We can write Eq.(2.34) as,

$$\nu(\eta) = \int_0^\eta \Delta(\epsilon) e^{-\epsilon} d\epsilon \quad (2.35)$$

where  $\epsilon = E/k_B T$  is the reduced energy and the reduced density of states is

$$\Delta(\epsilon) = \frac{\epsilon^{1/2+\xi}}{\Gamma(3/2+\xi)} \quad (2.36)$$

After truncation, the total energy of the atoms is  $\alpha(\eta)Nk_B T$  where

$$\alpha(\eta) = \int_0^\eta \epsilon \Delta(\epsilon) e^{-\epsilon} d\epsilon. \quad (2.37)$$

Therefore the average total energy per atom(in units of  $k_B T$ ) is  $\alpha(\eta)/\nu(\eta)$ . Before truncation ( $\eta \rightarrow \infty$ ) this quantity is  $\alpha(\infty)/\nu(\infty) = (3/2 + \xi)/1$ . The decrease in temperature is thus

$$\frac{T'}{T} = \frac{\alpha(\eta)/\nu(\eta)}{\alpha(\infty)/\nu(\infty)}. \quad (2.38)$$

Using Eq.(2.32) we now have,

$$\gamma(\eta) = \frac{\log(\frac{\alpha(\eta)}{\nu(\eta)\alpha(\infty)})}{\log[\nu(\eta)]}. \quad (2.39)$$

Solving Eqs. (2.35), (2.36), and (2.37) for a specific form of potential, one can determine  $\gamma(\eta)$ . For  $\xi = 3/2$ ,  $\nu(\eta) = 1 - \frac{2+2\eta+\eta^2}{2e^\eta}$  and  $\alpha(\eta) = 3 - \frac{6+6\eta+3\eta^2+\eta^3}{2e^\eta}$ . Figure 2.4 shows the dependence of the number of atoms, temperature, density and phase space density on the normalized truncation parameter  $\tilde{\eta} = \frac{\eta}{3/2+\xi}$  for  $\xi = 3/2$  and  $\xi = 3$ . It can be seen that for the same truncation,  $\tilde{\eta}$ , a higher phase space density is achieved with a larger  $\xi$  due to a faster shrinking of volume with decreasing temperature ( $V \propto T^\xi$ ).

## 2.4 Experimental Configuration

Ever since the first Bose-Einstein condensate [31], rubidium 87 has been an atom of choice, due to its large elastic cross sections and the convenience of trapping it with inexpensive diode lasers. The light needed to trap and cool these atoms is tuned close to the Rb87  $F=2 \rightarrow F'=3$  transition shown in the D2 hyperfine structure in Fig. 2.5. In our experiment this light was derived from a grating stabilized Toptica

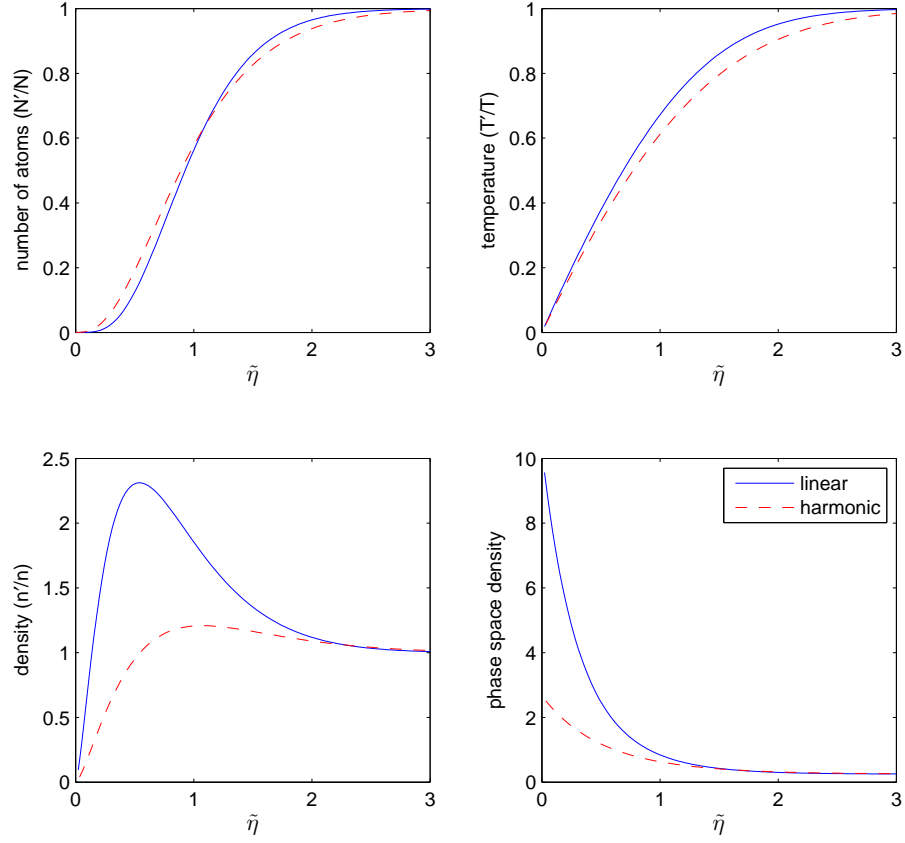


Figure 2.4: Evolution of thermodynamic quantities as a function of the trap truncation parameter.

DL-100 diode laser with a 1 MHz linewidth and 15 mW of output power. We call this our master laser. Using saturated absorption spectroscopy it was locked to the  $F=2 \rightarrow F'=2$  and  $F'=3$  crossover line. This light was injected into a home-made temperature stabilized slave laser with an output of 110 mW as shown in Fig. 2.6. Three frequency detunings of the light are needed in the experiment: -20 MHz for the MOT, -90 MHz for molasses cooling, and 0 MHz for imaging. To enable fast switching between these, the output from this main slave was sent through an Acousto-Optic Modulator (AOM) in a double-pass configuration. The frequency adjusted light was finally injected into a series of two slave lasers used for the actual trapping and cooling of atoms.

Due to non-resonant excitation to the  $F'=2$  state, some of the atoms can fall down to the  $F=1$  ground state and get out of the trapping cycle. To bring them back into the MOT, a repumping laser tuned to the  $F=1 \rightarrow F'=2$  state is used. Control over the intensity of this light is also crucial during the FORT loading stage and is adjusted by an AOM. All of these optics are placed in an isolated table as seen in Fig. 2.6. The trapping and repump beams are coupled through two fibers to the table containing the vacuum chamber. The vacuum chamber consisted of an octagonal multi-port chamber attached to a flange of a six-way cross. An ion pump attached to another flange kept the vacuum pressure at  $10^{-11}$  Torr.

After exiting the fiber on the second table, the MOT light is divided into three beams, circularly polarized and diameters expanded to 2.2 cm. These are then sent into the vacuum chamber from three orthogonal directions and then retroreflected with opposite circular polarization. The MOT is formed at the intersection of these six beams. The inhomogeneous magnetic field required to create the confining potential of the MOT was formed using two sets of water cooled coils arranged in an anti-Helmholtz configuration. A magnetic field gradient of 10 Gauss/cm along the axial direction was obtained with the coil geometry of our experiment. Around 10 million

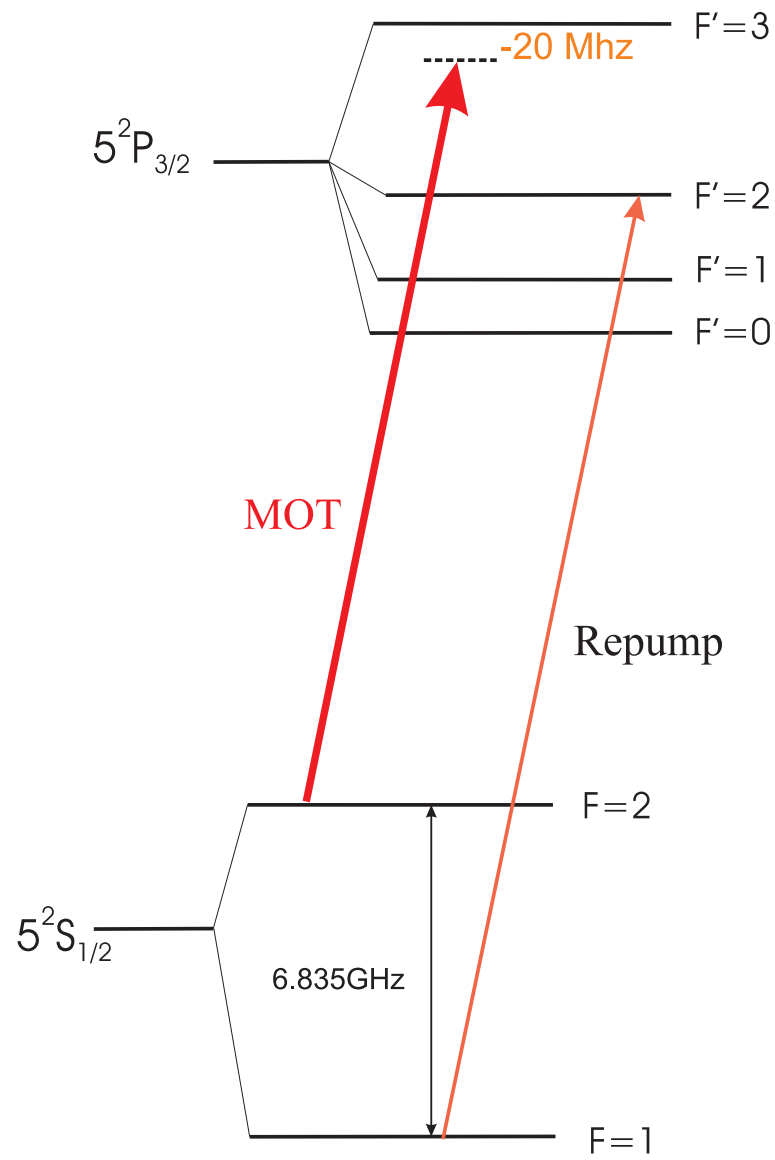


Figure 2.5: A schematic of the rubidium D2 transition.

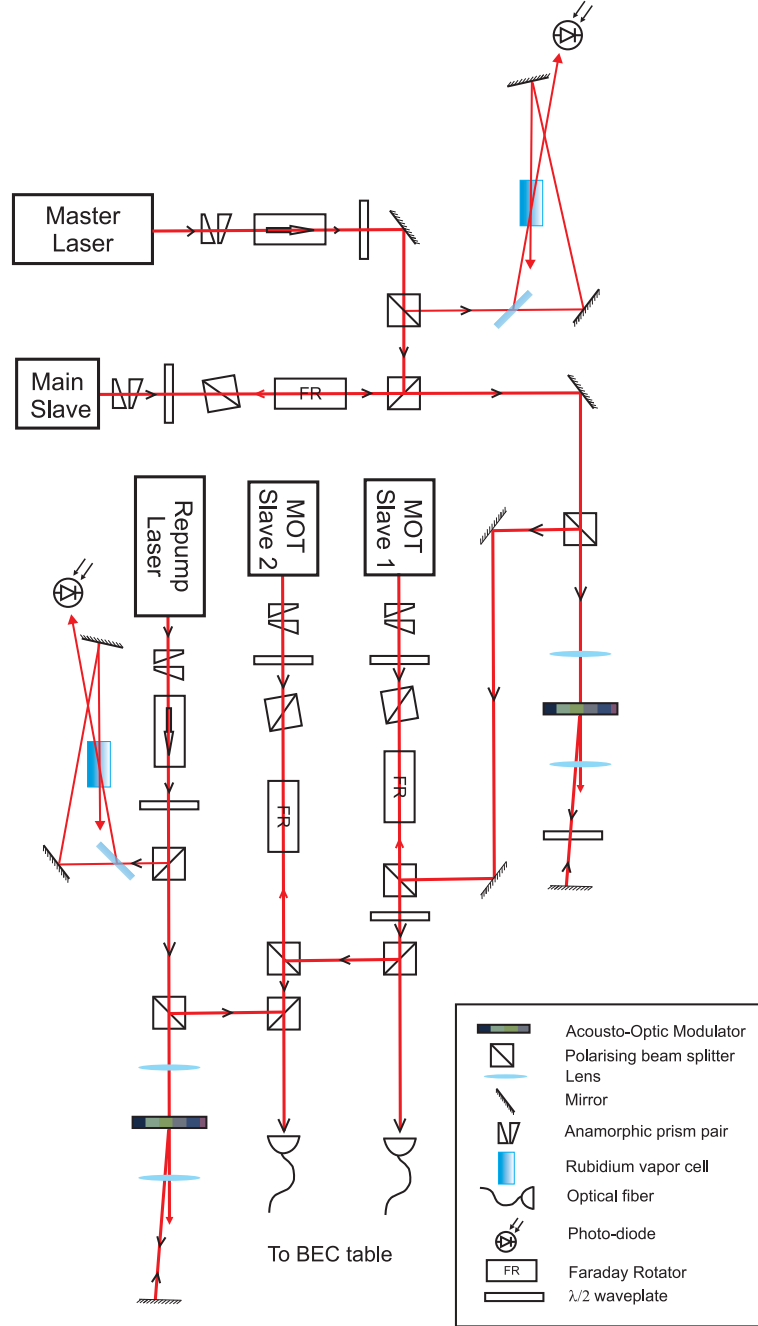


Figure 2.6: Set-up of the optical table for the BEC experiments. Not shown is a final 80 MHz AOM for both the MOT Slave beams before the optical fibers.



atoms were trapped in this Magneto-Optic trap. Finally, stray magnetic fields in the region of the MOT were removed with three pairs of Helmholtz coils, commonly known as the nulling coils.

A 50W CO<sub>2</sub> laser formed the Far Off-Resonant Trap (FORT) for the evaporative cooling stage. With a wavelength of 10.6 $\mu$ m, the laser is far detuned from the atomic resonance and its effect on the atoms can be considered as that of a static electric field. An atom with a ground state polarizability  $\alpha_g$  placed in the electric field  $E(x, y, z)$  of the Gaussian beam given by

$$|E|^2 = E_0^2 \frac{\exp[\frac{-2(x^2+y^2)}{w_0^2(1+(\frac{z}{z_R})^2)}]}{1 + (\frac{z}{z_R})^2}. \quad (2.40)$$

experiences a potential  $U = \frac{1}{2}\alpha_g E^2$ . Here  $w_0$  is the beam waist and  $z_R = \pi w_0^2/\lambda$  is the Rayleigh length. The focus of the beam where  $z \ll z_R$ , serves as a harmonic trapping potential

$$U = -\frac{1}{2}\alpha_g E_0^2 (1 - \frac{2x^2}{w_0^2} - \frac{2y^2}{w_0^2} - \frac{z^2}{z_R^2}). \quad (2.41)$$

The output of the CO<sub>2</sub> laser passed through a 40 MHz RF-driven AOM. The 35W first order from the AOM overlapped the MOT for a loading time of typically 20 seconds. The MOT light detuning was then increased to -90 MHz for optical molasses cooling. This was followed by reduction of the repump intensity to produce a temporal dark MOT. During this crucial step, atoms start entering into a state that is “dark” to the cooling light. The resultant decrease in the recoil heating and excited state collisions leads to an increase in the phase space density. After around 100ms, the MOT and repump beams were extinguished and the magnetic coil current switched off.

The FORT beam was transported into the vacuum chamber by a three lens assembly: the first two lenses formed a 2x beam expander followed by a third focussing lens mounted inside the chamber. The final spot size at the center of the MOT was  $w_0 = \lambda f/(\pi R)$ , where  $f = 38.1$ mm is the focal length of the third lens and  $R$  is the

radius of the beam incident on it. The second lens of the beam expander was mounted on a translation stage (Fig. 2.7). Moving this by 15 mm in 1 s increased the beam size  $R$  thereby compressing the FORT. A tightly focussed trap was essential to increase the elastic collision rate and enhance the evaporative cooling. The cloud of around a million ultracold atoms was then subjected to forced evaporative cooling, where the trap depth was lowered at an exponential rate by reducing the FORT beam intensity. This was done by decreasing the RF power driving the  $\text{CO}_2$  AOM. After 5 s and at a final laser power of 40 mW, a pure condensate of around 30,000 atoms in the  $5S_{1/2}$ ,  $F=1$  state was obtained. To image the BEC, it was released from the FORT and pulsed with the repump beam at full intensity to pump the atoms to the  $F=2$  state. After 8 ms of expansion, a 100ns pulse of light tuned to the resonant  $F=2 \rightarrow F'=3$  transition cast a shadow of the falling condensate on a CCD camera. Subtracting a reference image (without the condensate) from this gave the final distribution of the BEC.

Before we conclude it must be mentioned that aspects of the experimental set-up for kicking and photoassociation are explained in their respective chapters.

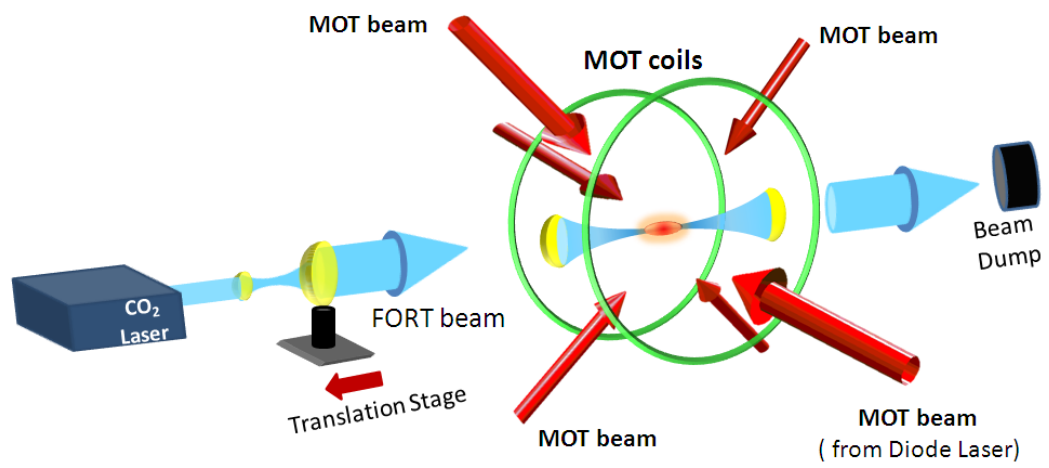


Figure 2.7: Alignment of beams for the Magneto-Optic Trap and the FORT inside the vacuum chamber.

## CHAPTER 3

### Quantum transport with a kicked BEC

Unraveling the details of transport in solid state systems is important for fundamental physics and is becoming particularly relevant for new nanoscopic devices [62, 63]. Atom optic systems offer an easily configurable and ‘clean’ system to study many aspects of it. In this chapter we investigate two models of directed transport in a quantum Hamiltonian. Section 3.1 is on higher order resonances of a quantum accelerator mode, which was discussed in the previous chapter. First, two theoretical approaches of explaining these resonances are described. These are then used to analyze experimental results. In section 3.2, the concept of a quantum-resonance ratchet is discussed. An expression of generalized momentum current is derived. Our realization of such a ratchet is then compared to this theory and the effect of the various experimental parameters studied.

#### 3.1 High-order resonances of a quantum accelerator mode

##### 3.1.1 Rephasing theory

Presence of a linear potential like gravity along the grating leads to the quantum kicked accelerator. In dimensionless units,

$$\hat{H} = \frac{\hat{p}^2}{2} - \frac{\eta}{\tau} \hat{x} + \phi_d \cos(\hat{x}) \sum_{N_p=0}^{\infty} \delta(t - N_p \tau). \quad (3.1)$$

Here,  $\eta = mg'T/\hbar G$  is the unitless ‘gravity’  $g'$ . As seen in the previous chapter, near multiples of the half-Talbot time  $T/T_{1/2}$ , a group of atoms can acquire a fixed momentum with each kick. In general, such accelerator modes can exist near rational

fractions of the Talbot time, that is when  $\tau = 2\pi(a/b)$ . As in section 2.3, and using the definitions of  $\tau$  and  $\eta$ , the phase acquired by the  $q^{\text{th}}$  order is

$$\phi_q = \tau q(p_i + \eta N_p + \frac{1}{2}q) \quad (3.2)$$

where  $p_i = P_i/\hbar G$  is the scaled initial velocity. For these higher order resonances, rephasing occurs between momentum orders separated by  $b\hbar G$  [64]. We can again divide the phase difference between these orders,

$$\phi_q - \phi_{q-b} = \tau b[p_i + \eta N_p + \frac{1}{2}(2q - b)] \quad (3.3)$$

into two parts,

$$\tau b(q + \eta N_p) = 2\pi q a \quad (3.4)$$

$$\tau b(p_i - b/2) = 2\pi l \quad (3.5)$$

the first of which is dependent on the pulse number. Solution of Eq. (3.4) gives the momentum acquired by the accelerator mode,

$$q = -\frac{\eta\tau}{\tau - 2\pi\frac{a}{b}}N_p \quad (3.6)$$

For a primary resonance, ( $a = l'b$ ), the above expression reduces to Eq. (2.20) as expected. Equation (3.5) also imposes a condition on the initial momentum of the atoms in the mode,

$$p_i = \frac{2\pi l}{\tau b} + \frac{b}{2} \quad (3.7)$$

### 3.1.2 $\epsilon$ -classical theory

Fishman, Guarneri, and Rebuzzini (FGR) in 2002 proposed a theory where the de-tuning,  $\epsilon$ , of the pulse period from resonance plays the role of Planck's constant. The map obtained in the classical (or correctly,  $\epsilon$ -classical,  $\epsilon \rightarrow 0$ ) limit of this system was able to successfully explain quantum accelerator modes. It further predicted the existence of higher order modes and spurred the experimental search for them [68].

We review this theory here.

The one period evolution operator or the Floquet operator for the Hamiltonian (3.1) can be written as

$$\hat{U} = \hat{K}\hat{F} = e^{-i\phi_d \cos(\hat{x})} \hat{F} \quad (3.8)$$

The matrix elements of this operator are evaluated in a basis of eigenfunctions of a particle falling under gravity,  $u_E(p) = \langle p|E\rangle$ ,

$$u_E(p) = \left(\frac{\tau}{2\pi\eta}\right)^{1/2} e^{i\frac{\tau}{\eta}(Ep - \frac{p^3}{6})} \quad (3.9)$$

The matrix elements of the free evolution operator are,

$$\begin{aligned} \langle p'|\hat{F}|p''\rangle &= \int dE e^{-E\tau} u_E(p') u_E^*(p'') \\ &= \delta(p' - p'' - \eta) e^{-i\frac{\tau}{2}(p' - \frac{\eta}{2})^2} \end{aligned} \quad (3.10)$$

The kick operator  $\hat{K}$  reads,

$$\langle p|e^{-i\phi_d \cos(\hat{x})}|p'\rangle = \sum_{n=-\infty}^{\infty} (-i)^n J_n \delta(p - p' - n) \quad (3.11)$$

Thus we have the propagator,

$$\begin{aligned} (\hat{U}\psi)(p) &= \int dp' \langle p|\hat{U}|p'\rangle \langle p'|\psi\rangle \\ &= \sum_{n=-\infty}^{\infty} (-i)^n J_n e^{-i\frac{\tau}{2}(p-n-\frac{\eta}{2})^2} \psi(p - n - \eta) \end{aligned} \quad (3.12)$$

The presence of the linear term in the Hamiltonian (3.1) breaks the kicking potential's periodicity, and quasimomentum is no longer conserved. By means of a gauge transformation, spatial periodicity and therefore conservation of the particle quasimomentum,  $\beta$ , can be restored,

$$\hat{H}_g(t) = \frac{1}{2} \left( \hat{p} + \frac{\eta}{\tau} t \right)^2 + \phi_d \cos(\hat{x}) \sum_{N_p=-\infty}^{\infty} \delta(t - N_p \tau). \quad (3.13)$$

This amounts to writing the state in a momentum basis falling freely with the particle,

$$\psi_g(p, N_p) = \langle p + \eta N_p | \hat{U}^{N_p} | \psi \rangle \quad (3.14)$$

where  $\eta N_p$  is the momentum gained due to gravity. The propagator (3.12) in this frame reads,

$$\hat{U}_g(N_p) = e^{-i\phi_d \cos(\hat{x})} e^{-i\frac{\tau}{2}(\hat{p} + \eta N_p + \frac{\eta}{2})^2} \quad (3.15)$$

### The kicked-rotor

We can write the Bloch eigenstates for the above periodic potential as  $e^{i\beta x} \psi_\beta(x)$ , where  $\psi_\beta(x)$  is  $2\pi$  periodic in  $x$ . Introducing an angular co-ordinate  $\theta = x \bmod(2\pi)$ ,  $\psi_\beta(\theta)$  can be considered a fictitious rotor (also called a  $\beta$ -rotor). The angular momentum representation is related to the kicked particle by,

$$\langle n | \psi_\beta \rangle = \langle n + \beta | \psi \rangle \quad (3.16)$$

In the  $\theta$ -representation,

$$\langle \theta | \psi_\beta \rangle = \frac{1}{\sqrt{2\pi}} \sum_n \langle n + \beta | \psi \rangle e^{in\theta} \quad (3.17)$$

The one kick evolution operator for  $|\psi_\beta\rangle$  is

$$\hat{U}_\beta = e^{-i\phi_d \cos(\hat{\theta})} e^{-i\frac{\tau}{2}(\hat{\mathcal{N}} + \beta + \eta N_p + \frac{\eta}{2})^2} \quad (3.18)$$

where the angular momentum operator  $\hat{\mathcal{N}} = -i\frac{d}{d\theta}$  is related to the particle momentum by  $\hat{p} = \hat{\mathcal{N}} + \beta$ .

### Dynamics near a Resonance: $\epsilon$ -Classical treatment

Let us now investigate the rotor dynamics near a resonance and define  $\epsilon = \tau - 2\pi l$  ( $|\epsilon| \ll 1$ ). With  $\tilde{k} = |\epsilon|\phi_d$ , and using  $e^{-i\pi l n^2} = e^{-i\pi l n}$ , the evolution operator (3.18) becomes,

$$\hat{U}_\beta(N_p) = e^{-i\frac{\tilde{k}}{|\epsilon|} \cos \hat{\theta}} e^{-\frac{i}{|\epsilon|} \hat{\mathcal{H}}_\beta(\hat{I}, N_p)}. \quad (3.19)$$

Here we have defined

$$\hat{\mathcal{H}}_\beta(\hat{I}, t) = \frac{1}{2} \frac{\epsilon}{|\epsilon|} (\epsilon) \hat{I}^2 + \hat{I}[\pi l + \tau(\beta + N_p \eta + \frac{\eta}{2})] \quad \text{with} \quad \hat{I} = |\epsilon| \hat{\mathcal{N}} = -i|\epsilon| \frac{d}{d\theta} \quad (3.20)$$

If  $|\epsilon|$  in Eq. (3.19) is treated as a Planck's constant, (3.19) would follow from quantization of the following classical (time-dependent) map,

$$I_{N_p+1} = I_{N_p} + \tilde{k} \sin(\theta_{N_p+1}) \quad \theta_{N_p+1} = \theta_{N_p} + \frac{\epsilon}{|\epsilon|} I_{N_p} + \pi l + \tau(\beta + N_p \eta + \frac{\eta}{2}) \quad (3.21)$$

In other words, as  $\epsilon \rightarrow 0$ , the quantum rotor dynamics can be described in terms of ‘classical rays’ along trajectories of (3.21). This limit has been dubbed “ $\epsilon$ -classical” to distinguish it from the actual  $\hbar \rightarrow 0$  classical limit.

We can define  $J_{N_p} = I_{N_p} + \frac{\epsilon}{|\epsilon|} [\pi l + \tau(\beta + N_p \eta + \frac{\eta}{2})]$  and remove the explicit time dependence,

$$J_{N_p+1} = J_{N_p} + \tilde{k} \sin(\theta_{N_p+1}) + \frac{\epsilon}{|\epsilon|} \tau \eta \quad \theta_{N_p+1} = \theta_{N_p} + \frac{\epsilon}{|\epsilon|} J_{N_p} \quad (3.22)$$

These describe stable periodic orbits on a 2-torus parametrized by  $J$  and  $\theta \pmod{2\pi}$ .

If the orbit has periodicity  $\mathfrak{p}$  (measured in kicks), then

$$J_{\mathfrak{p}} = J_0 + 2\pi \mathfrak{j}, \quad \theta_{\mathfrak{p}} = \theta_0 + 2\pi n \quad (3.23)$$

$\mathfrak{j}$ , called the *jumping index*, gives the number of times the orbit has wound around itself in the  $J$  direction. Figure shows phase space maps of Eq. (3.23) for a primary and two higher order modes.

After  $N_p$  cycles, the physical momentum  $q_{N_p} = I/|\epsilon|$  along this orbit is [67]

$$q_{N_p} \simeq n_0 - \frac{\eta\tau}{\epsilon} N_p + 2\pi \frac{\mathfrak{j}}{\mathfrak{p}|\epsilon|} N_p \quad (3.24)$$

where we have used Eq. (3.23) and the definition of  $J$ . These are trajectories surrounding a ‘stable fixed point’. Together they form an island of stability in the phase space. A wave packet starting with a sizable overlap with such an island grows linearly in momentum with the pulse number (3.24), and forms an ‘accelerator mode’. The mode is characterised by the parameters  $(\mathfrak{p}, \mathfrak{j})$ .



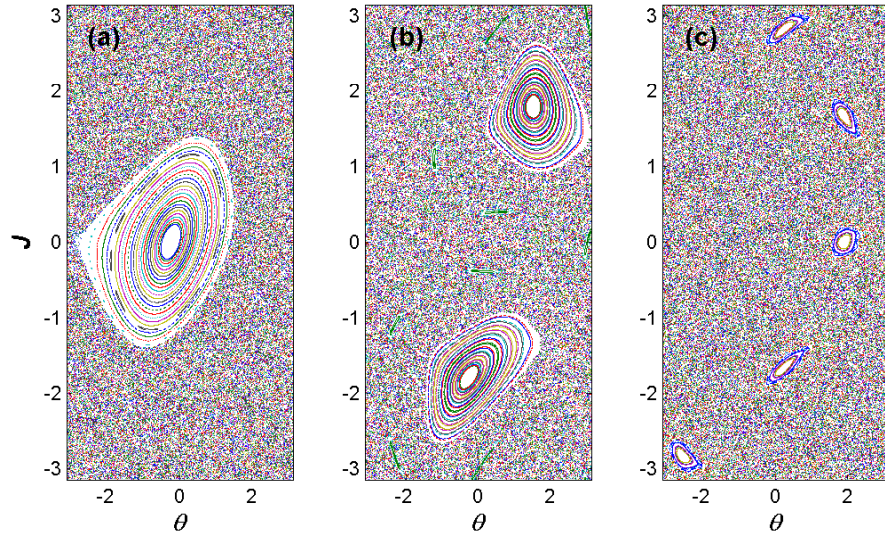


Figure 3.1: Phase space of quantum accelerator modes generated by the map of (3.22) for  $\tau = 5.744$  and  $\phi_d = 1.4$ . Mode (a) with  $(\mathbf{p}, \mathbf{j}) = (1, 0)$  for  $\eta = 2.1459$ , is a primary QAM. Higher order modes are seen in (b) with  $(\mathbf{p}, \mathbf{j}) = (2, 1)$ ,  $\eta = 2.766$ , and (c)  $(\mathbf{p}, \mathbf{j}) = (5, 1)$ ,  $\eta = 4.1801$ .

### $\epsilon$ -classical theory of higher order resonances

Higher order resonances appear near  $\tau = 2\pi a/b$  where  $a, b$  are coprime integers. Near a higher order resonance, we define  $\epsilon = \tau - 2\pi a/b$ . However, in general, no  $\epsilon$ -classical limit exists near these higher order times. Nevertheless, it was shown in Ref. [65] that the QAM's can still be generated, not by a single classical map, but by bundles of “classical rays” which follow the trajectories,

$$\begin{aligned}\theta_{N_p+1} &= \theta_{N_p} + I_{N_p} + \tau(\delta\beta + N_p\eta + \frac{\eta}{2}) + 2\pi S_{N_p}/b \\ I_{N_p+1} &= I_{N_p} - \tilde{k} \sin(\theta_{N_p+1} + 1)\end{aligned}\quad (3.25)$$

where  $\delta\beta = \beta - \beta_r$  gives the closeness to resonant  $\beta_r$ . The integers  $S_{N_p}$  can take integer values between 1 and  $b$  and are arbitrary. The average physical momentum is then,

$$q_{N_p} \simeq -\frac{\eta\tau}{\epsilon}N_p + \left(2\pi\frac{j}{b} - \sum_{r=0}^{T'-1} \Delta S_r\right) \frac{N_p}{T'\epsilon} \quad (3.26)$$

Here,  $\Delta S_r = 2\pi(S_{r+1} - S_r)/b$  and  $T'$  satisfies  $\Delta S_{r+T'} = \Delta S_r$ . For a primary QAM which we investigate experimentally,  $j = 0$ . Also with the simple case of  $\Delta S_r = 0$ , Eq. (3.26) reduces to,

$$q_{N_p} \simeq -\frac{\eta\tau}{\epsilon}N_p \quad (3.27)$$

identical to Eq. (3.6) obtained from the interference model.

#### 3.1.3 Experiment

To experimentally realize such higher order resonances, an initial state was produced in the form of a Bose-Einstein condensate of around 30,000 atoms of Rb87 in the  $F = 1, 5S_{1/2}$  state. The CO<sub>2</sub> beam forming the optical trap was then extinguished and the condensate released from the trap. The kicking beams were derived from a slave laser injection locked to the  $F = 2 \rightarrow F' = 3$  transition frequency of the master laser. It was thus 6.8 GHz red-detuned with respect to the condensate atoms

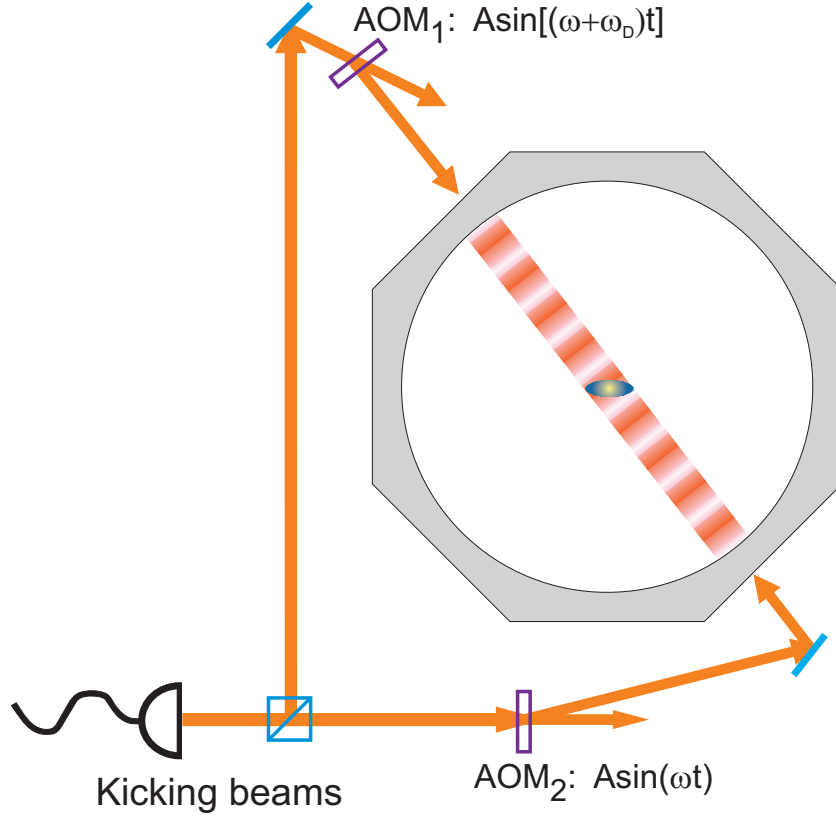


Figure 3.2: Set-up for the kicking experiments. Two counterpropagating beams formed the standing wave oriented at an angle of  $52^\circ$  to the vertical. AOM<sub>2</sub> was driven by an RF signal with a fixed frequency,  $\omega/2\pi = 40\text{MHz}$ .

(Fig. 2.5). An optical fiber transported this beam from the optical table to the BEC table where it was divided into two by a 50-50 beam splitter cube. Each of these beams had 25 mW of power and was directed into an acousto-optic modulator (Isomet model 40N). The frequency of the first order beam diffracted by the AOM is Doppler shifted by an amount equal to the frequency of the acoustic wave in the AOM. The acoustic wave was generated by an RF electrical signal supplied by an arbitrary waveform generator HP8770A after amplification. One of the AOMs was driven at a fixed 40 MHz while the other had a variable frequency input from a second HP8770A which was phase-locked to the first generator. By adjusting the variable part of this frequency,  $\omega_D = \frac{2\pi}{T_{1/2}}\beta + \frac{1}{2}Gat$ , the initial momentum  $\beta$ , and acceleration  $a$ , of the standing wave relative to the condensate could be changed. A schematic of the kicking set-up is shown in Fig. 3.2. After the application of the kicking sequence, the condensate was allowed to expand for 8 ms to allow the diffracted momentum orders to separate before imaging.

Pulse lengths of  $1.8 \mu s$  were used for the kicks. The probability of the  $n^{\text{th}}$  momentum order getting populated is  $|J_n(\phi_d)|^2$ . Thus, by examining a distribution after one kick, the strength  $\phi_d$  of a kick was inferred to be  $\approx 1.5$ .

Figure 3.3 depicts the evolution of a QAM as a function of kicks. The plots show horizontally stacked distributions with increasing pulse number near a resonance time. Figure 3.3(a) is a kick scan performed at  $T = 22.68 \mu s$ , close to the resonance at  $(2/3)T_{1/2}$  [70]. The linear growth of a QAM with orders separated by  $3\hbar G$  can be seen. This behavior where states separated by  $b\hbar G$  rephase to form the  $b^{\text{th}}$  order resonance is expected from the fractional Talbot effect [71]. The effect is clearer in Fig. 3.3(b) which is near the resonance at  $(1/2)T_{1/2}$  with a pulse separation of  $T = 17.1 \mu s$ . Figure 3.3(c) is at the Talbot time  $(2T_{1/2})$ , where the QAM can be seen to comprise of neighboring momentum states.

Next, time scans across two high-order resonances at  $(1/2)T_{1/2}$  and  $(1/3)T_{1/2}$  are

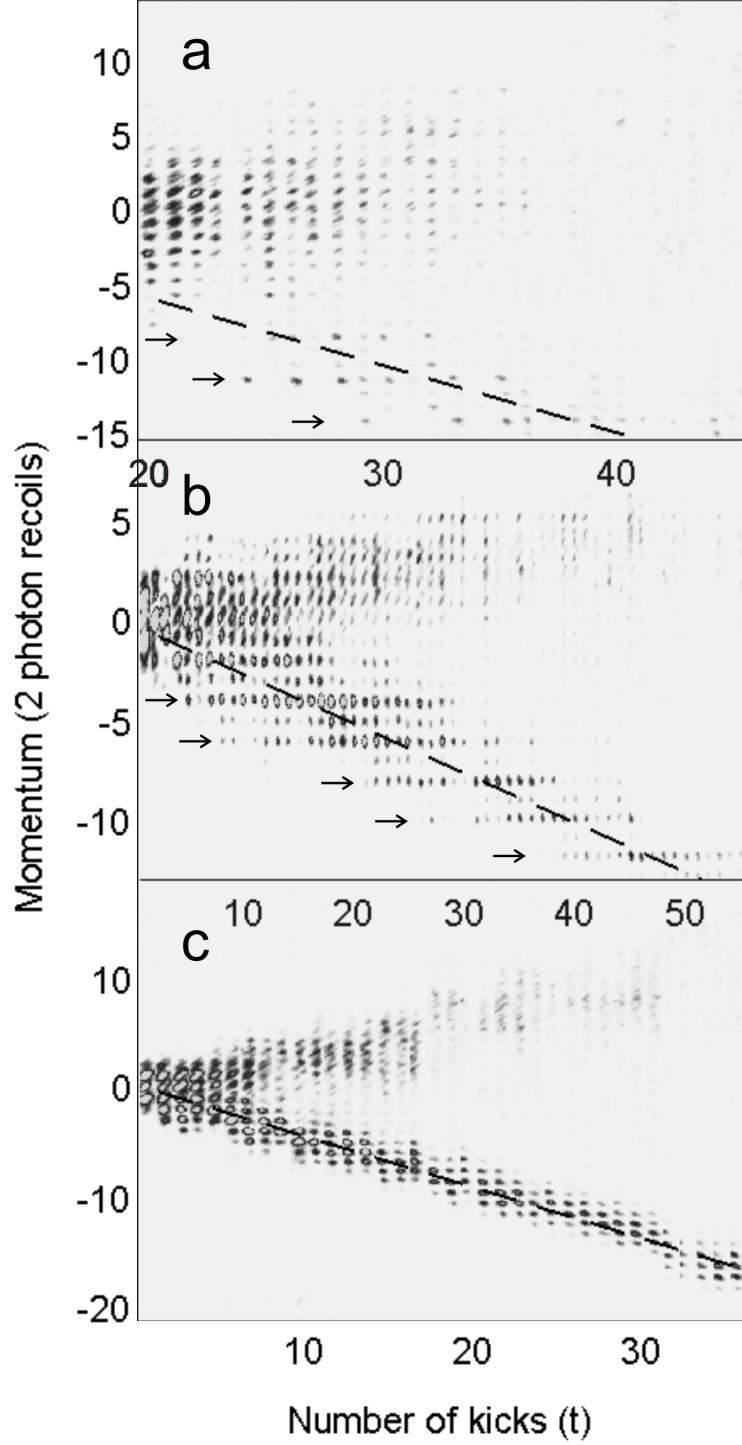


Figure 3.3: Quantum accelerator modes at (a)  $T=22.68 \mu s$  close to  $(2/3)T_{1/2}$ , (b)  $T=17.1 \mu s$  which is close to  $(1/2)T_{1/2}$ , and (c)  $T=72.4 \mu s$  close to  $2T_{1/2}$ . a value of  $g'=6 \text{ ms}^{-2}$  was used in these scans. The arrows in (a) and (b) show orders separated by  $b\hbar G$  which participate in the QAMs. Dashed lines correspond to the  $\epsilon$ -classical theory of Eq. (3.27)

shown in Figs. 3.4(a) and (b) respectively. The dashed curves are Eq. (3) demonstrating a good fit with the  $\epsilon$ -classical theory. The relatively weak experimental signal for the resonance at  $(1/3)T_{1/2}$  is also noticed in Fig. 3.4. This difficulty in creating a high-order QAM stems from the high kicking strength  $\phi_d$  needed to populate states comparable to  $b\hbar G$ . It can be seen from the fact that the population of the state  $b\hbar G$  is proportional to  $|J_b(\phi_d)|^2$  with a maximum at  $b \sim \phi_d$ . This high value of  $\phi_d$  has the unwanted effect of increasing the distribution of states not participating in the QAM, thereby masking the presence of a QAM.

Finally, the dependence of QAM on the initial momentum of the BEC was investigated by moving the standing wave using the variable frequency of a kicking AOM. The initial momentum scans performed near resonances at  $(1/2)T_{1/2}$  and  $(2/3)T_{1/2}$  are shown in Fig. 3.5(a) and (b) respectively. The QAM appears once every  $1\hbar G$  of initial momentum at  $(1/2)T_{1/2}$  and twice at  $(2/3)T_{1/2}$ . To understand this, we can use Eq. (3.7) to obtain the separation in initial momenta for a QAM to be  $\Delta p_i = 2\pi/\tau b \approx 1/a$ . Thus our experimental results bear out the predictions of the theory of high-order resonances.

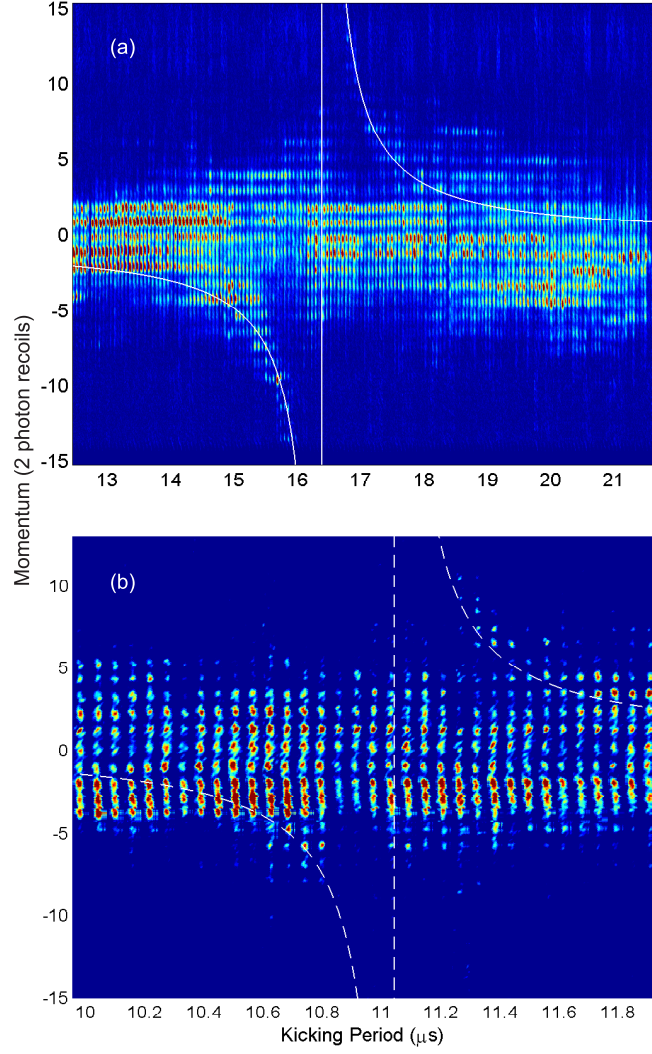


Figure 3.4: Horizontally stacked momentum distributions across (a)  $(1/2)T_{1/2}$  for 40 kicks,  $\phi_d = 1.4$  and effective acceleration  $g' = 6 \text{ ms}^{-2}$ ; and (b)  $(1/3)T_{1/2}$  for 30 kicks,  $\phi_d = 1.8$ , and  $g' = 4.5 \text{ ms}^{-2}$ . The dashed curve is a fit to the theory in Eq. (3.27)

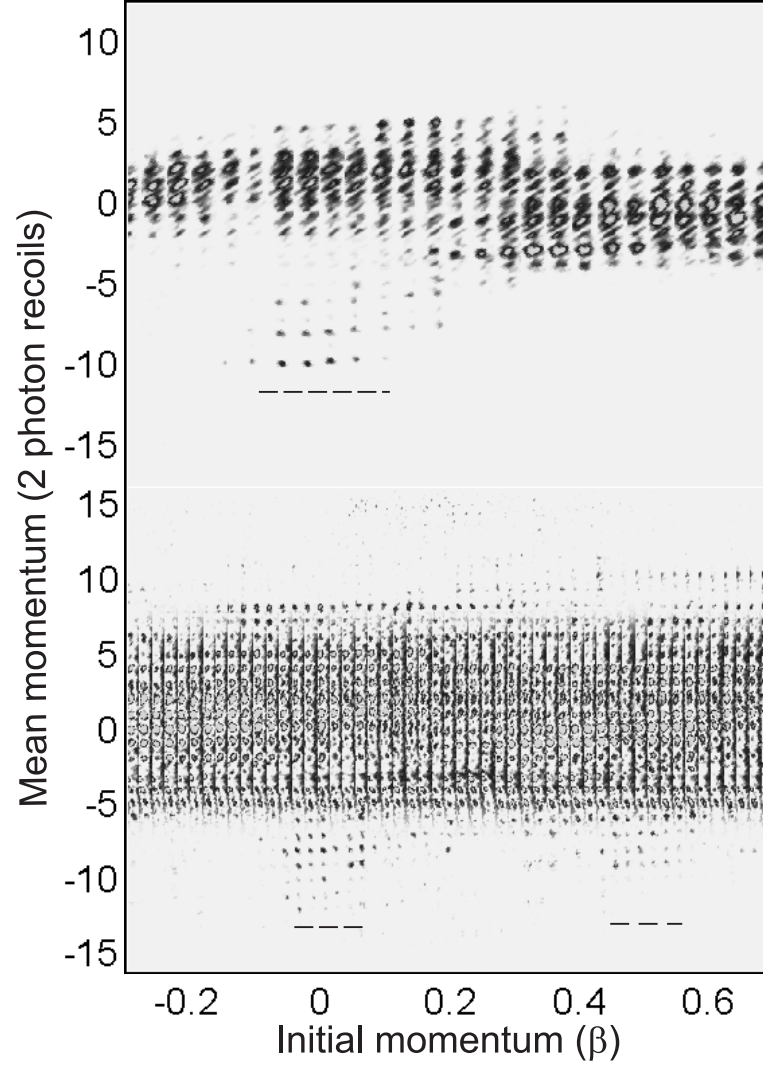


Figure 3.5: Initial momentum scans for QAMs near (a)  $(1/2)T_{1/2}$  ( $T=17.1 \mu s$ ) for 30 kicks and  $g'=6 \text{ ms}^{-2}$ ; and (b)  $(2/3)T_{1/2}$  ( $T=22.53 \mu s$ ) with 40 kicks and  $g'=4.5 \text{ ms}^{-2}$ . The dashes indicate QAMs at the resonant  $\beta$ .



### 3.2 A quantum ratchet

Feynmann in his classic Lectures on Physics [72] discussed the concept of a ratchet, and demonstrated how directed motion could not be extracted from a spatially asymmetric system kept in thermal equilibrium. However away from equilibrium, a ratchet current, defined as directed transport in a spatially periodic system with no bias field, becomes a possibility [73]. The best examples of this are seen in nature in the form of biological motors which can use thermal fluctuations to establish a particulate current. Hamiltonian ratchets, where deterministic chaos replaces dissipation to drive motion, have recently gathered theoretical and experimental interest. For instance, asymmetric dynamical localization led to a unidirectional current in a kicked rotor with spatiotemporal asymmetry [75]. The possibility of using a resonance of a kicked rotor with a broken spatial symmetry was shown in [74] and subsequently observed experimentally [26]. We realize such a quantum ratchet at arbitrary initial momenta (quasimomentum) and investigate its various parameter dependencies.

The initial state is prepared as a superposition of the momentum states

$$|\psi_0\rangle = \frac{1}{\sqrt{2}}[|0\rangle + |1\rangle] \quad (3.28)$$

With Eq. (3.17), we can express this as a rotor state,

$$\psi_0(\theta) = \frac{1}{\sqrt{4\pi}}[1 + e^{i\theta}] \quad (3.29)$$

After a time  $T$ , the 1<sup>st</sup> order picks up a phase  $\gamma = \frac{(\hbar G)^2}{2m\hbar}T$ . Equivalently, the free evolution can be substituted by a translation of the grating from  $\cos(\theta) \rightarrow \cos(\theta - \gamma)$ . We shall adopt this latter approach in the analysis below, and the experiments thereafter, where an offset kicking potential  $V(\theta) = \cos(\theta - \gamma)$  is applied on the initial state. The one period evolution operator for the Hamiltonian  $\hat{H} = \frac{\hat{p}^2}{2} + \phi_d \cos(\hat{x}) \sum_{N_p=0}^{\infty} \delta(t - N_p\tau)$  is given by (Eq. 3.18 with  $\eta = 0$ ),

$$\hat{U}_\beta = e^{-i\phi_d V(\hat{\theta})} e^{-i\tau(\hat{N}+\beta)^2/2}$$

$$= e^{-i\phi_d \cos(\hat{\theta}-\gamma)} e^{-i\hat{\mathcal{N}}\tau_\beta} \quad (3.30)$$

Here we have ignored an irrelevant phase factor and  $\tau_\beta = \pi l_0(2\beta + 1)$  with  $l_0$  an integer. After  $N_p$  kicks,

$$\begin{aligned} \psi_{N_p}(\theta) &= \hat{U}_\beta^{N_p} \psi_0(\theta) \\ &= \hat{U}_\beta^{N_p-1} e^{-i\phi_d \cos(\hat{\theta}-\gamma)} \psi_0(\theta - \tau_\beta) \\ &= \hat{U}_\beta^{N_p-2} e^{-i\phi_d \cos(\hat{\theta}-\gamma)} e^{-i\phi_d \cos(\hat{\theta}-\gamma-\tau_\beta)} \psi_0(\theta - 2\tau_\beta) \\ &= e^{-i\phi_d \sum_{s=0}^{N_p-1} \cos(\hat{\theta}-\gamma-s\tau_\beta)} \psi_0(\theta - N_p\tau_\beta) \\ &= e^{[-i\phi_d \frac{\sin(\tau_\beta N_p/2)}{\sin(\tau_\beta/2)} \cos\{\theta - (N_p-1)\frac{\tau_\beta}{2} - \gamma\}]} \psi_0(\theta - N_p\tau_\beta) \end{aligned} \quad (3.31)$$

where we have used the relation  $\sum_{s=0}^{t-1} e^{as} = (1 - e^{at})/(1 - e^a)$  in the last step.

The momentum current at time  $N_p$  is,

$$\begin{aligned} \langle \hat{\mathcal{N}} \rangle_{N_p} &\equiv \langle \psi_{N_p} | \hat{\mathcal{N}} | \psi_{N_p} \rangle \\ &= -i \int_0^{2\pi} d\theta \psi_{N_p}^*(\theta) \frac{d\psi_{N_p}(\theta)}{d\theta} \\ &= -i \int_0^{2\pi} d\theta \left[ i\phi_d \frac{\sin(\tau_\beta N_p/2)}{\sin(\tau_\beta/2)} \sin\left\{\theta - (N_p-1)\frac{\tau_\beta}{2} - \gamma\right\} |\psi_0(\theta - N_p\tau_\beta)|^2 \right. \\ &\quad \left. + \psi_0^*(\theta - N_p\tau_\beta) \psi_0'(\theta - N_p\tau_\beta) \right] \end{aligned} \quad (3.32)$$

Here the prime denotes a derivative with respect to  $\theta$ . Using the initial state (3.29) and identifying the second term as the mean momentum of the initial state, the change in the momentum current is [76],

$$\begin{aligned} \Delta \langle \hat{p} \rangle_{N_p} &= \langle \hat{\mathcal{N}} \rangle_{N_p} - \langle \hat{\mathcal{N}} \rangle_0 \\ &= \frac{\phi_d \sin(\tau_\beta N_p/2)}{2 \sin(\tau_\beta/2)} \sin[(N_p+1)\tau_\beta/2 - \gamma] \end{aligned} \quad (3.33)$$

When  $\tau_\beta \rightarrow 2r\pi$ , where  $r$  is an integer, we obtain a linear growth in the current, a ratchet acceleration:

$$\Delta \langle \hat{p} \rangle_{N_p, r} = -\frac{\phi_d}{2} \sin(\gamma) N_p. \quad (3.34)$$

At this point we would like to note that for a plane wave initial state, the integral of the first term in (3.32) vanishes and there is no change in the momentum current from its initial value. This explains our choice of the special superposition initial state (3.29) to create a ratchet. Of course one has to account for the finite initial momentum width of the condensate in an experiment. Towards this end we consider a condensate with a Gaussian distribution,  $\frac{1}{\sqrt{2\pi(\Delta\beta)^2}} \exp[-\frac{(\beta' - \beta)^2}{2(\Delta\beta)^2}]$ , where  $\beta$  and  $\Delta\beta$  are the average and standard deviation respectively. The average of the momentum current (3.33) over  $\beta = \beta'$  is [27, 77],

$$\langle \Delta \langle \hat{p} \rangle_{N_p} \rangle_{\Delta\beta} = \frac{\phi_d}{2} \sum_{s=1}^{N_p} \sin(\tau_\beta s - \gamma) \exp[-2(\pi l_0 \Delta\beta s)^2] \quad (3.35)$$

On resonance, that is when  $\tau_\beta = 2r\pi$ , Eq. (3.35) reduces to

$$\langle \Delta \langle \hat{p} \rangle_{N_p} \rangle_{\Delta\beta} = -\frac{\phi_d}{2} \sin(\gamma) \sum_{s=1}^{N_p} \exp[-2(\pi l_0 \Delta\beta s)^2] \quad (3.36)$$

### 3.2.1 Experiment

The experimental configuration was similar to that used to observe quantum accelerator modes but with  $\eta = 0$ . The initial state was prepared by applying a weak but long pulse (duration of 38  $\mu\text{s}$ ) to the released condensate. This resulted in a Bragg diffraction of the atoms into an equal superposition of the  $|0\hbar G\rangle$  and  $|1\hbar G\rangle$  states. This was followed by short (2  $\mu\text{s}$ ) kicks of the rotor, each with a strength  $\phi_d \sim 1.4$ . To produce an offset  $\gamma$ , the standing wave was shifted by changing the phase of the variable kicking AOM.

A systematic study was done to experimentally determine the parameter dependence of a quantum ratchet. We worked at the first quantum resonance where  $\tau_\beta = 2\pi$ , corresponding to the half-Talbot time,  $T_{1/2}$ . This gives a resonant  $\beta$  of 0.5 (for  $l_0 = 1$ ). Figure 3.6 shows the mean momentum as a function of the offset phase,  $\gamma$ , after 5 kicks on the initial state. The largest change in momentum was at  $\gamma = \pi/2, 3\pi/2$  etc. This can be seen classically as a maximum gradient of the optical potential acting on

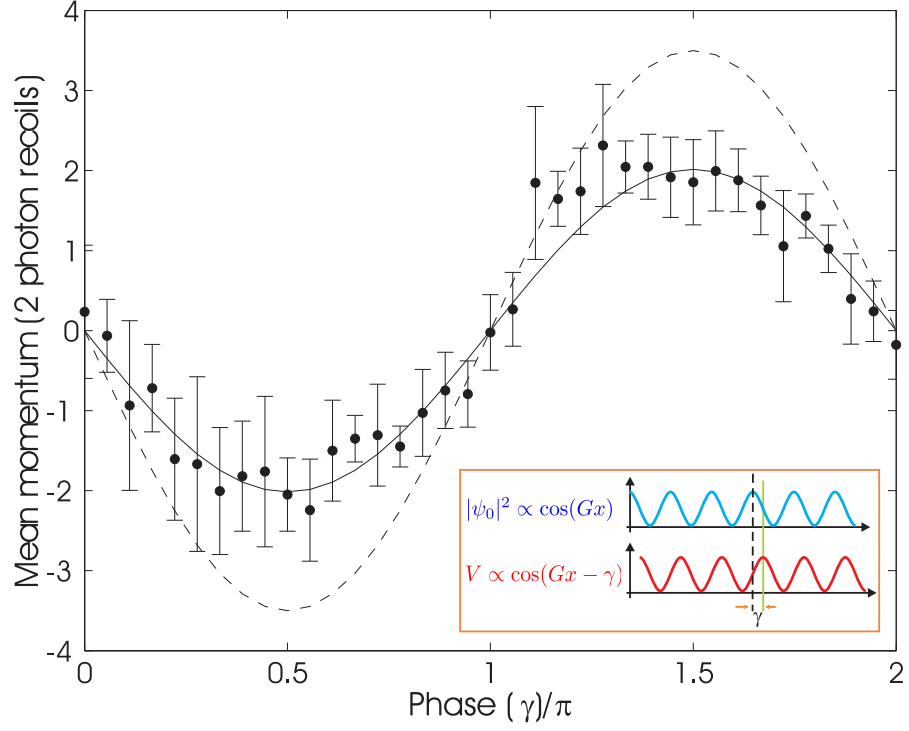


Figure 3.6: Dependence of the mean momentum of the quantum ratchet on the offset angle  $\gamma$  for 5 kicks and  $\beta = 0.5$ . The dashed and solid lines represent Eqs. (3.33) and (3.36) respectively. The inset shows the offset  $\gamma$  created between the symmetry centers of the initial distribution (blue curve) and the kicking potential  $V$  (red curve).

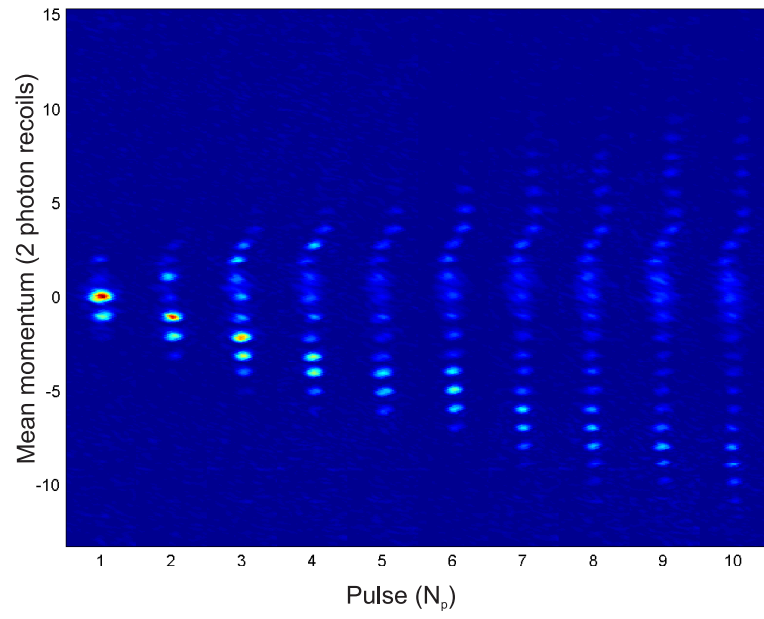


Figure 3.7: The ratchet effect. This time of flight image shows growth of mean momentum with each standing wave pulse applied with a period of  $T_{1/2}$  and a maximum offset ( $\gamma = \pi/2$ ) between the standing wave and the initial state.

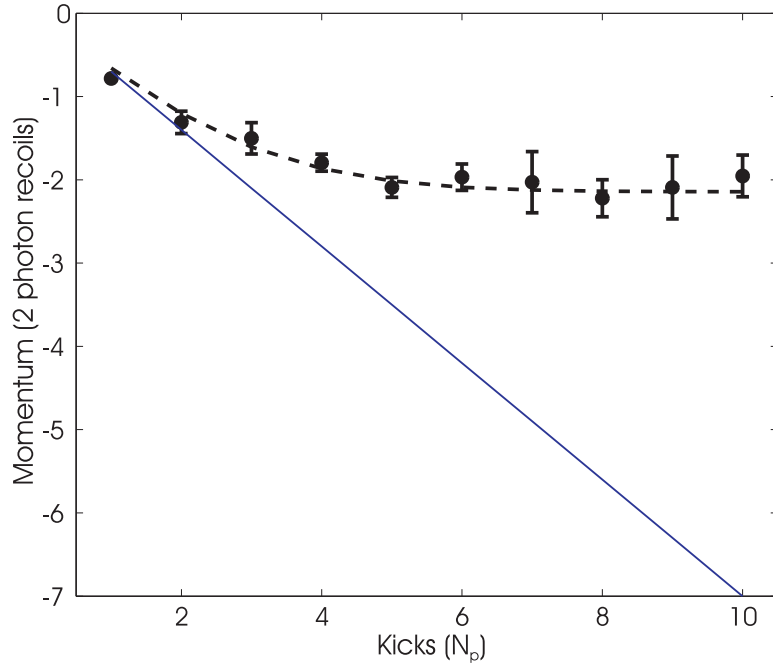


Figure 3.8: Mean momentum as a function of kicks. The data and error bars are from experiments with  $\phi_d = 1.4, \gamma = \pi/s$  and  $\beta = 0.5$ . The solid line is Eq. (3.33) while the dashed line corresponds to Eq. (3.36).

the atomic distribution when it is displaced by an integer multiple of  $\gamma = \pi/2$  (Fig. 3.6). The ratchet effect can be seen clearly in the time of flight image of Fig. 3.7 at  $\gamma = \pi/2$ . The mean momentum as a function of kicks is plotted in Fig. 3.8, and exhibits a saturation of the ratchet acceleration. A fit of the mean momentum in Figs. 3.6 and 3.8 to Eq. (3.36) yields a value of  $\Delta\beta = 0.056$ . This value is consistent with a condensate momentum width measured using a time-of-flight technique. Finally, with  $\gamma = \pm\pi/2$ , the dependence of the mean momentum on  $\beta$  is depicted in Fig. 3.9. As expected, a pronounced ratchet effect is seen at the resonant  $\beta = 0.5$  but is suppressed overall due to the finite  $\Delta\beta$ .

Thus, we realized a quantum-resonance ratchet by applying periodic kicks from a symmetric optical potential on a superposition state. An asymmetry introduced between the centers of the initial state and the kicking potential created a ratchet current (Fig. 3.6), with a maximum magnitude at  $\gamma = \pm\pi/2$ . A linear growth in momentum was observed at the resonant  $\beta = 0.5$ , but was found to be suppressed by the finite momentum width of the BEC. It is therefore desirable to reduce  $\Delta\beta$  to obtain a higher ratchet current.

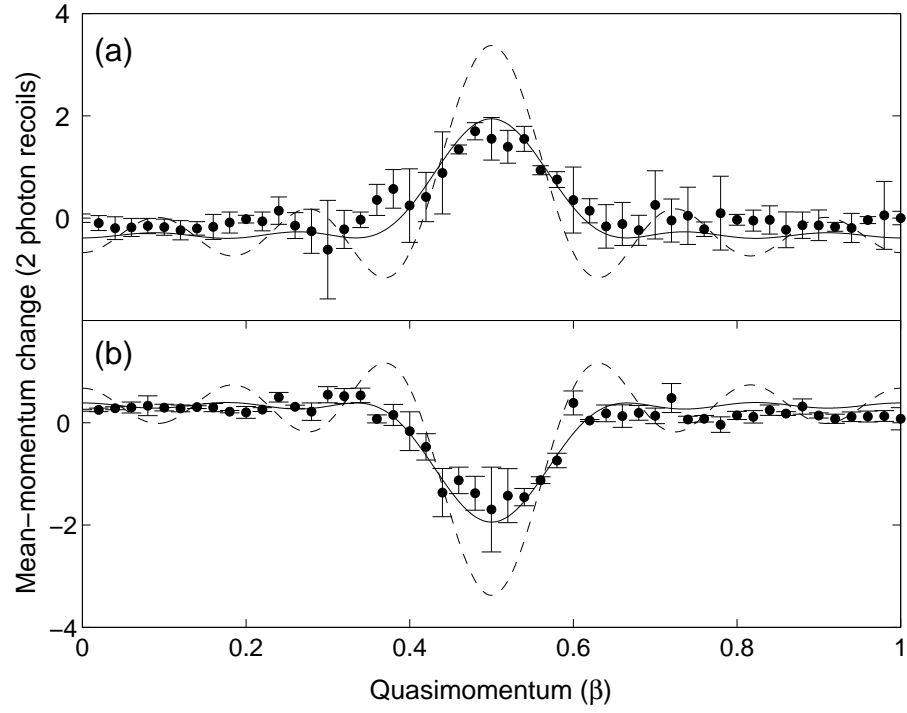


Figure 3.9: Change in mean momentum vs the quasimomentum  $\beta$  for  $\phi_d = 1.4$  and (a)  $\gamma = -\pi/2$ , (b)  $\gamma = \pi/2$ . Shown are the fits of Eqs. (3.33), dashed line and (3.36), solid line respectively to the experimental data (filled circles).



## CHAPTER 4

### Sub-Fourier resonances of the kicked rotor

A discrete Fourier transform of input test signals was recently performed with a BEC in an optical lattice [78]. The resultant frequency spectra were resolved more accurately than possible by classical Fourier analysis. Such examples exploit the non-linear response of the quantum system to an excitation. For instance, the linewidth of the  $n^{\text{th}}$  harmonic of a multiphoton Raman resonance was shown to be  $n$ -fold narrower than the Fourier transform linewidth of the driving optical pulse [79]. In another demonstration, dynamical localization in the classically chaotic regime of the quantum kicked rotor was utilized to discriminate between two driving frequencies with a sub-Fourier resolution [28]. At a primary quantum resonance at the Talbot time, adjacent momentum orders evolve in phases which are integer multiples of  $2\pi$ . As we saw in chapter 2, this leads to a quadratic growth in mean energy,  $\langle E \rangle = 2\pi E_r \phi_d^2 N^2$  where  $E_r = \hbar^2 G^2 / 8M$  is the photon recoil energy. The width of mean energy distribution around the resonance time was found to decrease with kicks and kicking strength as  $1/(N^2 \phi_d)$  [91]. This sub-Fourier behavior was attributed to the non-linear nature of the quantum delta kicked rotor and explained using the  $\epsilon$ -classical theory [80].

High-precision measurements using quantum mechanical principles have been carried with atom interferometers for many years [81]. Such devices were used to determine the Earth's gravitational acceleration [82–84], fine structure constant  $\alpha$  [86–88], and the Newtonian constant of gravity [89]. The promise of the QDKR as a candidate for making these challenging measurements has begun to be realized [29]. Recently a scheme was proposed for measuring the overlap or fidelity between a near-resonant

$\delta$ -kicked rotor state and a resonant state via application of a tailored pulse at the end of a rotor pulse sequence [90]. It predicted a  $1/N^3$  scaling of the temporal width of the fidelity peak. In this chapter we describe our observation of such fidelity resonance peaks and their sub-Fourier nature. In section 4.1 we discuss the theory. We also calculate the effect of gravity on such a measurement. Section 5.7 details the experimental configuration and the results.

#### 4.1 A fidelity measurement on the QDKR

We begin with the evolution of a state  $|\psi_0\rangle$  due to  $N$  kicks at a period near the Talbot time, i.e.,  $\tau = 4\pi + \epsilon$ ,

$$\begin{aligned} |\psi_f\rangle &= \hat{U}^N |\psi_0\rangle \\ &= \sum_n c_n |n\rangle \end{aligned} \quad (4.1)$$

where the  $|n\rangle$  are momentum eigenstates in units of  $\hbar G$ . The effect of the deviation from resonance (to the first order in  $\epsilon$ ), results in a change of the phase of the complex coefficients  $c_n = A_n(\epsilon) \exp\{i\theta_n(\epsilon)\}$ ,

$$\begin{aligned} c_n(\epsilon) &\simeq c_n(0) \exp\left(i \frac{\partial \theta_n}{\partial \epsilon} \Big|_{\epsilon=0} \epsilon\right) \\ &= (-i)^n J_n(\phi_d) \exp\left(i \frac{\partial \theta_n}{\partial \epsilon} \Big|_{\epsilon=0} \epsilon\right) \end{aligned} \quad (4.2)$$

$c_n(0)$  are the resonant coefficients as seen in Eq. (2.10). We notice that a measurement of the mean energy  $\langle E \rangle = \frac{1}{2} \sum_n n^2 p_n$  for the distribution  $p_n = |\langle n | \psi \rangle_f|^2$  will not detect these phases.

To probe the effect of these phase changes, Ref. [90] proposed a measurement of the projection of this final off-resonant state onto the resonant state. To this end one can define a “fidelity”,

$$F = |\langle \psi_0 | \hat{U}_r \hat{U}^N | \psi_0 \rangle|^2 \quad (4.3)$$

where  $\hat{U} = \exp(-i\frac{\tau}{2}\hat{p}^2) \exp[-i\phi_d \cos(\hat{x})]$  and  $\hat{U}_r = \exp[iN\phi_d \cos(\hat{x})]$ . Experimentally,  $\hat{U}_r$  can be implemented with a kick changed in phase by  $\pi$  and carrying a strength of  $N\phi_d$ . Note that on resonance,  $\exp(-i\frac{\tau}{2}\hat{p}^2) = 1$  and the final state is the same as the initial.  $F$  therefore measures the probability of revival of the initial state as a function of these deviations. Using Eqs. (4.1) and (4.2), the fidelity can be expressed as,

$$F \simeq \left| \sum_n J_n^2(N\phi_d) \exp(i\Theta_n) \right|^2 \quad (4.4)$$

Here we have introduced

$$\Theta_n = \frac{\partial \theta_n}{\partial \epsilon} \Big|_{\epsilon=\beta=\eta=0} \epsilon + \frac{\partial \theta_n}{\partial \beta} \Big|_{\epsilon=\beta=\eta=0} \beta + \frac{\partial \theta_n}{\partial \eta} \Big|_{\epsilon=\beta=\eta=0} \eta \quad (4.5)$$

to account for the general case of phases accruing from deviations in resonant time ( $\epsilon$ ), initial momentum ( $\beta$ ) or a non-zero gravity ( $\eta$ ).

This perturbative treatment was used to show that near the Talbot time,  $\tau = 4\pi$ , the fidelity is [90]

$$F(\epsilon, \beta = 0, \eta = 0) \simeq J_0^2 \left( \frac{1}{12} N^3 \phi_d^2 \epsilon \right) \quad (4.6)$$

The width of such a peak in  $\epsilon$  therefore changes as  $1/(N^3 \phi_d^3)$ , displaying a sub-Fourier dependence on the measurement time, expressed here in units of kicks,  $N$ . We now investigate the behavior of the fidelity in the presence of a linear potential like gravity.

#### 4.1.1 Effect of ‘gravity’

For a perturbation only due to gravity,

$$\Theta_n = \frac{\partial \theta_n}{\partial \eta} \Big|_{\epsilon=\beta=\eta=0} \eta \quad (4.7)$$

Equation (4.2) can be rearranged as,

$$\frac{\partial \theta_n}{\partial \eta} \Big|_{(\epsilon=\beta=\eta=0)} = \frac{\frac{\partial c_n}{\partial \eta} \Big|_{(\epsilon=\beta=\eta=0)}}{i c_n(0, 0, 0)} \quad (4.8)$$

Coefficients  $c_n$  are

$$c_n(\epsilon, \beta, \eta) = \langle n + \beta | \hat{U}_{g_N} \dots \hat{U}_{g_2} \hat{U}_{g_1} | \beta \rangle \quad (4.9)$$

$\hat{U}_{g_i} = \exp[-i\frac{\tau}{2}(\hat{p} + t\eta + \frac{\eta}{2})^2] \exp[-i\phi_d \cos(\hat{x})]$  is the  $t^{\text{th}}$  kick evolution operator in the freely falling frame which was introduced in section (3.1.2) obtained after a gauge transformation of the QDKA Hamiltonian.

After 3 kicks on the initial zero momentum eigenstate,

$$\begin{aligned} \frac{\partial c_n}{\partial \eta}|_{(\epsilon=\beta=\eta=0)} &= \langle n | \frac{\partial \hat{U}_{g_3}}{\partial \eta} \hat{U}_{g_2} \hat{U}_{g_1} + \hat{U}_{g_3} \frac{\partial \hat{U}_{g_2}}{\partial \eta} \hat{U}_{g_1} + \hat{U}_{g_3} \hat{U}_{g_2} \frac{\partial \hat{U}_{g_1}}{\partial \eta} | 0 \rangle |_{(\epsilon=\beta=\eta=0)} \\ &= -\frac{2i\tau}{2} \langle n | (\hat{p} + 3\eta + \frac{\eta}{2})(3 + \frac{1}{2}) \exp(-i\phi_d \cos \hat{x}) \hat{U}_{g_2} \hat{U}_{g_1} + \\ &\quad \hat{U}_{g_3} (\hat{p} + 2\eta + \frac{\eta}{2})(2 + \frac{1}{2}) \exp(-i\phi_d \cos \hat{x}) \hat{U}_{g_1} + \\ &\quad \hat{U}_{g_3} \hat{U}_{g_2} (\hat{p} + 1\eta + \frac{\eta}{2})(1 + \frac{1}{2}) \exp(-i\phi_d \cos \hat{x}) | 0 \rangle |_{(\epsilon=\beta=\eta=0)} \\ &= -i\tau \langle n | e^{-i\phi_d(1-1) \cos \hat{x}} \hat{p} (3 + \frac{1}{2}) e^{-i\phi_d(3+1-1) \cos \hat{x}} + \\ &\quad e^{-i\phi_d(2-1) \cos \hat{x}} \hat{p} (2 + \frac{1}{2}) e^{-i\phi_d(3+1-2) \cos \hat{x}} + \\ &\quad e^{-i\phi_d(3-1) \cos \hat{x}} \hat{p} (1 + \frac{1}{2}) e^{-i\phi_d(3+1-3) \cos \hat{x}} | 0 \rangle \end{aligned}$$

Therefore for  $N$  kicks,

$$\frac{\partial c_n}{\partial \eta}|_{(\epsilon=\beta=\eta=0)} = -i\tau \sum_{r=1}^N b_{n,r} \quad (4.10)$$

where

$$b_{n,r} = \langle n | e^{-i\phi_d(r-1) \cos \hat{x}} \hat{p} (N - r + \frac{3}{2}) e^{-i\phi_d(N+1-r) \cos \hat{x}} | 0 \rangle \quad (4.11)$$

We make an observation here. Equation (4.11) can be expanded as  $b_{n,r} = (N - r + \frac{3}{2}) \sum_{m=-\infty}^{\infty} m^2 J_m[(N+1-r)\phi_d] J_{m-n}[(r-1)\phi_d] \frac{(-1)^m}{(-i)^n}$ . This expression and Eq. (4.10) show that, a first order perturbation in  $\eta$  can be viewed as a rotation in the complex plane (real  $\rightarrow$  imaginary and vice versa). Similar results hold for deviations from resonant  $\epsilon$  and  $\beta$  and explain the basis of assumption (4.2).

We now return back to evaluate (4.10) with (4.11),

$$\frac{\partial c_n}{\partial \eta}|_{(\epsilon=\beta=\eta=0)} = -i\tau \phi_d \sum_{r=1}^N (N - r + \frac{3}{2})(N + 1 - r) \langle n | e^{-i\phi_d(r-1) \cos \hat{x}} \sin \hat{x} e^{-i\phi_d(N-1+r) \cos \hat{x}} | 0 \rangle$$

$$\begin{aligned}
&= -i\tau\phi_d\langle n|\sin\hat{x} e^{-iN\phi_d\cos\hat{x}}|0\rangle\sum_{r=1}^N(N-r+\frac{3}{2})(N+1-r) \\
&= \frac{i\tau}{2i}\phi_d\langle n|(e^{i\hat{x}}-e^{-i\hat{x}})e^{-iN\phi_d\cos\hat{x}}|0\rangle\sum_{r=1}^N(N-r+\frac{3}{2})(N+1-r) \\
&= \frac{\tau}{2}\phi_d(\langle n+1|-\langle n-1|)\{\sum_l(-i)^l J_l(N\phi_d)|l\rangle\}\sum_{r=1}^N(N-r+\frac{3}{2})(N+1-r) \\
&= \frac{\tau}{2}\phi_d[(-i)^{n+1}J_{n+1}(N\phi_d)-(-i)^{n-1}J_{n-1}(N\phi_d)]\sum_{r=1}^N(N-r+\frac{3}{2})(N+1-r) \\
&= -\frac{i\tau n}{N}(-i)^n J_n(N\phi_d)\sum_{r=1}^N(N-r+\frac{3}{2})(N+1-r) \tag{4.12}
\end{aligned}$$

using  $J_{n+1}(x) = \frac{2n}{x}J_n(x) - J_{n-1}(x)$ .

This gives us,

$$\begin{aligned}
\frac{\partial\theta_n}{\partial\eta}|_{(\epsilon=\beta=\eta=0)} &= \frac{\frac{\partial c_n}{\partial\eta}|_{(\epsilon=\beta=\eta=0)}}{ic_n(0,0,0)} \\
&= -\tau n[N^2 + \frac{5}{2}N + \frac{3}{2} + \frac{(N+1)}{2}\{\frac{2N+1}{3} - (2N + \frac{5}{2})\}]
\end{aligned}$$

Keeping only terms in  $N^2$ ,

$$\begin{aligned}
\frac{\partial\theta_n}{\partial\eta}|_{(\epsilon=\beta=\eta=0)} &= -\tau n\frac{N^2}{3} \\
&= -\frac{4\pi}{3}nN^2 \tag{4.13}
\end{aligned}$$

Therefore, the fidelity is

$$\begin{aligned}
F(\eta, \epsilon = \beta = 0) &\simeq |\sum_n J_n^2(N\phi_d) \exp(i\frac{\partial\theta_n}{\partial\eta}\eta)|^2 \\
&= \sum_n J_{-n}(N\phi_d)J_n(N\phi_d) \exp\{i(-\Delta + \pi)n\}^2
\end{aligned}$$

where we have used result (4.13) to define  $\Delta = \frac{4\pi}{3}N^2\eta$  and used the Bessel function property,  $J_{-m}(x) = (-1)^m J_m(x)$ . Finally with the help of Graf's identity,  $\sum_l J_{-l+m}(A)J_l(B) e^{il\phi} = \frac{A+Be^{i\phi}}{A+Be^{-i\phi}}J_m[(A^2 + B^2 + 2AB\cos\phi)^{1/2}]$ , we can simplify this

to

$$\begin{aligned}
F(\eta, \epsilon = \beta = 0) &= \left| \frac{N\phi_d(1 + e^{-i\Delta})}{N\phi_d(1 + e^{i\Delta})} J_0[N\phi_d(2 - 2\cos\Delta)^{1/2}] \right|^2 \\
&= J_0^2(N\phi_d\Delta) \\
&= J_0^2\left(\frac{4\pi}{3}N^3\phi_d\eta\right)
\end{aligned} \tag{4.14}$$

keeping the lowest terms in  $\eta$ . Thus the width of a fidelity peak centered at the resonant zero acceleration should drop as  $1/N^3$ .

A similar procedure gives the fidelity near the resonant( $\beta = 0$ ) initial momentum [90],

$$F(\beta, \epsilon = \eta = 0) = J_0^2(2\pi\phi_d N(N+1)\beta) \tag{4.15}$$

## 4.2 Experimental Configuration and Results

These experiments were performed with a Bose-Einstein condensate of around 20,000  $^{87}\text{Rb}$  atoms in the  $5S_{1/2}, F = 1, m_F = 0$  level. The selection of the  $m_F = 0$  Zeeman sublevel was done by keeping the MOT coils on during the evaporative cooling. Only the  $m_F = 0$  atoms which are insensitive to the magnetic field gradient (10G/cm) of the MOT coils could then undergo a stable evaporation [94], producing a pure  $m_F = 0$  condensate.

After being released from the trap, the condensate was exposed to a horizontal optical grating created by two beams of wavelength  $\lambda = 780$  nm light detuned 6.8 GHz to the red of the atomic transition. The wave vector of each beam was aligned  $\theta = 52^\circ$  to the vertical. This formed a horizontal standing wave at the point of intersection with a wavelength of  $\lambda_G = \lambda/2\sin\theta$ . With this grating vector  $G = 2\pi/\lambda_G$  the resonant Talbot time is  $T_T = 4\pi M/\hbar G^2 = 106.5 \mu\text{s}$ . The kicking pulse length was  $\Delta t = 0.8 \mu\text{s}$  with a measured  $\phi_d \approx 0.6$ . To create the reversal operator  $\hat{U}_r$  in Eq. (4.3), a final kick of strength  $N\phi_d$  was applied at the end of the  $N$  rotor kicks. We did this by increasing the intensity rather than the pulse length in order to keep this

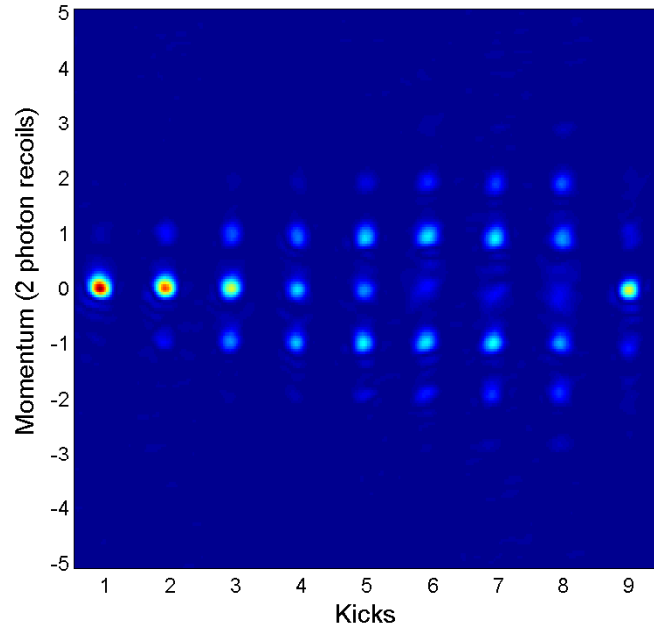


Figure 4.1: Momentum distributions of a sequence of 8 kicks of strength  $\phi_d$  followed by a final  $\pi$ -phase reversed kick of strength  $N\phi_d$ , with a time period equal to the Talbot time  $106.5\mu s$ .

final kick within the Raman-Nath regime. Moreover, the standing wave for this kick was shifted by half a wavelength by changing the phase of one of the kicking AOM's rf driving signal. A time-of-flight image of a fidelity kicking sequence on resonance is depicted in Fig. 4.1.

The sensitivity of the phases in this experiment to external perturbations made it necessary to identify and minimize such sources. Calculating the photon scattering rate  $\gamma_p = \frac{\Omega^2}{\delta^2}\gamma$  for our kicking strength  $\phi_d (= \frac{\Omega^2 \Delta t}{8\delta})$ , we find that decoherence due to spontaneous emission is expected to be important only beyond  $\sim 35$  kicks. Dephasing primarily due to vibrations made the reversal process inconsistent for  $N > 6$ . To reduce this, the standing wave at each kick was shifted by half a wavelength with respect to the previous kick. This had the effect of shifting the Talbot time resonance to  $T_{1/2}$ . Consequently the reduced experimental time led to much improved results. After 8 ms of expansion, the separated momentum orders were absorption imaged.

In the experiment fidelity is measured by the fraction of atoms which have returned to the initial zero momentum state. That is we measure  $F = P_0 / \sum_n P_n$  where  $P_n$  is the number of atoms in the  $n^{\text{th}}$  momentum order obtained from the time-of-flight images. To facilitate the analysis of the data, all of the resonance widths ( $\delta\epsilon$ ) were scaled to that at a reference kick number of  $N = 4$ . That is we define a scaled fidelity width  $\Delta\epsilon = \delta\epsilon / \delta\epsilon_{N=4}$  for each scaled kick number  $N_s = N/4$  and recover  $\log \Delta\epsilon = -3 \log N_s$  using Eq. (4.6). For each kick, a scan is performed around the resonance time. To ensure the best possible fit of the central peak of the fidelity spectrum to a gaussian, the time is scanned between values which make the argument of  $J_0^2$  of Eq. (4.6)  $\approx 2.4$  so that the first side lobes are only just beginning to appear. Figure 4.3(a) plots the logarithm of the FWHM for 4 to 9 kicks scaled to the fourth kick. A linear fit to the data gives a slope of  $-2.73 \pm 0.19$  giving a reasonable agreement with the predicted value of -3 within the experimental error [93]. As seen in the same figure, the results are close to the numerical simulations which take into account the



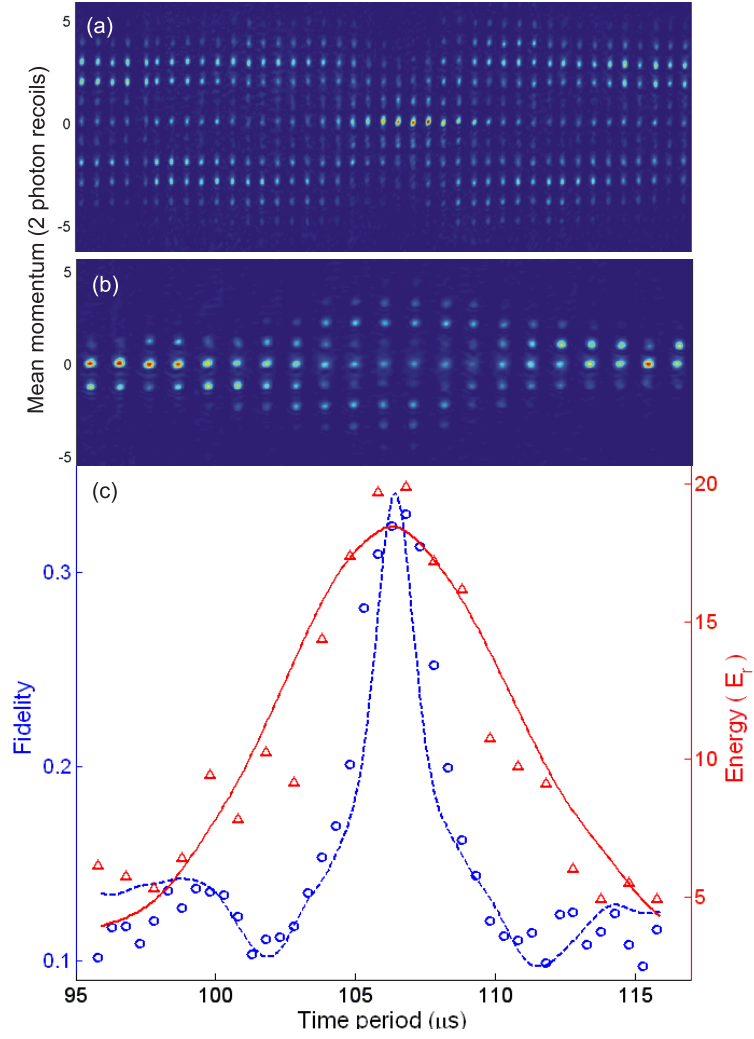


Figure 4.2: (a) Horizontally stacked time-of-flight images of a fidelity scan around the Talbot time. Each TOF image was the result of 5 kicks with  $\phi_d = 0.8$  followed by a  $\pi$ -phase shifted kick at  $5\phi_d$ . (b) Mean energy distribution of the 5 kick rotor with the same  $\phi_d$ . (c) The measured fidelity distribution (circles) from (a). The mean energy of the scan in (b) is shown by the triangles. Numerical simulations of the experiment for a condensate with momentum width  $0.06 \hbar G$  are also plotted for fidelity (blue-dashed line) and mean energy (red-solid line). The amplitude and offset of the simulated fidelity were adjusted to account for the experimentally imperfect reversal phase.

finite width of the initial state of  $0.06 \hbar G$  [27].

We also compared the resonance widths of the kicked-rotor mean energy  $\langle E \rangle$  to that of the fidelity widths. As in the fidelity, the plotted values  $\Delta\langle E \rangle$  have been normalized to that of the fourth kick. On the log scale, the width of each peak gets narrower with the kick number with a slope of  $-1.93 \pm 0.21$  (Fig. 4.3(a)) in agreement with previous results [92, 95]. The relative scalings of the fidelity and mean energy distributions can be seen clearly in Fig. 4.2. It can be seen that even for relatively few kicks the fidelity peak can be significantly narrower. As a further test of Eq. (4.6), the variation in the widths of the fidelity and mean energy peaks were studied as a function of  $\phi_d$ . Figure 4.3(b) shows the fidelity width changing with a slope of  $-1.96 \pm 0.30$ , close to the predicted value of -2. This is again a faster scaling compared to the mean energy width which decreases with a slope of  $-0.88 \pm 0.24$  (the theoretical value being -1).

The resonances studied here appear for pulses separated by the Talbot time and an initial momentum state of  $\beta = 0$ . As seen in Eq. (4.15), the peak width in  $\beta$  space is expected to change as  $1/[N(N+1)]$  around this resonant, as against a  $1/N$  scaling of the mean energy width [92]. To verify this, the initial momentum of the condensate with respect to the standing wave was varied and the kicking sequence applied. The experimentally measured widths  $\Delta\beta = \delta\beta/\delta\beta_{N=4}$  in Fig. 4.4 display a scaling of  $\Delta\beta \propto [N(N+1)]^{-0.92}$  close to the theoretical value.

For an initial state  $|\beta+n\rangle$ , the wave function acquires a non-zero phase during the free evolution even at the Talbot time. Therefore the final kick performs a velocity selective reversal, preferentially bringing back atoms closer to an initial momentum of  $\beta = 0$ . This is similar to the time-reversed Loschmidt cooling process proposed in Refs. [96, 97], although in that technique a forward and reverse path situated on either side of the resonant time was used in order to benefit from the chaotic dynamics. To observe this effect the current scheme offers experimental advantage in terms of

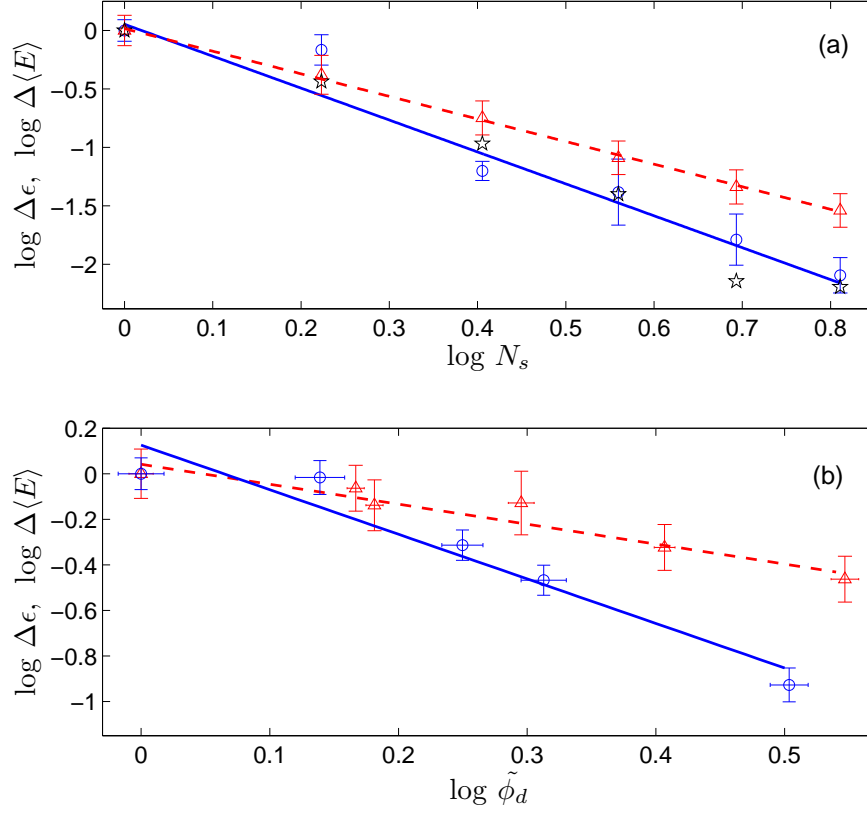


Figure 4.3: Experimentally measured fidelity (circles) and mean energy (triangles) widths (FWHM) as a function of (a) the number of pulses, and (b) the kicking strength  $\tilde{\phi}_d$  scaled to  $\phi_d$  of the first data point. In (a), the data are for 4 to 9 kicks in units normalized to the 4<sup>th</sup> kick. Error bars in (a) are over three sets of experiments and in (b)  $1\sigma$  of a Gaussian fit to the distributions. Dashed lines are linear fits to the data. Stars are numerical simulations for an initial state with a momentum width of  $0.06\hbar G$ .

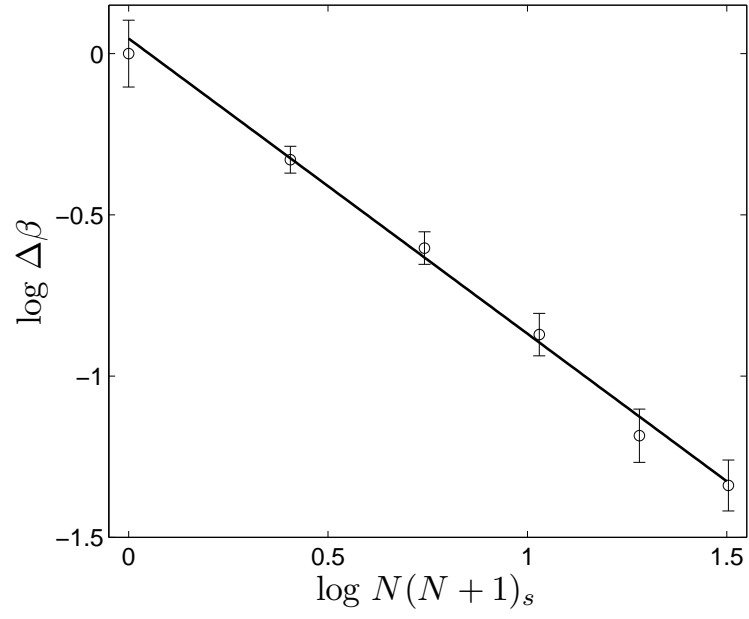


Figure 4.4: Variation of the fidelity peak width around  $\beta=0$  as a function of kick number  $N(N+1)_s = N(N+1)/20$  scaled to the 4<sup>th</sup> kick. The straight line is a linear fit to the data with a slope of  $-0.92 \pm 0.06$ . Error bars as in Fig. 2(b).

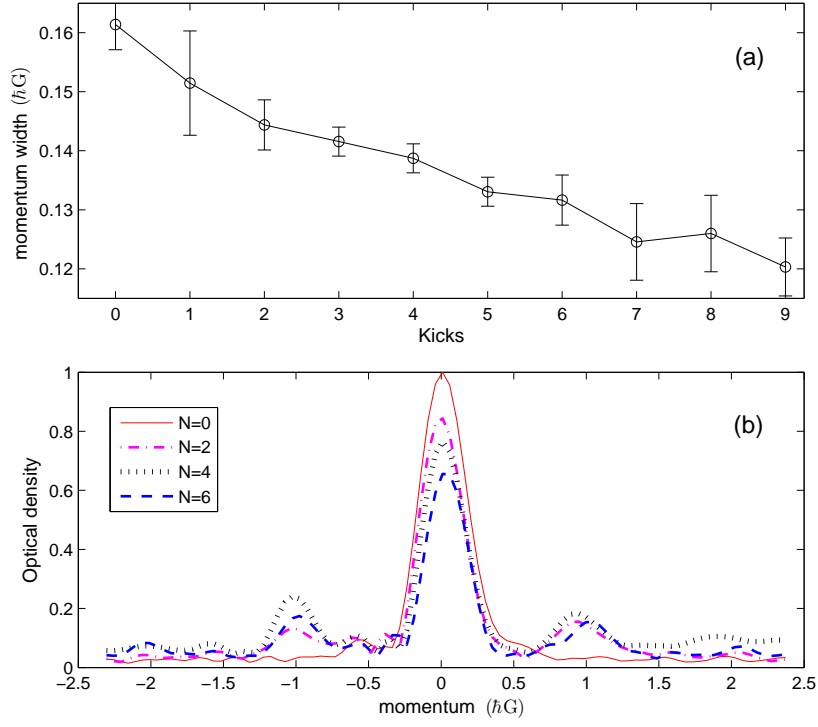


Figure 4.5: (a) Momentum width of the reversed zeroth order state as a function of kick number. Error bars are an average over three experiments. (b) Optical density plots for the initial state (red,solid) and kick numbers 2 (magenta,dot-dashed),4 (black,dotted), and 6 (blue,dashed) after summation of the time-of-flight image along the axis perpendicular to the standing wave.

stability due to the reduced length of the pulse sequence. Here, only a single pulse performs the velocity selection at the end, whereas in the Loschmidt technique  $N$  phase reversed kicks separated by a finite time are used. Figure 4.5 demonstrates the reduction of the momentum distribution width. Accompanying this decrease is a drop in the peak height. Our simulations and the results of Ref. [97] predict that for the case of a non-interacting condensate this should remain constant. In addition to interactions we expect experimental imperfections in the fidelity sequence to play a role in the smaller peak densities with increasing kick numbers. We performed the same experiment 4.5 ms after the BEC was released from the trap when the mean field energy had mostly been transformed to kinetic energy in the expanding condensate. A similar reduction in the momentum width of the reversed state along-with a decrease in the peak density was observed.

Finally to investigate the sensitivity of the fidelity resonance to gravity, the standing wave was accelerated during the application of the pulses. This acceleration was scanned across the resonant zero value and readings of the fidelity collected. Since a typical value of the half-width at half maximum is  $\eta = 0.05$  for  $N=4$  (corresponding to an acceleration of  $4\text{m/s}^2$ ), the perturbative treatment of acceleration on fidelity used above is justified. Figure 4.6 plots the experimental data for 4 to 9 kicks, where the widths of the peaks decrease with a slope of  $-3.00 \pm 0.23$  in excellent agreement with the theory. In conclusion, we performed experimental measurements of the fidelity widths of a  $\delta$ -kicked rotor state near a quantum resonance. The width of these peaks centered at the Talbot time decreased at a rate of  $N^{-2.73}$  comparable to the predicted exponent of  $-3$ . By comparison, the mean energy widths was found to reduce only as  $N^{-1.93}$ . Furthermore, the fidelity peaks in momentum space changed as  $(N(N+1))^{-0.92}$ , also consistent with theory. The reversal process used in the fidelity experiments led to a decrease in the momentum distribution of the final zeroth order state by  $\sim 25\%$  (for  $N=9$ ) from the initial width. The sub-Fourier dependencies of the

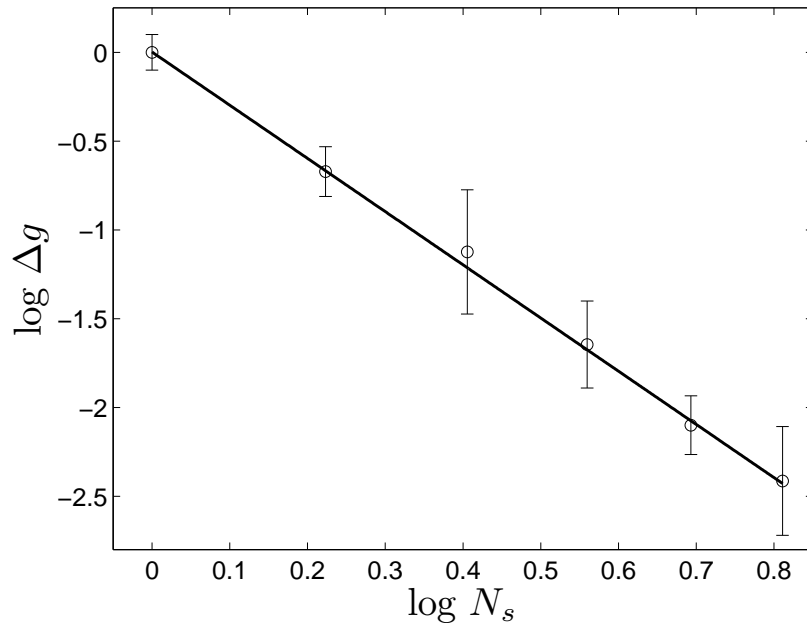


Figure 4.6: Dependence of the acceleration resonance peak width as a function of the kick number in units scaled to the 4<sup>th</sup> kick. Error bars are over three sets of experiments.

mean energy and fidelity observed here are characteristic of the dynamical quantum system that is the QDKR [90]. The narrower resonances of the fidelity scheme could be exploited in locating the resonance frequency with a resolution below the limit imposed by the Fourier relation. This can help determine the photon recoil frequency ( $\omega_r = E_r/\hbar$ ) which together with the photon wavelength enables measurement of the fine structure constant with a high degree of precision [29, 86–88]. We also demonstrated a  $N^{-3}$  dependence of the resonance width in acceleration space in accordance with the extended theory. The sensitivity of an atom interferometer based gravimeter scales as the square of the loop time, hence the pursuit of large area interferometers to improve accuracy [82–84]. By comparison, the fidelity is responsive to the gravitational acceleration  $g$  with the cube of the ‘time’  $N$ , leading to the possibility of higher precision measurements. One could perform a fidelity measurement on a freely falling condensate exposed to kicks accelerating at the local value of  $g$  (to realize  $\eta \ll 1$ ). Variation in  $g$  would then manifest itself as a shift of the resonant acceleration. A parts per billion precision [85] would require a judicious selection of the parameters  $(N, \phi_d, T)$ , for instance  $(150, 10, 16T_{1/2})$ . Such a resolution, though not feasible in the current set-up without addressing stability related issues, could be possible with future refinements, for instance through active stabilization measures.



## CHAPTER 5

### Photoassociation of a $^{87}\text{Rb}$ BEC

Our studies on kicked atoms have so far employed the linear kicked rotor model. A non-linearity can be introduced via interactions among the condensate atoms. Such interaction-induced non-linearity in the kicked rotor was shown to lead to a shift in the resonance and a striking cutoff at the maximum, due to coupling between phonon modes [98]. Another system studied in this context is the quantum  $\delta$ -kicked harmonic oscillator. It is realized with a kicked rotor in a harmonic trap and exhibits resonances like the rotor. Dephasing and destruction of the resonant motion were found to occur in the presence of interactions [99]. Furthermore, the nonlinear version remains an excellent candidate to study quantum-classical correspondence [100]. To pave the way for such studies, it is necessary to tune the interactions on demand. Magnetic Feshbach resonances, and more recently Optical Feshbach resonances, have enabled such control over the condensate interaction. In this chapter, we describe our experiments on photoassociation spectroscopy performed near long range molecular states of a  $^{87}\text{Rb}$  BEC to realize an Optical Feshbach resonance. In section 5.1 we discuss such spectroscopy. This is followed by a review of the theory ultracold collisions and Feshbach resonances in sections 5.2 and 5.3 respectively. We then discuss the experimental configuration and results in section 5.4, and the conclusion in section 5.5.

## 5.1 Photoassociative spectroscopy

Photoassociation (PA) is a process in which two atoms colliding in the presence of a light field absorb a photon to form a bound, excited molecule. This effect was first observed for the  $\text{H}_2$  molecule and rare gas halide molecules [101,102]. With the advent of laser cooling, photoassociation of samples of cold atoms became a high resolution spectroscopic technique as a result of the very low energy spread of the atoms [103]. It has since been used to precisely measure atomic lifetimes, map ground state collisional wavefunctions, probe long range and ‘pure long range’ molecular states and to produce translationally cold molecules from cold atoms [104–107]. Furthermore, it was discovered that the collisional state scattering length can be altered near a photoassociation resonance [111]. This effect has been termed as an optically induced Feshbach resonance and has interesting implications for the dynamics of Bose-Einstein condensates [112–114]. Experimental results of photoassociation of a  $^{87}\text{Rb}$  Bose-Einstein condensate and the effect on the scattering length will be outlined in this chapter.

Figure 1 depicts a typical photoassociative process. The interaction of the ground-state atoms (S+S) occurs along a Van-der Waals potential  $V_g(R) = -C_6/R^6$  at long ranges. For short internuclear distances the interaction is described by a  $1/R^{12}$  strong electron exchange repulsion. Atoms colliding in the presence of light tuned close to the S-P transition can absorb a photon and form an electronically excited molecule. The interaction between the two atoms in the excited molecule is determined by a resonant dipole-dipole interaction,  $V_e = -C_3/R^3$ , at long ranges. Many of the bound states that are formed have energies close to the threshold and are therefore easier to access via free-bound photoassociation compared to traditional bound-bound spectroscopy [104]. The absorption takes place at an internuclear separation called the Condon point  $R_C$  where the laser photon energy is equal to the difference between the ground the excited state potentials. The stimulated rate of transition from the

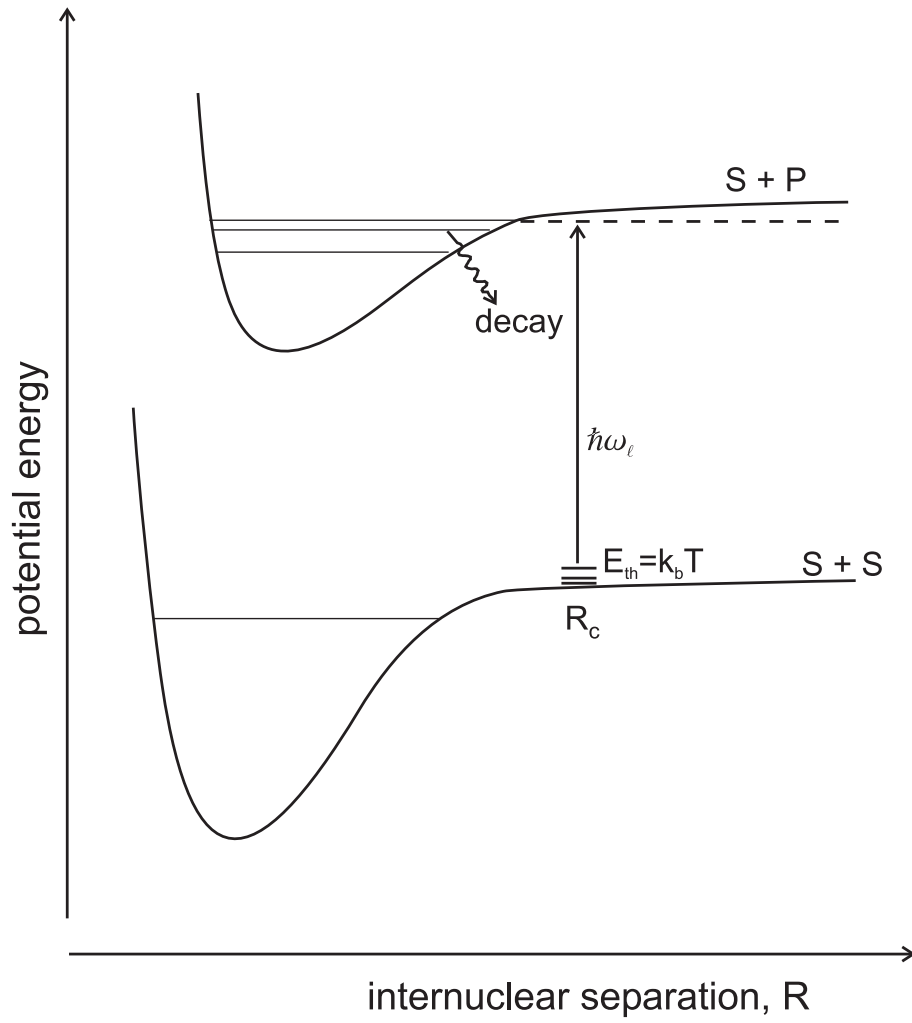


Figure 5.1: Schematic of a photoassociation process. Two atoms colliding along the ground state potential (S+S) absorb a photon and get excited to the (S+P) molecular potential. The excited molecule can subsequently decay to free atoms or a ground state molecule.

free to bound state is given by

$$\Gamma_{\text{stim}} = \frac{4\pi^2 I d_M^2}{c} |\langle e|g\rangle|^2, \quad (5.1)$$

where  $I$  is the laser intensity,  $d_M$  is the molecular dipole transition moment,  $|g\rangle$  is the ground state collisional wavefunction and  $|e\rangle$  the bound, excited state [112]. The decay of the excited state molecule to either ground state molecules or to hot atoms leads to loss from the trap containing the molecules. Monitoring this loss as a function of the PA laser frequency results in a spectrum of the free-bound transitions. This technique is generally known as photoassociation spectroscopy. This is a very high resolution technique resulting from the very low energy spread of ultracold collisions (a few MHz at  $\mu\text{K}$  temperatures, which is comparable to the natural molecular linewidths) [104]. As can be seen from Eqn. (5.1), the transition rate depends on the Franck-Condon overlap between the ground and excited state wavefunctions. With larger collisional wavefunctions at greater internuclear distances, ultracold photoassociation is ideal for probing long-range excited molecular states [104].

The molecular states investigated using photoassociation in this study were the  $1_g$  and the  $0_g^-$  pure long range state. These are labeled by Hund's case (c). The total electron orbital angular momentum  $\vec{l}$  couples strongly with the total spin  $\vec{s}$  to form  $\vec{j} = \vec{l} + \vec{s}$ . The projection of  $\vec{j}$  along the internuclear axis  $\Omega$  is conserved due to cylindrical symmetry of the molecule. The molecular states are labeled as  $\Omega_{g/u}$ . The  $g/u$  denotes the inversion symmetry of the electronic wavefunction. The  $1_g$  state has  $\Omega=1$  and is symmetric with respect to a reflection about the center of the internuclear axis (a *gerade* state,  $g$ ). The  $0_g^-$  state has an additional reflection symmetry and changes sign upon reflection in a plane containing the internuclear axis (the negative sign) [106].

## 5.2 Ultracold Collisions

Elastic two-body collisions are central to the description of Bose-Einstein condensates as they determine the behavior as well as the stability of the condensates. The following discussion reviews basic elastic collision theory. One begins by looking for solutions to the time-independent Schrödinger equation

$$\left[\frac{\hat{p}^2}{2\mu} + V(\mathbf{r})\right]\psi(\mathbf{r}) = E\psi(\mathbf{r}) \quad (5.2)$$

which describes the motion of two atoms with relative momentum  $\mathbf{p} = \hbar\mathbf{k}$  colliding in the potential  $V(\mathbf{r})$ .  $\mu$  is the reduced mass of the particles and  $E = \hbar^2 k^2 / 2\mu$  is the collision energy. At large  $r$ , where the potential is negligible, the scattering wave function satisfies the free-particle Schrödinger equation and the solution can be written as

$$\psi_{\mathbf{k}}(\mathbf{r}) \xrightarrow{r \rightarrow \infty} A[\exp(i\mathbf{k} \cdot \mathbf{r}) + f(k, \theta, \phi) \frac{\exp(ikr)}{r}] \quad (5.3)$$

That is, the scattering wave function at large distances is a superposition of an incident plane wave and an outgoing spherical wave.  $A$  is a normalization constant.

To calculate the scattering amplitude  $f$ , we consider the case of a central potential  $V(r)$ . For such a potential the Hamiltonian commutes with the total angular momentum,  $L^2$  and its projection  $L_z$ . Also the scattering is symmetric about the incident direction and therefore independent of  $\phi$ . One can thus separate the solutions in terms of radial components  $R_l(k, r)$  and Legendre polynomials  $P_l(\cos\theta)$  with contributions of  $l$  different partial waves.

$$\psi_{\mathbf{k}}(k, r, \theta) = \sum_{l=0}^{\infty} R_l(k, r) P_l(\cos\theta) \quad (5.4)$$

The Schrödinger equation for the radial part of the wavefunction becomes

$$\left[\frac{d^2}{dr^2} - \frac{l(l+1)}{r^2} - U(r) + k^2\right]u_l(k, r) = 0 \quad (5.5)$$

where  $u_l(k, r) = rR_l(k, r)$  and  $U(r) = 2\mu V(r)/\hbar^2$ . The total scattering cross section is defined as  $\sigma = \int |f|^2 d\Omega$ , where the integration is over solid angle, can be shown to be

$$\sigma = \frac{4\pi}{k^2} \sum_l (2l+1) \sin^2 \delta_l \quad (5.6)$$

where  $\delta_l$  is the phase shift of the  $l^{\text{th}}$  partial wave as a result of the collision. For identical bosons, only even partial waves contribute,

$$\sigma = \frac{8\pi}{k^2} \sum_{l \text{ even}} (2l+1) \sin^2 \delta_l \quad (5.7)$$

In the ultracold regime the collisional energy is too small to overcome the centrifugal barrier  $\hbar^2 l(l+1)/2\mu r^2$ . As can be seen from Fig. 5.2, any partial wave with  $l > 0$  cannot enter inside the potential. Therefore only  $l=0$  (i.e. s-waves) need to be considered for ultracold collisions.

From Eq. 5.7 the scattering cross-section for the  $l=0$  wave is

$$\sigma_{l=0} \rightarrow 8\pi a^2 \quad (5.8)$$

where the scattering length  $a$  has been defined as

$$a = -\lim_{k \rightarrow 0} \frac{\tan \delta_0}{k} \quad (5.9)$$

Physically, the scattering length can be understood as the intercept of the unperturbed collisional wave-function with the internuclear axis.

### 5.3 Scattering length and Feshbach Resonances

The dynamics of an interacting Bose-Einstein condensate are described by the Gross-Pitaevskii equation

$$\left[ -\frac{\hbar^2}{2m} \nabla^2 + U(\mathbf{r}) + g|\psi(\mathbf{r})|^2 \right] \psi(\mathbf{r}) = -i\hbar \frac{\partial}{\partial t} \psi(\mathbf{r}) \quad (5.10)$$

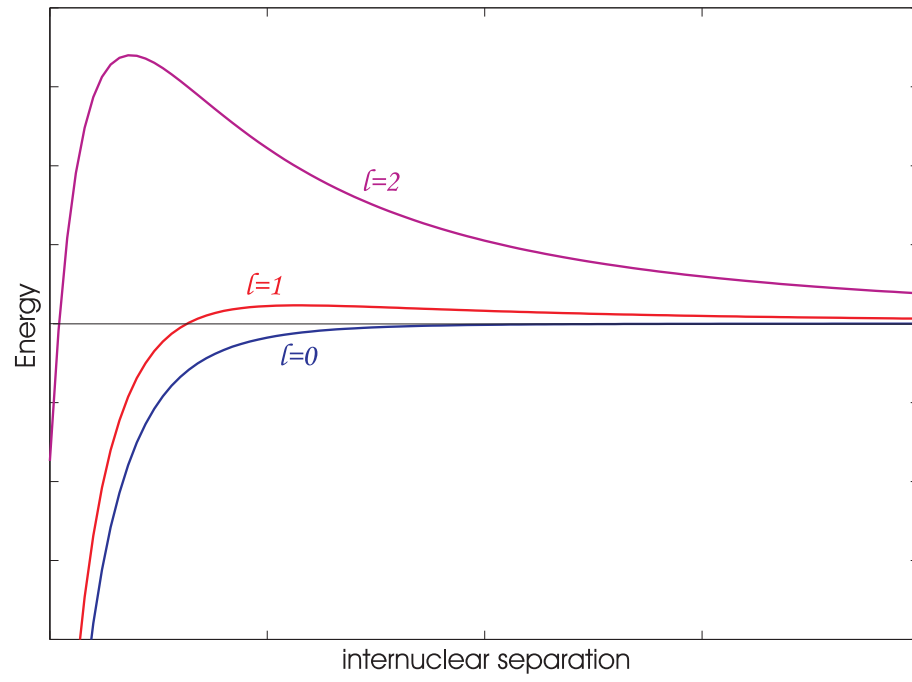


Figure 5.2: Centrifugal energy term  $\hbar^2 l(l+1)/2\mu r^2$  of the Hamiltonian for three partial waves,  $l=0,1,2$ . For low energy scattering all partial waves  $l > 0$  are blocked by the centrifugal barrier.

$\psi(\mathbf{r})$  is the condensate wave function. The first two terms in the Hamiltonian are the kinetic energy and the trapping potential  $U(\mathbf{r})$ . It also contains a non-linear mean field energy term  $g|\psi(\mathbf{r})|^2$  which describes the interaction energy of an atom in the mean-field produced by the other bosons. It is proportional to the condensate density  $n = |\psi(\mathbf{r})|^2$  and the interaction coefficient  $g = 4\pi\hbar^2 a/m$  for two-body elastic collisions between the bosons. The elastic scattering length,  $a$ , thus determines the interactions. For  $a > 0$  the interactions are repulsive, and  $a < 0$  leads to a condensate with attractive interactions stable only below a certain critical density [108]. Changing the scattering length has therefore received much attention and has been made possible by the use of Feshbach resonances.

The scattering length depends strongly on the nature of the interatomic potential. This is best illustrated by the textbook problem of scattering by a square-well potential:

$$\begin{aligned} V(r) &= -V_0 \text{ if } r < R \\ &= 0 \text{ if } r > R \end{aligned}$$

Upon solving the radial wavefunctions  $u_l(r)$  with boundary conditions  $u_l(0) = 0$  and continuity at  $r = R$  one finds the phase shift for the s-wave ( $l=0$ ) to be

$$\delta_0(k) = -kR + \tan^{-1}\left[\frac{k}{k'} \tan(k'R)\right]$$

$k$  and  $k'$  are the wavevectors outside and inside the well respectively. Thus from Eq. 5.9 the scattering length can be shown to be

$$a = R\left[1 - \frac{\tan(\lambda R)}{\lambda R}\right] \quad (5.11)$$

where  $\lambda = \sqrt{mV_0/\hbar^2}$ . Figure 5.3 plots the scattering length as a function of  $\lambda$ . As can be seen, increasing  $\lambda$  which is equivalent to increasing the well depth  $V_0$  leads to periodic divergences of  $a$ .



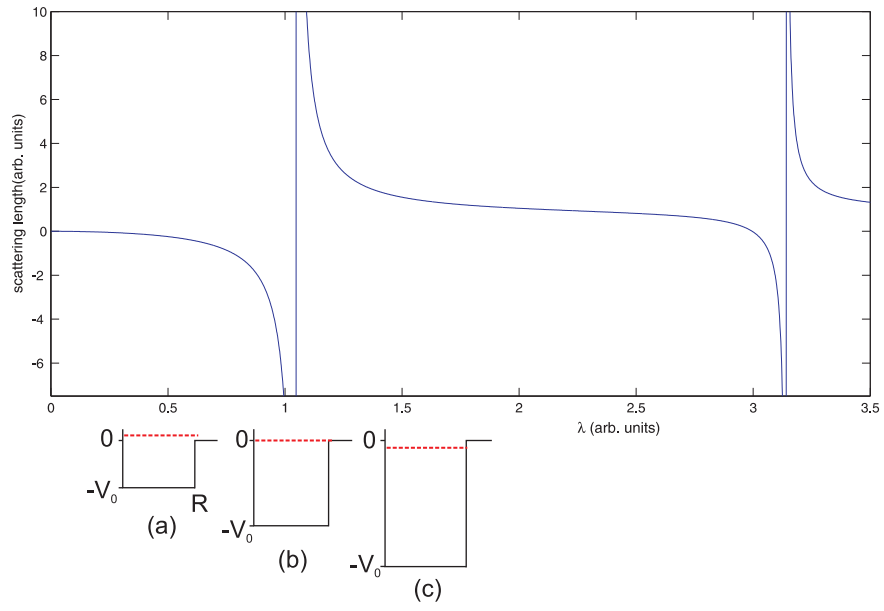


Figure 5.3: Variation of the scattering length  $a$  as a function of  $\lambda = \sqrt{mV_0/\hbar^2}$ . As the well depth  $V_0$  increases ((a) to (c)) a bound state is formed (dashed line) and the scattering length passes through a divergence and changes sign.

The negative scattering length for an attractive square-well potential begins to decrease as the well-depth increases, diverges when the well can hold a bound-state and becomes positive for a weakly bound state. The dependence of the energy of the last bound state,  $E_b$ , on the scattering length is given by  $E_b = -\hbar^2/ma^2$  for  $a \gg R$ .

The relationship between the scattering length and the position of the last bound state is at the heart of the concept of Feshbach resonances. The idea of inducing such a resonance involves using an external field to change the internal states of the colliding atoms to couple them to a quasi-bound state of *another* interatomic potential. Using a magnetic field for instance, two atoms colliding in an open channel  $V_0$  in a hyperfine asymptote can be Zeeman shifted into resonance with a bound state in another hyperfine state where they can stay temporarily bind. The upper potential with a higher threshold energy for the low energy atoms is usually called a closed channel, since energy conservation prohibits the escape of atoms from this potential. The tunability of the scattering length by a magnetic field is expressed as  $a(B) = a_{bg}[1 - \Delta/(B - B_0)]$  where  $a_{bg}$  is the background scattering length far away from resonance,  $B_0$  is the field on resonance, and  $\Delta$  is the width of the resonance. Such a magnetic Feshbach resonance [109] was first observed in a  $^{23}\text{Na}$  BEC [110].

### 5.3.1 Optical Feshbach Resonance

Fedichev et al. [111] proposed the use of optical fields near a photoassociation resonance as a means of modifying the scattering length. An intense field of light tuned near such a resonance can be used to couple a pair of atoms colliding in a ground state potential to a bound excited state of a  $1/R^3$  potential and thereby change the scattering properties of the pair of atoms. Bohn and Julienne [112] introduced a complex phase shift  $\delta = \lambda + i\mu$ , to include the presence of inelastic loss near a PA resonance. This leads to a complex scattering length, the imaginary part of which accounts for the spontaneous loss processes from the excited state. The expressions

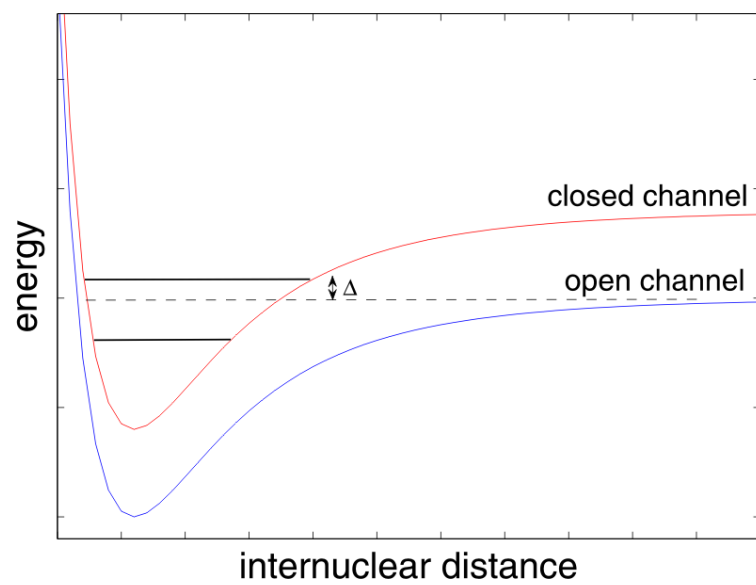


Figure 5.4: A Feshbach resonance occurs when an excited state has a bound state close to the collisional threshold. Changing the detuning  $\Delta$  by an external field can couple the collisional to the bound state and change the scattering length.

for the scattering length,  $a$  and the inelastic loss rate coefficient,  $K_{\text{inel}}$  were given as

$$a = a_{\text{bg}} + \frac{1}{2k_i} \frac{\Gamma_{\text{stim}} \Delta}{\Delta^2 + (\Gamma_{\text{spon}}/2)^2} \quad (5.12)$$

$$K_{\text{inel}} = \frac{2\pi\hbar}{m} \frac{1}{k_i} \frac{\Gamma_{\text{stim}} \Gamma_{\text{spon}}}{\Delta^2 + (\Gamma_{\text{spon}}/2)^2} \quad (5.13)$$

where  $a_{\text{bg}}$  is the background scattering length in the absence of the light,  $k_i$  is the wavenumber of the condensate atoms,  $\Delta$  is the detuning from a PA resonance and  $\Gamma_{\text{stim}}$  and  $\Gamma_{\text{spon}}$  are the stimulated transition rate and spontaneous decay rate constants respectively. In arriving at these expressions the assumption  $\Gamma_{\text{spon}} \gg \Gamma_{\text{stim}}$  has been made [114]. This is usually true with the measured  $\Gamma_{\text{stim}}/2\pi$  being of the order of a few kHz whereas  $\Gamma_{\text{spon}}/2\pi$  is around 20 MHz. From Eq. 5.12 it can be seen that there are two parameters that can tune the scattering length, the detuning  $\Delta$ , and the intensity  $I$ , contained in the stimulated transition rate  $\Gamma_{\text{stim}}$  (Eq. 5.1). To minimise inelastic loss processes and still have a significant change in the scattering length, it becomes necessary to choose a light source far detuned from a PA resonance (Eq. 5.13) and with a high intensity (large  $\Gamma_{\text{stim}}$ , Eq. 5.12). Such an optically induced Feshbach resonance was first achieved in a  $^{87}\text{Rb}$  BEC in 2004 [114].

Another way of viewing the Optical Feshbach Resonance process is in the dressed-state picture. The relevant states are the collisional ground state dressed in  $n$  photons from the laser  $|g, n\rangle$  and the excited state dressed in  $n - 1$  photons  $|e, n - 1\rangle$ . Altering the frequency of the light enables one to change the position of the bound state in the excited state relative to the ground state potential.

## 5.4 Experiment and Results

The photoassociation light was derived from a grating stabilized master laser (Topica Photonics DL 100). The output light was monitored with a wavemeter (Coherent Wavemaster, resolution  $\sim 500$  MHz). To set the laser's initial frequency to a value

near a known molecular level, its grating angle, current, and temperature were appropriately adjusted. It was then offset-locked to the MOT laser using a scanning Fabry-Perot interferometer cavity (Coherent, 300 MHz free spectral range). The majority of the light was used to injection lock a home built diode laser (Sanyo diode, 120 mW). The output of this slave laser was coupled through an optical fiber to the table for the BEC experiment. A small amount of the slave light was sent into the scanning cavity through a flipper mirror (Fig. 5.5). At the right current, transmission peaks of the slave and master overlap on the photodiode signal, indicating that the slave was following the master. The flipper mirror was then lowered and the path kept open for the reference beam to be input into the cavity.

The master PA laser was locked to the reference light using home built electronics. The basic operating principle for the locking is shown in Fig. 5.6. Around 1 mW each from the master PA laser and reference light (from MOT or Repump laser) were coupled to the scanning cavity through a polarizing beam-splitter cube. The cavity was scanned with a free spectral range of 300 MHz with the help of a piezo-electric transducer attached to one of the mirrors. The frequency difference (modulo FSR) between the transmission peaks of the beams from the photodiode was converted to a ‘separation’ voltage,  $V_{\text{sep}}$  [115,116]. The difference between this and a setpoint voltage  $V_{\text{set}}$  from a National Instruments analog card gave the error signal,  $V_{\text{error}}$  (Fig. 5.6). This error signal was sent to a PID controller, built in-house. The correction output from the PID was combined with the scan control voltage from the DL 100 unit to control the PA master laser’s grating angle. Changing  $V_{\text{set}}$  during a photoassociation experiment enabled control over the frequency of the PA light with an accuracy of around 5 MHz.

The power in the PA beam, before it had entered the BEC chamber, was measured at 33 mW. It had a waist radius of 70  $\mu\text{m}$  on the condensate. Higher intensities, which are especially vital for Optical Feshbach Resonances, are possible by reducing

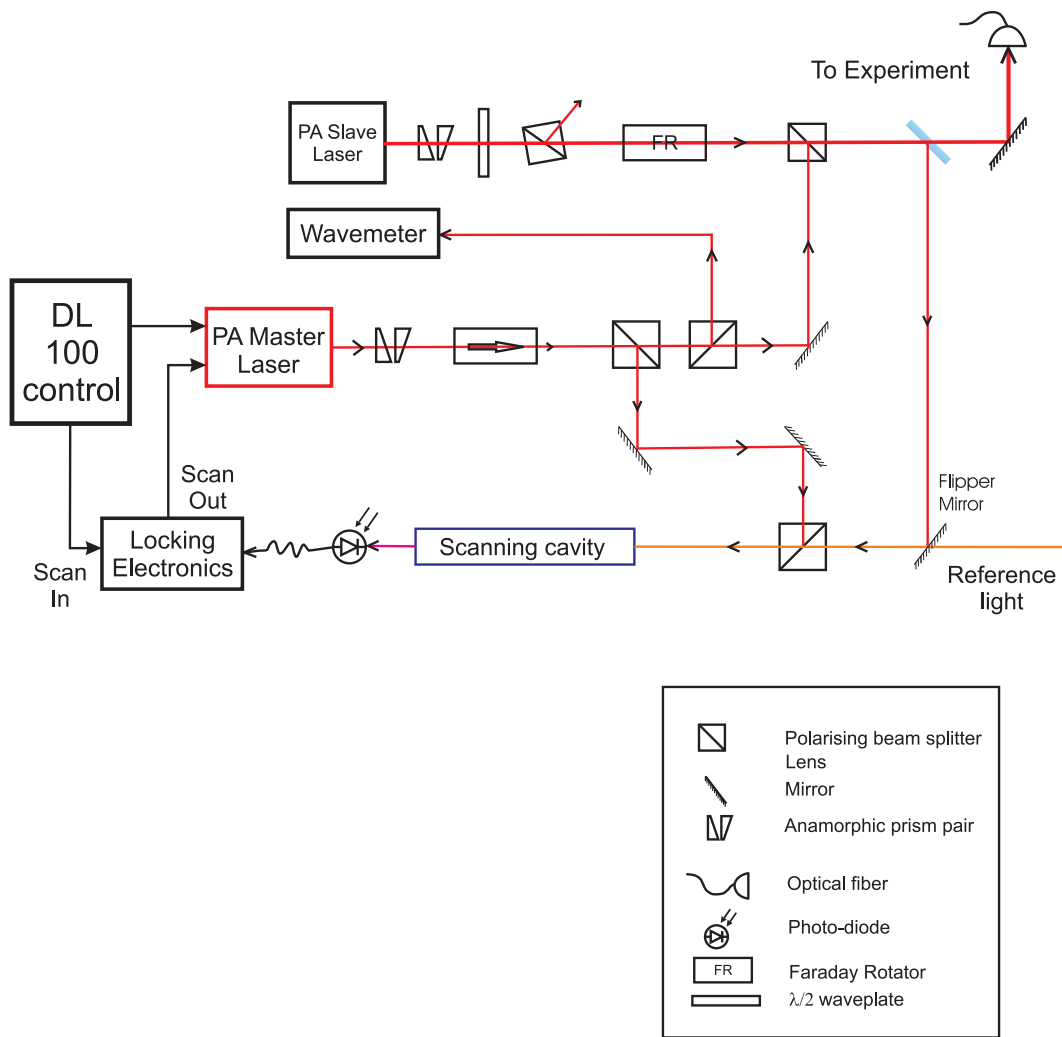


Figure 5.5: Schematic of the optical set-up for the photoassociation light.

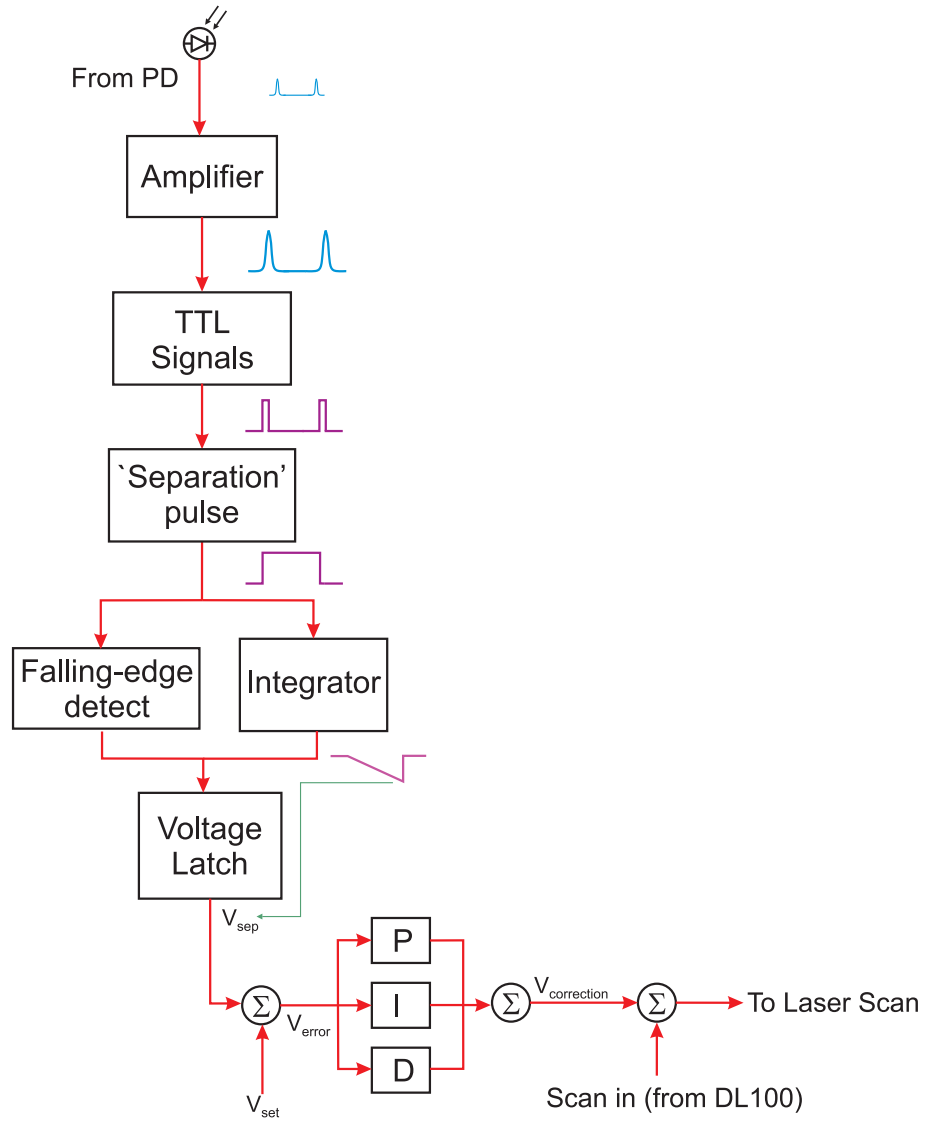


Figure 5.6: Flowchart of the locking for the photoassociation master laser.

the beam waist size. However, this makes the dipole force of the PA beam strong enough to displace the condensate from the FORT making it increasingly difficult to perform any photoassociation experiment.

Figure 5.8 shows the photoassociation spectrum of the  $1_g(P_{3/2}), v = 152$  molecular state. This spectrum was obtained on an ultracold sample (kept in the FORT and just before the BEC transition) with a 1 mW beam pulsed on for 100 ms. The state has a binding energy of  $24.1 \text{ cm}^{-1}$  below the  $^{87}\text{Rb}$   $D_2$  line and asymptotically connects to  $5^2S_{1/2} + 5^2P_{3/2}$  at large internuclear distances [105]. Five molecular lines of the hyperfine structure can be seen. These have been categorized in Ref. [118] according to Hund's rule (c). The good quantum numbers for these states are the total molecular angular momentum  $F$ , total nuclear spin  $I$  and their projections  $F_z$  and  $I_z$  on the internuclear axis.

The  $0_g^-(\sim S_{1/2} + P_{3/2}), v = 1$  photoassociation spectrum of a BEC ( $\sim 25,000$  atoms  $^{87}\text{Rb}$ ) was observed with a 5 ms square pulse with a power of 33 mW. Two rotational lines  $J=0$  and  $J=2$  separated by 200 MHz can be seen in Fig. 5.9. This state located  $26.8 \text{ cm}^{-1}$  below the  $^{87}\text{Rb}$   $D_2$  line is a 'pure long range' state with internuclear distances  $> 20a_0$  [117], much greater than ordinary chemical bonds ( $a_0 = 0.53\text{\AA}$  is the Bohr radius). Single atom spontaneous emission losses in the presence of the PA light is proportional to  $(\Omega/\delta)^2$ , where  $\Omega$  is the Rabi frequency and  $\delta$  the light detuning from an atomic resonance. With the high detuning (800 GHz) of the  $0_g^-$  state from the atomic resonance such losses are therefore small. Moreover, a strong Franck-Condon overlap with the incident collisional state [117] and absence of many neighboring molecular states makes the  $0_g^-(P_{3/2}), v = 1$  particularly suitable for studying Optical Feshbach resonances near it.

Bragg spectroscopy [119] was utilised in Ref. [114] as a technique to measure the scattering length as a function of the photoassociation detuning.  $N$ -th order Bragg diffraction is a process where atoms exposed to a standing wave of off-resonant



light undergo absorption of  $N$  photons from one beam, followed by emission into the other. The internal state of an atom is left unchanged but it ends up acquiring  $2N$  photon recoils of momentum ( $2N\hbar k$ , where  $k = 2\pi/\lambda$  is the wave-vector of light). For a moving standing wave created by two beams with a frequency difference  $\nu$ , the energy and momentum conservation condition for noninteracting atoms is satisfied when  $h\nu_0 = (2\hbar k)^2/2m + 2\hbar \mathbf{k} \cdot \mathbf{p}_i/m$  [119].  $\mathbf{p}_i$  is the initial momentum of the atoms. In a weakly interacting condensate of uniform density  $n$ , the Bogoliubov dispersion relation is

$$\nu = \sqrt{\nu_0^2 + 2\nu_0 nU/h}$$

where  $nU = n4\pi\hbar^2 a/m$  is the chemical potential. For  $h\nu \gg nU$

$$\nu = \nu_0 + nU/h \quad (5.14)$$

The free particle resonance frequency has thus been shifted by the mean field energy [119]. In the presence of a photoassociation light tuned near a molecular state, any optically induced change in the scattering length should therefore be apparent in a shift of the Bragg resonance frequency. Therefore for a known condensate density, such a shift in the resonance frequency would allow measurement of the scattering length  $a$ .

Light 6.8 GHz red detuned from the  $^{87}\text{Rb}$   $D_2$  line was used to create a standing wave. As shown in Fig. 5.7 the Bragg (kicking) beams were aligned such that the wavevector of the standing wave was along the long axis of the FORT. Each of the beams were passed through two acousto-optic modulators. The radio-frequency driving one of these modulators was changed to vary the frequency of the beam passing through it. This created a moving standing wave required to perform a Bragg scan around the resonance frequency. Figure 5.10(a) is an image of a Bragg scan performed by changing the relative frequency between the two beams creating the standing wave. A  $90\ \mu\text{s}$  long Bragg pulse transferred nearly 40% atoms on resonance

to the  $-2\hbar k$  momentum state. Figure 5.10(b) shows the Bragg resonance curves for photoassociation light detunings of  $\Delta/2\pi = +10$  MHz and -10 MHz with respect to the  $0_g^-(P_{3/2}), v = 1, J = 2$  molecular state. No shift of the resonance is observed.

An alternate approach can be adopted to extract the scattering length values from the loss spectrum [114,118]. The two-body loss rate equation for the condensate density  $n(\mathbf{r}, \mathbf{t})$  is

$$\frac{\partial n(\mathbf{r}, \mathbf{t})}{\partial t} = -2K_{\text{inel}}n(\mathbf{r}, \mathbf{t})^2 \quad (5.15)$$

where  $K_{\text{inel}}$  is the inelastic rate coefficient. Assuming local density changes only due to photoassociation loss, McKenzie et. al. [120] give a relationship between the fraction of remaining atoms  $f(\eta)$  and  $K_{\text{inel}}$

$$f(\eta) = \frac{15}{2}\eta^{-5/2}\{\eta^{1/2} + \frac{1}{3}\eta^{3/2} - (1 + \eta)^{1/2} \tanh^{-1}[\sqrt{\eta/(1 + \eta)}]\} \quad (5.16)$$

where  $\eta = 2K_{\text{inel}}n_0t$  and  $t$  is the PA pulse length.

The  $K_{\text{inel}}$  values calculated from the loss spectrum of the  $0_g^-(P_{3/2}), v = 1, J = 2$  state using Eq. 5.16 is shown in Fig. 5.11. A lorentzian fit to this yields a spontaneous decay rate,  $\Gamma_{\text{spon}}$ , of 8 MHz(Eq. 5.13). In addition, the amplitude  $A_0$  of the fit can be related to the stimulated rate constant  $\Gamma_{\text{stim}}$  as  $\Gamma_{\text{stim}}/k_i = A_0(m\Gamma_{\text{spon}}/8\pi\hbar)$  from Eq.5.13. For the data in Fig. 5.11,  $\Gamma_{\text{stim}}/k_i = 2.3 \times 10^{-3}\text{ms}^{-1}$ .

These values of  $\Gamma_{\text{stim}}$  and  $\Gamma_{\text{spon}}$  can be used in Eq. 5.12 to calculate the scattering length and the result is plotted in Fig. 5.12. A maximum change of  $6a_0$  can be seen. This corresponds to a variation of 5 Hz in the Bragg resonance frequency, quite a small value to be detected using Bragg analysis. To achieve larger variations in the scattering length, a higher intensity of the PA light is necessary as can be seen from Eq. 5.12. Moreover any alteration in  $a$  can be amplified in the mean-field induced Bragg shift by using a higher condensate density (Eq. 5.14). Thus an improvement in these two parameters is crucial for the direct observation of an optically induced Feshbach resonance.

## 5.5 Conclusion and Outlook

Photoassociation spectroscopy performed on a  $^{87}\text{Rb}$  BEC was able to resolve five hyperfine levels of the  $1_g$  long range molecular state and two rotational levels of the  $0_g^-$  ‘pure long range’ state, matching the available data in the literature. Bragg spectroscopy done near the  $0_g^-(P_{3/2}), v = 1, J = 2$  state did not yield a detectable change in the s-wave scattering length  $a$ . Analysis of the loss spectrum of this state as a function of the photoassociation detuning revealed a change of 6 Bohr radius in the scattering length. To achieve a larger and directly observable change, an improvement in the condensate density and the photoassociation light intensity is necessary and is currently being pursued.

Another approach could be to more easily detect small changes in ‘ $a$ ’ using a different measurement technique. Such a possibility was investigated using a method based on the interference between two copies of the condensate, made by standing wave pulses separated by  $\Delta t$  as shown in Fig. 5.13(a) [121]. The final interference amplitude depends on the difference in phase between the two copies accumulated during  $\Delta t$ ,  $\phi = [\frac{\hbar G^2}{2m} + \frac{2\mu}{7\pi\hbar}]\Delta t$  where the first term arises from the recoil energy of the initial copy and the second term is due to a mean field effect of the condensate Fig. 5.13(a). Here it is assumed that one of the condensates has few atoms and consequently negligible mean field energy. The measured signal is then the number of atoms diffracted by the two pulses divided by the maximum number of atoms diffracted (i.e., without the second pulse). It can be seen in Fig. 5.13(c) that the signal oscillates faster for a larger mean field of a condensate with a higher number of atoms. Such a change in the oscillation frequency can be expected to occur in the presence of Optically Induced scattering length changes. Compared to the Bragg technique, this method yields a higher frequency resolution of mean field shifts simply with an increase in the measurement time  $\Delta t$  (Fig. 5.13(d)).

Thalhammer *et al.* recently induced an optical Feshbach resonance via a coherent

Raman transition [122]. This stimulated Raman scheme offers a more stable control of the photoassociation light frequency and has a slightly less severe restriction on the light intensity. It can be achieved in our existing experiment by adding a second laser with a suitable frequency in order to couple the colliding atoms to a bound state in the ground molecular potential.

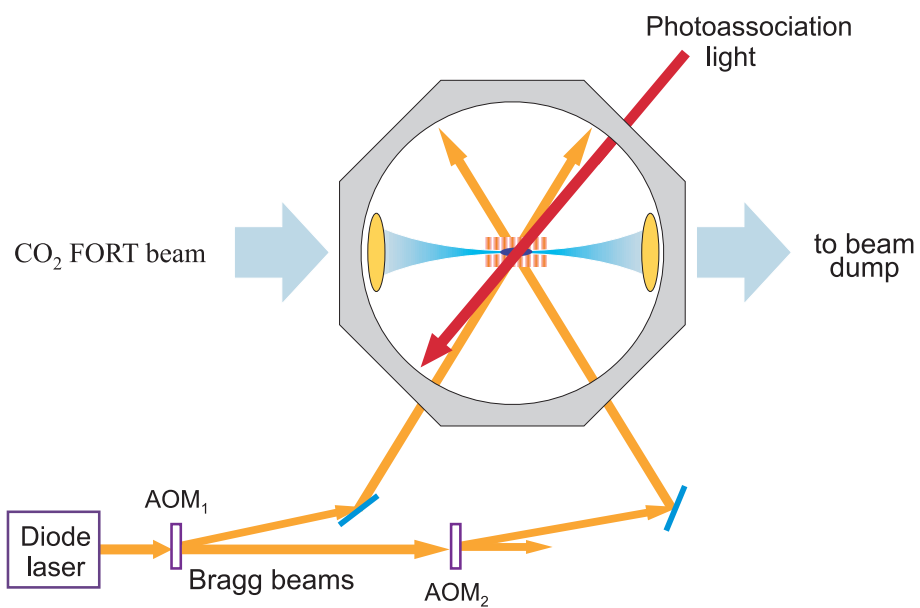


Figure 5.7: Experimental configuration for photoassociation. Shown are the  $\text{CO}_2$  laser FORT and the photoassociation beams. The Bragg (kicking) beams were aligned such that a horizontal standing wave was created along the long axis of the FORT.

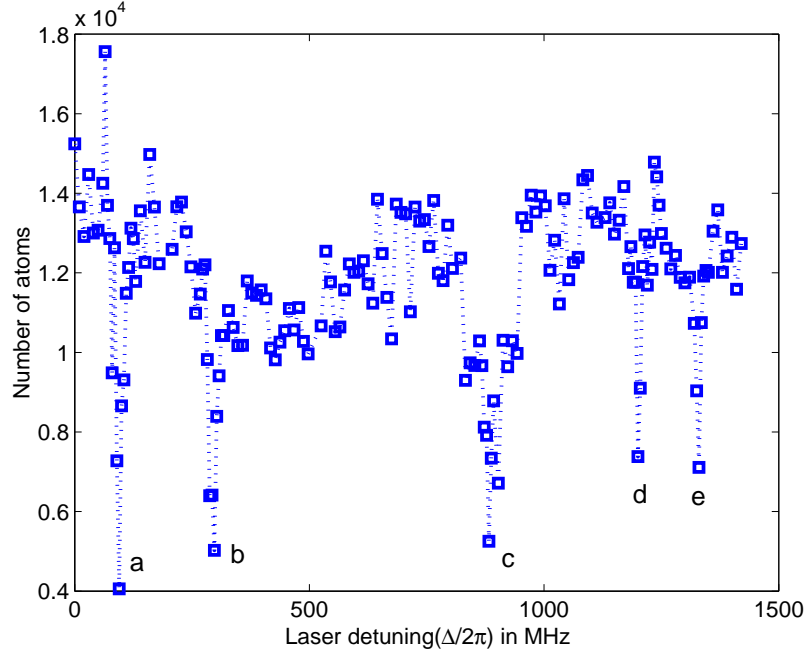


Figure 5.8: Photoassociation spectrum of the  $1_g(P_{3/2}), v = 152$  state. 0 MHz on this scale corresponds to a point 713 GHz below the  $^{87}\text{Rb}$   $D_2$  line. The states  $a$  through  $e$  correspond to  $|2, -2, 3, -3\rangle, |3, -2, 3, -3\rangle, |1, -1, 3, -2\rangle, |2, -1, 3, -2\rangle, |1, 0, 1, -1\rangle$  of Ref. [118] labeled by the  $|F, f, I, i\rangle$  quantum numbers.

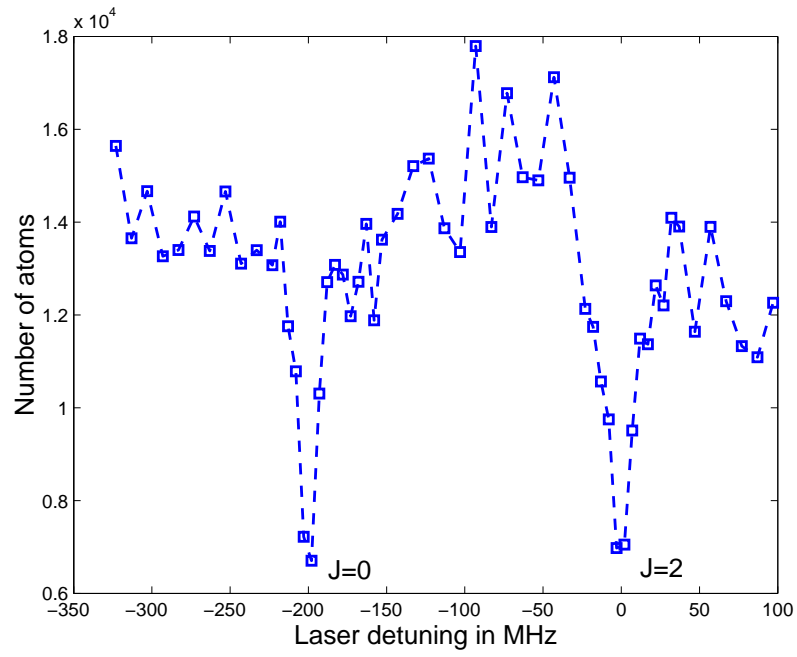


Figure 5.9: Photoassociation of the  $0_g^-(\sim S_{1/2} + P_{3/2}), v = 1$  state showing the J=0 and J=2 rotational levels. Each point is separated by 5 MHz.

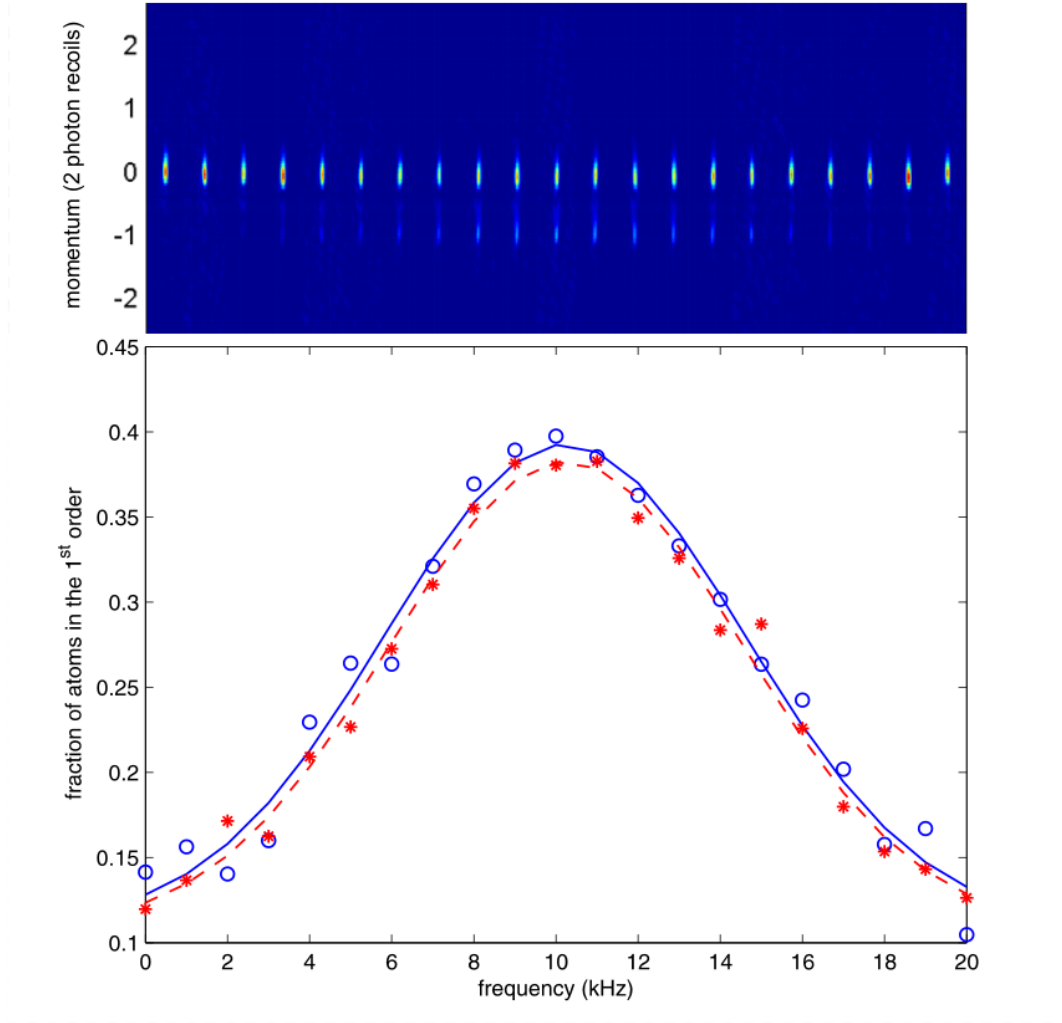


Figure 5.10: (a) First order Bragg diffraction as a function of the frequency difference between the beams used to create the standing wave. (b) Percentage of Bragg diffracted atoms for two photoassociation light detunings,  $\Delta/2\pi = +10\text{MHz}$  (red) and  $-10\text{MHz}$  (blue).



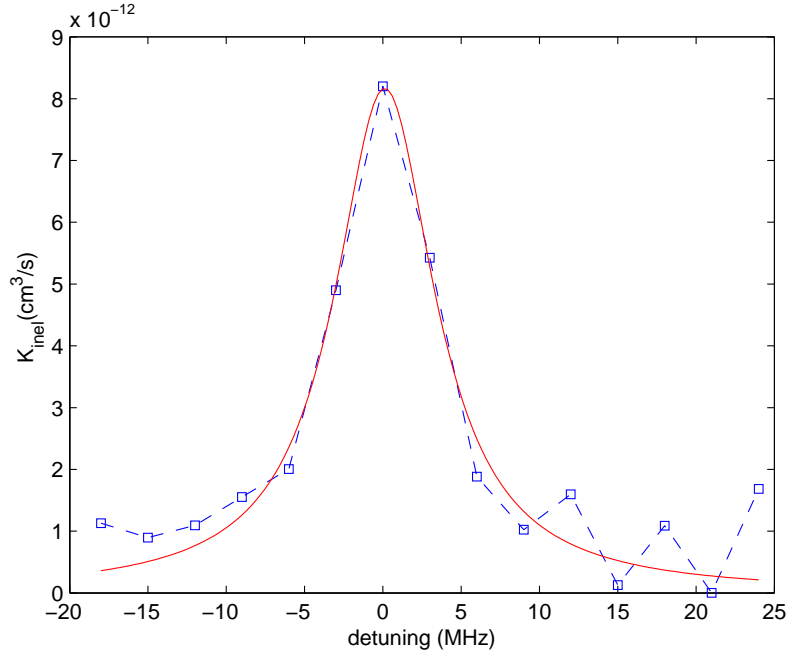


Figure 5.11: Measured inelastic collision rate coefficients for the  $0_g^-(P_{3/2}), v = 1, J = 2$  state. Also shown is a lorentzian fit to the data from which values of  $\Gamma_{\text{spon}}$  and  $\Gamma_{\text{stim}}$  are obtained.

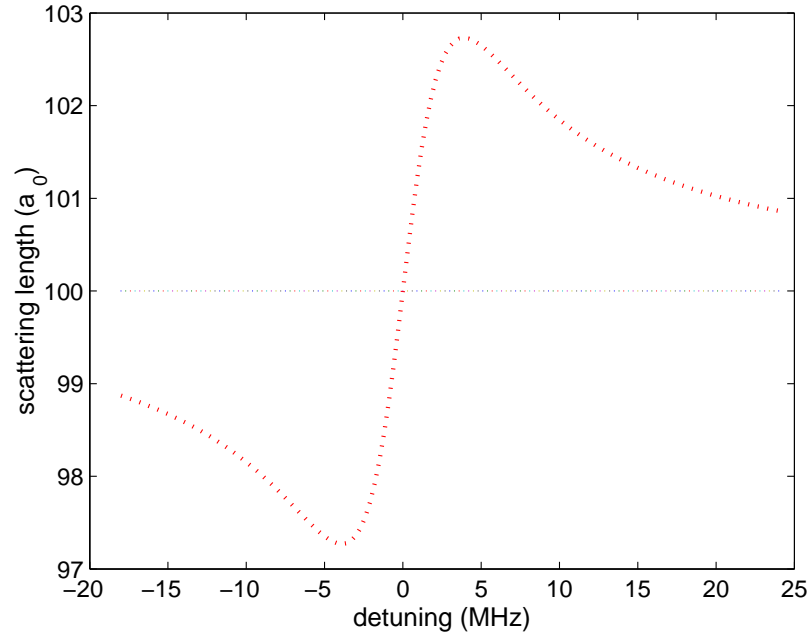


Figure 5.12: Plot of the scattering length  $a$  in units of  $a_0 = 0.53\text{\AA}$ , the Bohr radius, calculated from the data in Fig. 5.11. The dashed line is the background scattering length of  $100a_0$  and the detuning is with respect to the  $0_g^-(P_{3/2}), v = 1, J = 2$  state.

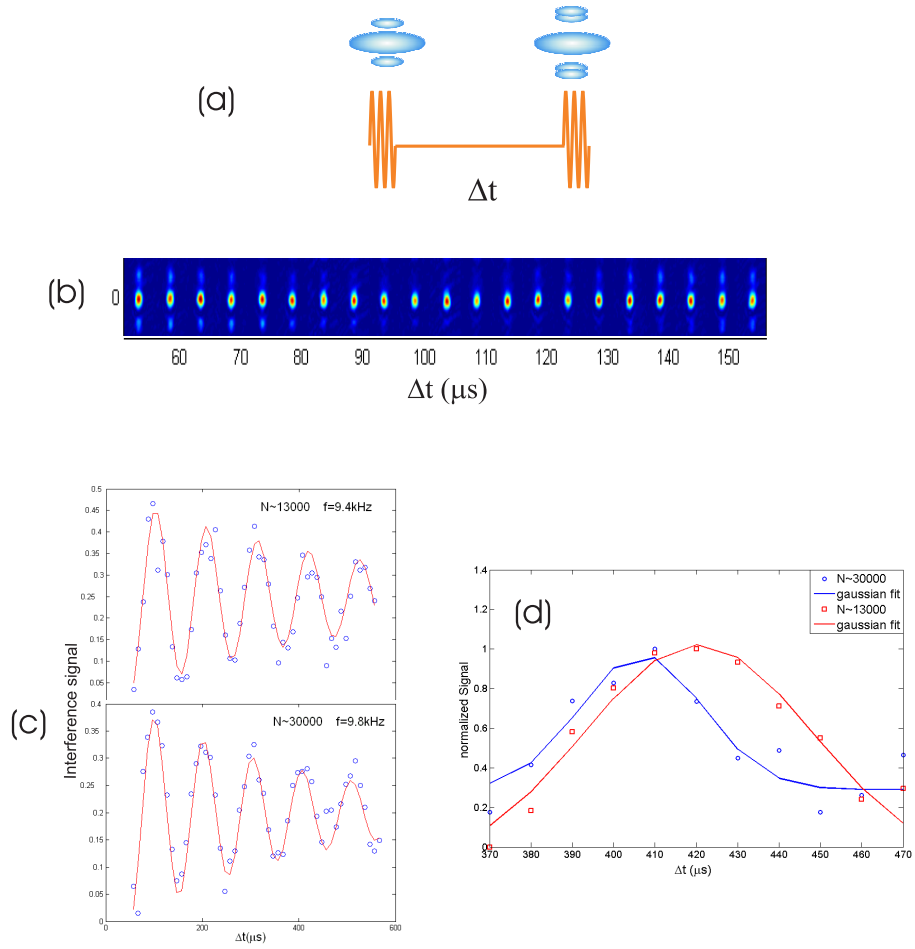


Figure 5.13: Interference between condensates as a measure of mean field energy. Please refer to text for details.

## CHAPTER 6

### CONCLUSIONS

#### 6.0.1 Summary

The work covered in this study explored two features of a periodically kicked quantum system - transport and sensitivity to deviations from resonance. To prepare the required initial momentum state for these experiments, a BEC was created in an all-optical trap. Exposing it to short periodic kicks from an off-resonant standing wave, with the correct choice of parameters, enabled investigation of momentum transport. The first system was a quantum  $\delta$ -kicked accelerator. Specifically three higher order resonances of an accelerator mode were observed and their parameter dependence characterized. Two theoretical approaches were used to analyze the modes - one based on rephasing of momentum states separated by the order of the resonance. It was also seen that the dynamics could be explained as contributions from a family of rays of a fictitious classical system, obtained close to the resonance ( $\epsilon \rightarrow 0$ ).

A quantum ratchet was realized at a primary resonance ( $T_{1/2}$ ). The dependence of the directed ratchet current on the momentum of the initial state, or *quasimomentum*, was investigated and explained by theory. A result of this *quasimomentum* dependence is that the finite momentum width of a BEC was found to suppress the ratchet current after some kicks.

Measurement of the fidelity or overlap of a resonant QDKR state with an off-resonant state was performed. The widths of the resultant peaks were found to scale as the inverse cube of the measurement time, in units of kicks. A theoretical analysis revealed a similar scaling behavior in the presence of acceleration and was validated

by experiment. Furthermore, velocity selection in the measurement process led to a reduced momentum width of the final zeroth order state compared to the initial state.

Finally, photoassociation spectroscopy was performed on a  $^{87}\text{Rb}$  Bose-Einstein condensate for the  $1_g$  and  $0_g^-$  long range molecular states to realize an Optical Feshbach resonance. The observed loss spectrum was used to analyze the change in the elastic scattering length.

### 6.0.2 Future work

The results described in this work lays out the groundwork for further refinements to the experiments and future research. It became clear during the search for Optical Feshbach resonances that extracting the scattering lengths near a photoassociation resonance is more involved than with a Magnetic Feshbach resonance. Bragg spectroscopy as a measure of the scattering length is time consuming, with the photoassociation losses adding to the difficulties. Recently it was shown that the benefits of the two could instead be combined: a robust magnetic Feshbach resonance in the presence of a bound-bound photoassociation light provides the flexibility of the optical method with a minimized atom loss [123]. Some changes to our existing experimental set-up are currently being undertaken to implement this technique. Once tunability of interatomic interactions is achieved, its effect on the resonances of the QDKR and QDKA can be probed.

Complex optical potentials can be produced by overlapping standing waves of on resonant and off resonant light. Presence of a Feshbach resonances in the light will allow a new degree of control and absorptive and refractive indices of atoms diffracted by these potentials can be studied.

Another model popular with quantum chaologists is the  $\delta$ -kicked harmonic oscillator. Its phase space displays a stochastic web, the thickness of which is determined by the amount of underlying classical chaos. Identifying such a web in the quantum

version and exploring its properties can yield answers to questions on quantum chaos. Such a system can be implemented for instance by kicking the condensate while it is still in the trap.

With an improved understanding gained from this research, one can hope to harness more of the exotic quantum properties in real life applications like quantum information processing and computations.

## BIBLIOGRAPHY

- [1] A. Einstein, “Zum Quantensatz von Sommerfeld und Epstein”, Verh. Deutsch. Phys. Ges. **19**, 82 (1917).
- [2] Michael Tabor, *Chaos and Integrability in Nonlinear Dynamics: An Introduction* (Wiley, New York, 1989).
- [3] A. Peres, *Quantum Theory: Concepts and Methods* (Kluwer Academic Publishers, Dordrecht, 1993).
- [4] J. E. Bayfield, and P. M. Koch, “Multiphoton Ionization of Highly Excited Hydrogen Atoms,” Phys. Rev. Lett. **33**, 258 (1974).
- [5] J. E. Bayfield, L. D. Gardner, and P. M. Koch, “Observation of Resonances in the Microwave-Stimulated Multiphoton Excitation and Ionization of Highly Excited Hydrogen Atoms,” Phys. Rev. Lett. **39**, 76 (1977).
- [6] F. L. Moore, J. C. Robinson, C. F. Bharucha, Bala Sundaram, and M. G. Raizen, “Atom optics realization of the quantum delta-kicked rotor,” Phys. Rev. Lett. **75**, 4598 (1995).
- [7] M. G. Raizen, F. L. Moore, J. C. Robinson, C. F. Bharucha, and Bala Sundaram, “An Experimental Realization of the Quantum delta-Kicked Rotor,” Quantum and Semiclass. Optics **8**, 687 (1996).
- [8] E. J. Galvez, B. E. Sauer, L. Moorman, P. M. Koch, and D. Richards, “Microwave Ionization of H Atoms: Breakdown of Classical Dynamics for High Frequencies,” Phys. Rev. Lett. **61**, 2011 (1988).

- [9] J. E. Bayfield, G. Casati, I. Guarneri, and D. W. Sokol, “Localization of Classically Chaotic Diffusion for Hydrogen Atoms in Microwave Fields,” *Phys. Rev. Lett.* **63**, 364 (1989).
- [10] R. Blümel, A. Buchleitner, R. Graham, L. Sirko, U. Smilansky, and H. Walther, “Dynamical localization in the microwave interaction of Rydberg atoms: The influence of noise,” *Phys. Rev. A* **44**, 4521 (1991).
- [11] F. L. Moore, J. C. Robinson, C. F. Bharucha, P. E. Williams, and M. G. Raizen, “Observation of Dynamical Localization in Atomic Momentum Transfer: A New Testing Ground for Quantum Chaos,” *Phys. Rev. Lett.* **73**, 2974 (1994).
- [12] B. G. Klappauf, W. H. Oskay, D. A. Steck, and M. G. Raizen, “Observation of Noise and Dissipation Effects on Dynamical Localization,” *Phys. Rev. Lett.* **81**, 1203 (1998).
- [13] V. Milner, D. A. Steck, W. H. Oskay, and M. G. Raizen, “Recovery of classically chaotic behavior in a noise-driven quantum system,” *Phys. Rev. E* **61**, 7223 (2000).
- [14] A. J. Daley, A. S. Parkins, R. Leonhardt, and S. M. Tan, “Diffusion Resonances in Action Space for an Atom Optics Kicked Rotor with Decoherence,” *Phys Rev. E* **65**, 035201(R) (2002).
- [15] H. Ammann, R. Gray, I. Shvarchuck, N. Christensen, “Quantum delta-kicked rotor: Experimental observation of decoherence,” *Phys. Rev. Lett.* **80**, 4111, (1998).
- [16] R. Feynman, “Simulating Physics with Computers,” *Int. J. Theoret. Phys.* **21**, 467 (1982).



- [17] S. R. Wilkinson, C. F. Bharucha, K. W. Madison, Qian Niu, and M. G. Raizen, “Observation of Atomic Wannier-Stark Ladders in an Accelerating Optical Potential,” *Phys. Rev. Lett.* **76**, 4512 (1996).
- [18] Qian Niu, Xian-Geng Zhao, G. A. Georgakis, and M. G. Raizen, “Atomic Landau-Zener Tunneling and Wannier-Stark Ladders in Optical Potentials,” *Phys. Rev. Lett.* **76**, 4504 (1996).
- [19] S. R. Wilkinson, C. F. Bharucha, M. C. Fischer, K. W. Madison, P. R. Morrow, Qian Niu, Bala Sundaram, and M. G. Raizen, “Experimental evidence for non-exponential decay in quantum tunnelling,” *Nature* **387**, 575 (1997).
- [20] M. B. Dahan, E. Peik, J. Reichel, Y. Castin, and C. Salomon, “Bloch Oscillations of Atoms in an Optical Potential,” *Phys. Rev. Lett.* **76**, 4508 (1996).
- [21] E. Peik, M. B. Dahan, I. Bouchoule, Y. Castin, and C. Salomon, “Bloch oscillations of atoms, adiabatic rapid passage, and monokinetic atomic beams,” *Phys. Rev. A* **55** 2989 (1997).
- [22] Q. Niu and M. G. Raizen, “How Landau-Zener Tunneling Takes Time,” *Phys. Rev. Lett.* **80**, 3491 (1998).
- [23] M. K. Oberthaler, R. M. Godun, M. B. dArcy, G. S. Summy, and K. Burnett, “Observation of Quantum Accelerator Modes,” *Phys. Rev. Lett.*, **83**, 4447, (1999).
- [24] R. M. Godun, M. B. dArcy, M. K. Oberthaler, G. S. Summy, and K. Burnett, “Quantum accelerator modes: a tool for atom optics,” *Phys. Rev. A* **62**, 013411 (2000).

- [25] M. B. d’Arcy, R. M. Godun, D. Cassettari, and G. S. Summy, “Accelerator-mode-based technique for studying quantum chaos,” *Phys. Rev. A* **67**, 023605 (2003).
- [26] M. Sadgrove, M. Horikoshi, T. Sekimura, and K. Nakagawa, “Rectified Momentum Transport for a Kicked Bose-Einstein Condensate,” *Phys. Rev. Lett.*, **99**, 043002 (2007).
- [27] I. Dana, V. Ramareddy, I. Talukdar, and G. S. Summy, “Experimental Realization of Quantum-Resonance Ratchets at Arbitrary Quasimomenta,” *Phys. Rev. Lett.*, **100**, 024103 (2008).
- [28] P. Szriftgiser, J. Ringot, D. Delande, and J. C. Garreau, “Observation of Sub-Fourier Resonances in a Quantum-Chaotic System,” *Phys. Rev. Lett.* **89**, 224101 (2002).
- [29] A. Tonyushkin and M. Prentiss, “Selective manipulation of degenerate interferometer loops by an atom-optics kicked rotor,” *Phys. Rev. A*, **78** 053625 (2008).
- [30] A. Tonyushkin, S. Wu, and M. Prentiss, “Demonstration of a multipulse interferometer for quantum kicked-rotor studies,” *Phys. Rev. A*, **79**, 051402(R) (2009).
- [31] M. H. Anderson, J. R. Ensher, M. R. Matthews, C. E. Wieman and E. A. Cornell, “Observation of Bose-Einstein Condensation in a Dilute Atomic Vapor,” *Science* **269** 198 (1995).
- [32] K. B. Davis, M. -O. Mewes, M. R. Andrews, N. J. van Druten, D. S. Durfee, D. M. Kurn, and W. Ketterle, “Bose-Einstein Condensation in a gas of Sodium atoms,” *Phys. Rev. Lett.* **75**, 3969 (1995).

- [33] M. D. Barrett, J. A. Sauer, and M. S. Chapman, “All-optical formation of an atomic Bose-Einstein condensate,” *Phys. Rev. Lett.* **87**, 010404 (2001).
- [34] BV Chirikov, “A universal instability of many-dimensional oscillator systems,” *Phys Rep* **52(5)**, 265-379, (1979).
- [35] A. L. Lichtenberg, and M. A. Lieberman, *Regular and Chaotic Dynamics* (Springer-Verlag, 1991).
- [36] J. M. Greene, “A method for determining a stochastic transition,” *J. Math. Phys.* **20**, 1183, (1979).
- [37] F. L. Moore, J. C. Robinson, C. Bharucha, P. E. Williams, and M. G. Raizen, “Observation of dynamical localization in atomic momentum transfer: A new testing ground for quantum chaos,” *Phys. Rev. Lett.* **73**, 2974 (1994).
- [38] Charles Kittel, *Introduction to Solid State Physics* (John Wiley and Sons, 1996).
- [39] M. B. d’Arcy, R. M. Godun, M. K. Oberthaler, D. Cassettari, and G. S. Summy, “Quantum Enhancement of Momentum Diffusion in the Delta-Kicked Rotor,” *Phys. Rev. Lett.* **87**, 074102-1, (2001).
- [40] G. Casati, B. V. Chirikov, F. M. Izraelev, and Joseph Ford, “Stochastic behavior of a quantum pendulum under a periodic perturbation,” in *Stochastic Behavior in Classical and Quantum Hamiltonian Systems*, edited by G. Casati and J. Ford (Springer, Berlin, 1979).
- [41] B.V. Chirikov, F.M. Izrailev and D.L. Shepelyansky, “Dynamical Stochasticity in Classical and Quantum Mechanics,” *Sov. Sci. Rev. C* **2 209** (1989).
- [42] D.L. Shepelyansky, “Some Statistical Properties of Simple Classically Stochastic Quantum Systems,” *Physica D* **8**, 208 (1983).

- [43] P. W. Anderson, “Absence of Diffusion in Certain Random Lattices,” *Phys. Rev.* **109**, 1492 (1958).
- [44] M. K. Oberthaler, R. M. Godun, M. B. dArcy, G. S. Summy, and K. Burnett, “Observation of Quantum Accelerator Modes,” *Phys. Rev. Lett.* **83**, 4447, (1999).
- [45] M. Sadgrove, M. Horikoshi, T. Sekimura, and K. Nakagawa, “Rectified Momentum Transport for a Kicked Bose-Einstein Condensate,” *Phys. Rev. Lett.* **99**, 043002, (2007).
- [46] S. N. Bose, “Plancks Gesetz und Lichtquantenhypothese,” *Z. Phys.* **26**, 178 (1924).
- [47] A. Einstein, “Quantentheorie des einatomigen idealen Gases. II,” *Sitzungsberichte der preussischen Akademie der Wissenschaften Bericht 1*, 3 (1925).
- [48] Peyman Ahmadi, “Investigating optical atom traps for Bose-Einstein Condensation,” Doctoral thesis, Oklahoma State University, July 2006.
- [49] Brian P. Timmons, “Dynamics of kicked laser cooled rubidium atoms,” Doctoral thesis, Oklahoma State University, July 2006.
- [50] Ghazal Behin Aein, “Quantum Chaos with a Bose-Einstein Condensate,” Doctoral thesis, Oklahoma State University, July 2007.
- [51] H. J. Metcalf, and P. van der Straten, *Laser Cooling and Trapping* (Springer-Verlag, New York, 1999).
- [52] S. Chu, L. Hollberg, J. E. Bjorkholm, A. Cable, and A. Ashkin, “Three dimensional viscous confinement and cooling of atoms by resonance radiation pressure,” *Phys. Rev. Lett.* **55**, 48 (1985).

- [53] S. Chu, J.E. Bjorkholm, A. Shkin, and A. Cable, “Experimental observation of optically trapped atoms,” *Phys. Rev. Lett.* **57** 314 (1986).
- [54] P. Lett, R. Watts, C. Westbrook, W. Phillips, P. Gould, and H. Metcalf, “Observation of Atoms Laser Cooled below the Doppler Limit,” *Phys. Rev. Lett.* **61**, 169 (1988).
- [55] J. Dalibard and C. Cohen-Tannoudji, “Laser Cooling Below the Doppler Limit by Polarization Gradients-Simple Theoretical Models,” *J. Opt. Soc. Am. B* **6**, 2023, (1989).
- [56] P. J. Ungar, D. S. Weiss, S. Chu, and E. Riis, “Optical Molasses and Multilevel Atoms-Theory,” *J. Opt. Soc. Am. B* **6**, 2058, (1989).
- [57] H. F. Hess, “Evaporative cooling of magnetically trapped and compressed spin-polarized hydrogen,” *Phys. Rev. B* **34** 3476 (1986).
- [58] J. M. Doyle, J. C. Sandberg, I. A. Yu, C. L. Cesar, D. Kellepner, and T. J. Greytak, “Hydrogen in the submillikelvin regime: Sticking probability on superfluid  $^4\text{He}$ ,” *Phys. Rev. Lett.* **67** 603 (1991).
- [59] K. B. Davis, M. O. Mewes, and W. Ketterle, “An analytical model for evaporative cooling of atoms,” *Appl. Phys. B* **60**, 155 (1995).
- [60] H. Wu, C. J. Foot, “Direct simulation of evaporative cooling,” *J. Phys. B.* **29**, L321 (1996).
- [61] V. Bagnato, D. E. Pritchard, and D. Kleppner, “Bose-Einstein Condensation in an External Potential,” *Phys. Rev. A* **35**, 4354 (1987).
- [62] T. Dittrich, P. Hänggi, G.-L. Ingold, B. Kramer, G. Schön, W. Zwerger, *Quantum Transport and Dissipation*, Wiley-VCH (1998).

- [63] A. V. Ponomarev, S. Denisov, P. Hänggi, “ac-Driven Quantum Motor,” *Phys. Rev. Lett.* **102**, 230601 (2009).
- [64] P. Ahmadi, G. BehinAein, V. Ramareddy, and G. S. Summy, “Creation Mechanism of Quantum Accelerator Modes,” *Phys. Rev. A.* **80**, 053418 (2009).
- [65] I. Guarneri, and L. Rebuzzini, “Quantum Accelerator Modes Near Higher-Order Resonances,” *Phys. Rev. Lett.* **100**, 234103 (2008).
- [66] C. Ryu, M. F. Andersen, A. Vaziri, M. B. dArcy, J. M. Grossman, K. Helmerson, and W. D. Phillips, “High-order quantum resonances observed in a periodically kicked Bose-Einstein Condensate,” *Phys. Rev. Lett.* **96**, 160403 (2006).
- [67] S. Fishman, I. Guarneri, and L. Rebuzzini, “Stable Quantum Resonances in Atom Optics,” *Phys. Rev. Lett.* **89**, 084101(2002).
- [68] S. Schlunk, M. B. d’Arcy, S. A. Gardiner, and G. S. Summy, “Experimental Observation of High-Order Quantum Accelerator Modes,” *Phys. Rev. Lett.* **90**, 124102 (2003).
- [69] S. Fishman, I. Guarneri, and L. Rebuzzini, “A Theory for Quantum Accelerator Modes in Atom Optics,” *J. Stat. Phys.* **110**, 911 (2003).
- [70] V. Ramareddy, G. BehinAein, I. Talukdar, P. Ahmadi, and G. S. Summy, “High-order Resonances of the Quantum  $\delta$ -kicked accelerator,” *Eur. Phys. Lett.* **89**, 33001 (2010).
- [71] M. V. Berry, and S. Klein, “Integer, fractional and fractal Talbot effects,” *J. Mod. Opt.* **43**, 2139 (1996).
- [72] R. P. Feynman, R. B. Leighton, and M. Sands, *The Feynman Lectures on Physics*, (Vol. 1, Addison-Wesley, Reading, MA, 1963).

- [73] P. Reimann, “Brownian motors: noisy transport far from equilibrium,” *Phys. Rep.* **361**, 57 (2002).
- [74] E. Lundh, and M. Wallin, “Ratchet Effect for Cold Atoms in an Optical Lattice,” *Phys. Rev. Lett.* **94**, 110603 (2005).
- [75] P. H. Jones, M. Goonasekera, D. R. Meacher, T. Jonckheere, and T. S. Monteiro, “Directed Motion for Delta-Kicked Atoms with Broken Symmetries: Comparison between Theory and Experiment,” *Phys. Rev. Lett.* **98**, 073002 (2007).
- [76] I. Dana, and V. Roitberg, “Quantum resonances and ratchets in free-falling frames,” *Phys. Rev. E* **76**, 015201 (2007).
- [77] Vijayashankar Ramareddy, “Quantum chaos using delta kicked systems”, Doctoral thesis, Oklahoma State University, December 2008.
- [78] M. Sadgrove, S. Kumar, and K. Nakagawa, “Signal analysis with atom optics,” *Phys. Rev. A* **79**, 053618 (2009).
- [79] F. S. Cataliotti, R. Scheunemann, T. W. Hänsch, and M. Weitz, “Superresolution of Pulsed Multiphoton Raman Transitions,” *Phys. Rev. Lett.* **87**, 113601 (2001).
- [80] S. Wimberger, I. Guarneri, and S. Fishman, “Quantum Resonances and Decoherence for  $\delta$ -kicked atoms,” *Nonlinearity* **16**, 1381 (2003).
- [81] *Atom Interferometry*, edited by P. R. Berman (Academic, San Diego, 1997).
- [82] J. M. McGuirk, M. J. Snadden, and M. A. Kasevich, “Large Area Light-Pulse Atom Interferometry,” *Phys. Rev. Lett.* **85**, 4498 (2000).
- [83] K. J. Hughes, J. H. T. Burke, and C. A. Sackett, “Suspension of Atoms Using Optical Pulses, and Application to Gravimetry,” *Phys. Rev. Lett.* **102**, 150403 (2009).

- [84] T. Lévèque, A. Gauguet, F. Michaud, F. Pereira Dos Santos, and A. Landragin, “Enhancing the Area of a Raman Atom Interferometer Using a Versatile Double-Diffraction Technique,” *Phys. Rev. Lett.* **103**, 080405 (2009).
- [85] A. Peters, K. Y. Chung, and S. Chu, “Measurement of gravitational acceleration by dropping atoms,” *Nature*, **400**, 849 (1999).
- [86] D. S. Weiss, B. C. Young, and S. Chu, “Precision Measurement of the Photon Recoil of an Atom Using Atomic Interferometry,” *Phys. Rev. Lett.*, **70**, 2706 (1993).
- [87] P. Cladé, E. de Mirandes, M. Cadoret, S. Guellati-Khelifa, C. Schwob, F. Nez, L. Julien and F. Biraben<sup>1</sup>, “Determination of the Fine Structure Constant Based on Bloch Oscillations of Ultracold Atoms in a Vertical Optical Lattice,” *Phys. Rev. Lett.* **96** 033001 (2006).
- [88] M. Cadoret, E. de Mirandes, P. Cladé, S. Guellati-Khélifa, C. Schwob, F. Nez, L. Julien, and F. Biraben, “Combination of Bloch Oscillations with a Ramsey-Bordé Interferometer: New Determination of the Fine Structure Constant,” *Phys. Rev. Lett.* **101** 230801 (2008).
- [89] J. B. Fixler, G. T. Foster, J. M. McGuirk, M. A. Kasevich, “Atom Interferometer Measurement of the Newtonian Constant of Gravity,” *Science*, **315**, 74 (2007).
- [90] P. McDowall, A. Hilliard, M. McGovern, T. Grünzweig, and M. F. Andersen, “A fidelity treatment of near-resonant states in the atom-optics kicked rotor,” *New J. Phys.* **11**, 123021 (2009).
- [91] S. Wimberger, I. Guarneri, and S. Fishman, “Classical Scaling Theory of Quantum Resonances,” *Phys. Rev. Lett.* **92**, 084102 (2004).



- [92] C. Ryu, M. F. Andersen, A. Vaziri, M. B. dArcy, J. M. Grossman, K. Helmerson, and W. D. Phillips, “High-Order Quantum Resonances Observed in a Periodically Kicked Bose-Einstein Condensate,” *Phys. Rev. Lett.* **96**, 160403 (2006).
- [93] I. Talukdar, R. Shrestha, and G. S. Summy, “Sub-Fourier Characteristics of a  $\delta$ -kicked-rotor Resonance,” *Phys. Rev. Lett.*, **105**, 054103 (2010).
- [94] M.-S. Chang, C. D. Hamley, M. D. Barrett, J. A. Sauer, K.M. Fortier, W. Zhang, L. You, and M. S. Chapman, “Observation of Spinor Dynamics in Optically Trapped  $^{87}\text{Rb}$  Bose-Einstein Condensates,” *Phys. Rev. Lett.* **92**, 140403 (2004).
- [95] S. Wimberger, M. Sadgrove, S. Parkins, and R. Leonhardt, “Experimental verification of a one-parameter scaling law for the quantum and “classical” resonances of the atom-optics kicked rotor,” *Phys. Rev. A* **71**, 053404 (2005).
- [96] J. Martin, B. Georgeot, and D. L. Shepelyansky, “Cooling by Time Reversal of Atomic Matter Waves,” *Phys. Rev. Lett.* **100**, 044106 (2008).
- [97] J. Martin, B. Georgeot, and D. L. Shepelyansky, “Time Reversal of Bose-Einstein Condensates,” *Phys. Rev. Lett.* **101**, 074102 (2008).
- [98] T. S. Monteiro, A. Rançon, and J. Ruostekoski, “Nonlinear Resonances in  $\delta$ -Kicked Bose-Einstein Condensates,” *Phys. Rev. Lett.* **102**, 014102 (2009).
- [99] S. Wimberger, R. Mannella, O. Morsch, and E. Arimondo, “Resonant Nonlinear Quantum Transport for a Periodically Kicked Bose Condensate,” *Phys. Rev. Lett.* **94**, 130404 (2005).
- [100] S. A. Gardiner, D. Jaksch, R. Dum, J. I. Cirac, and P. Zoller, “Nonlinear matter wave dynamics with a chaotic potential,” *Phys. Rev. A* **62**, 023612 (2000).
- [101] P. M. Solomon, “The Absorption Coefficient of Quasi-Molecular Hydrogen,” *Astrophys. J.* **139**, 999 (1964).

- [102] J. H. Schloss, R. B. Jones, and J. G. Eden, “Wavelength dependence of the photoassociation of  $\text{Kr}(4p^6\ ^1S_0)$ - $\text{F}(2p^5\ ^2P)$  collision pairs,” *Chem. Phys. Lett.* **191** 195 (1992).
- [103] H. R. Thorsheim, J. Weiner, and P. S. Julienne, “Laser-Induced Photoassociation of Ultracold Sodium Atoms,” *Phys. Rev. Lett.* **58**, 2420 (1987).
- [104] J. D. Miller, R. A. Cline, and D. J. Heinzen, “Photoassociation Spectrum of Ultracold Rb atoms,” *Phys. Rev. Lett.* **71**, 2204 (1993).
- [105] R. A. Cline, J. D. Miller, and D. J. Heinzen, “Study of  $\text{Rb}_2$  Long-Range States by High-Resolution Photoassociation Spectroscopy,” *Phys. Rev. Lett.* **73**, 632 (1994).
- [106] K. M. Jones, E. Tiesinga, P. D. Lett, and P. S. Julienne, “Ultracold photoassociation spectroscopy: Long-range molecules and atomic scattering,” *Rev. Mod. Phys.* **78**, 483 (2006).
- [107] A. Fioretti, D. Comparat, A. Crubellier, O. Dulieu, F. Masnou-Seeuws, and P. Pillet, “Formation of Cold  $\text{Cs}_2$  Molecules through Photoassociation,” *Phys. Rev. Lett.* **80**, 4402 (1998).
- [108] E. A. Donley, N. R. Claussen, S. L. Cornish, J. L. Roberts, E. A. Cornell, and C. E. Wieman, “Dynamics of collapsing and exploding Bose-Einstein condensates,” *Nature* **412**, 295 (2001).
- [109] E. Tiesinga, B. J. Verhaar, and H. T. C. Stoof, “Threshold and resonance phenomena in ultracold ground-state collisions,” *Phys. Rev. A* **47**, 4114 (1993).
- [110] S. Inouye, M. R. Andrews, J. Stenger, H.-J. Miesner, D. M. Stamper-Kurn, and W. Ketterle, “Observation of Feshbach resonances in a Bose-Einstein condensate,” *Nature(London)* **392**, 151 (1998).

- [111] P. O. Fedichev, Yu. Kagan, G. V. Shlyapnikov, and J. T. M. Walraven, “Influence of Nearly Resonant Light on the Scattering Length in Low-Temperature Atomic Gases,” *Phys. Rev. Lett.* **77**, 2913 (1996).
- [112] J. L. Bohn, and P. S. Julienne, “Prospects for influencing scattering lengths with far-off-resonant light,” *Phys. Rev. A* **56**, 1486 (1997).
- [113] F. K. Fatemi, K. M. Jones, and P. D. Lett, “Observation of Optically Induced Feshbach Resonances in Collisions of Cold Atoms,” *Phys. Rev. Lett.* **85**, 4462 (2000).
- [114] M. Theis, G. Thalhammer, K. Winkler, M. Hellwig, G. Ruff, R. Grimm and J. Hecker Denschlag, “Tuning the Scattering Length with an Optically Induced Feshbach Resonance,” *Phys. Rev. Lett.* **93**, 123001 (2004).
- [115] M. Theis, “Optical Feshbach Resonances in a Bose-Einstein Condensate,” Ph.D. thesis, University of Innsbruck, Innsbruck, April 2005.
- [116] M. Hellwig, “Stabilisierung von Laser-Systemen für Experimente mit ultrakalten Atomen,” Master’s thesis, University of Innsbruck, Innsbruck, 2005.
- [117] A. Fioretty, C. Amiot, C. M. Dion, O. Dulieu, M. Mazzonik, G. Smirne, and C. Gabbanini, “Cold rubidium molecule formation through photoassociation: A spectroscopic study of the  $0_g^-$  long-range state of  $^{87}\text{Rb}_2$ ,” *Eur. Phys. J. D* **15**, 189, (2001).
- [118] C. D. Hamley, E. M. Bookjans, G. Behin-Aein, P. Ahmadi, and M. S. Chapman, “Photoassociation spectroscopy of a spin-1 Bose-Einstein condensate,” *Phys. Rev. A* **79**, 023401 (2009).

- [119] J. Stenger, S. Inouye, A. P. Chikkatur, D. M. Stamper-Kurn, D. E. Pritchard, and W. Ketterle, “Bragg Spectroscopy of a Bose-Einstein Condensate,” *Phys. Rev. Lett.* **82**, 4569 (1999).
- [120] C. McKenzie, J. Hecker Denschlag, H. Häffner, A. Browaeys, Luís E. E. de Araujo, F.K . Fatemi, K. M. Jones, J. E. Simsarian, D. Cho, A.Simoni, E. Tiesinga, P. S. Julienne, K. Helmerson, P. D. Lett, S. L.Rolston, and W. D. Phillips, “Photoassociation of Sodium in a Bose-Einstein Condensate,” *Phys. Rev. Lett.* **88**, 120403 (2002).
- [121] E. W. Hagley, L. Deng, M. Kozuma, M. Trippenbach, Y. B. Band, M. Edwards, M. Doery, P. S. Julienne, K. Helmerson, S. L. Rolston, and W. D. Phillips, “Measurement of the Coherence of a Bose-Einstein Condensate,” *Phys. Rev. Lett.* **83**, 3112, (1999).
- [122] G. Thalhammer, M. Theis, K. Winkler, R. Grimm, and J. H. Denschlag, “Inducing an optical Feshbach resonance via stimulated Raman coupling,” *Phys. Rev. A.* **71** 033403 (2005).
- [123] D. M. Bauer, M. Lettner, C. Vo, G. Rempe and S. Dür, “Control of a magnetic Feshbach resonance with laser light,” *Nature Phys.* **5**, 339 (2009).

## APPENDIX A

### Publications

## High-order resonances of the quantum $\delta$ -kicked accelerator

V. RAMAREDDY<sup>1(a)</sup>, G. BEHINAEIN<sup>1,2</sup>, I. TALUKDAR<sup>1</sup>, P. AHMADI<sup>1,2</sup> and G. S. SUMMY<sup>1</sup>

<sup>1</sup> *Department of Physics, Oklahoma State University - Stillwater, OK 74078-3072, USA*

<sup>2</sup> *Department of Physics, MIT-Harvard Center for Ultracold Atoms, and Research Laboratory of Electronics, Massachusetts Institute of Technology - Cambridge, MA 02139, USA*

received 25 August 2009; accepted in final form 19 January 2010  
published online 19 February 2010

PACS 37.10.Jk – Atoms in optical lattices  
PACS 05.45.Mt – Quantum chaos; semiclassical methods

**Abstract** – We report the observation of high-order resonances of the quantum  $\delta$ -kicked accelerator using a BEC kicked by a standing wave of light. The signature of these resonances is the existence of quantum accelerator modes. For the first time quantum accelerator modes were seen near  $1/2$ ,  $2/3$  and  $1/3$  of the half-Talbot time. Using a BEC enabled the internal momentum state structure of the modes and resonances to be studied for the first time. This structure has many similarities to that present in the fractional Talbot effect. We present a theory for this system based on rephasing of momentum orders and apply it to predict the behavior of the accelerator modes around a resonance of any order.

Copyright © EPLA, 2010

Over the last decade the availability of ultra-cold atoms and the development of atom optical techniques has led to a revolution in the study of quantum chaotic systems. These techniques have allowed the quantum-chaotic dynamics of cold atoms subject to kicks from a standing wave of laser light to be observed in great detail. This system has been used in realizing the atom optics versions of the quantum  $\delta$ -kicked rotor (QDKR) [1] and the quantum  $\delta$ -kicked accelerator [2,3]. Other interesting classes of kicked systems studied theoretically include the kicked harmonic oscillator [4] and kicked Harper model [5].

One aspect of the behavior of these kicked systems that is of particular interest is the phenomenon of quantum resonance [6]. These resonances occur at distinct kicking periods and are characterized by a quadratic increase in the kinetic energy of atoms with certain initial momenta. To date most work has concentrated on the most easily observed of these resonances in the QDKR. These occur when the kicking period is an integer multiple of the half-Talbot time [7]. However, quantum resonances can also occur at kicking periods that are rational fractions  $a/b$  (where  $a$  and  $b$  are integers) of the half-Talbot time [8]. These are what are known as “high-order” quantum resonances, with  $b$  being the order of the resonance. Several of these resonances have been observed for the QDKR using both BEC [9] and a thermal sample of atoms [10]. High-order resonances have also been investigated theoretically

for a  $\delta$ -kicked system within a harmonic potential (the  $\delta$ -kicked harmonic oscillator) [11]. Nevertheless, even though the signatures of a few high-order resonances have been detected, their rich internal structure has never been directly observed in any system.

In this letter we present the results of experiments using a Bose-Einstein condensate which show the structure and dynamics that gives rise to the quantum resonances. This is achieved through the first observation of quantum resonances of order 3, 4, and 6 in a QDKR which has been modified by the addition of a static linear potential created with the Earth’s gravity. Such a system is known as the quantum  $\delta$ -kicked accelerator (QDKA). The resonances can be described using two theoretical frameworks: one taking an approach where the quantum system is modeled using a classical-like mapping [12]; the other which is presented in this paper is based on the fractional Talbot effect [7] where the atom-light interaction is considered as diffraction at a phase grating. These complimentary pictures enable us to predict the ensemble behavior of the system and to explain the internal momentum state (diffraction order) structure of the quantum resonances observed in the experiments. Interference between these momentum states is also the reason that only atoms with certain initial momenta can participate in the resonance.

For the QDKA, the presence of the linear potential breaks the symmetry and allows a fixed momentum per kick to be imparted to a subset of atoms when the pulse period is close to a resonance time. Atoms which

<sup>(a)</sup>E-mail: vijay.ramareddy@gmail.com

are kicked in such a way are said to be in a quantum accelerator mode (QAM) [3]. Fishman, Guarneri and Rebuzzini (henceforth referred to as FGR) developed a framework called  $\epsilon$ -classical theory [13], where a parameter  $\epsilon$  proportional to the difference of the pulse period from one of the primary resonances plays the role of Planck's constant. In the limit of pulse period very close to a primary resonance time, ( $\epsilon \rightarrow 0$ ), a classical mapping can be used to describe the system. This theory has been modified to develop a model for the QAM near high-order resonances [12]. The kicked accelerator can be described using a Hamiltonian

$$H = P^2/2M - Mg'x + \hbar\phi_d \cos(Gx) \sum_n \delta(t' - nT), \quad (1)$$

where the first term represents the kinetic energy ( $P$  is the atomic momentum,  $M$  is the atomic mass), the second term is a linear potential ( $g'$  is an acceleration in the direction of the pulsed standing wave,  $x$ ), and the third term is the  $\delta$ -kicked potential ( $\phi_d$  is the kicking strength,  $G = 2\pi/\lambda_G$ ,  $\lambda_G$  is the spatial period of the potential,  $T$  is the kicking period). One possible way to understand QAMs at high order resonances is to use the approach developed by FGR at the primary resonances where the single-kick evolution operator is written in a frame falling with the acceleration  $g'$  as  $U_\beta(t) = e^{-\frac{i}{\hbar} \hat{k} \cos \hat{\theta}} e^{-\frac{i}{\hbar} \hat{H}_\beta}$ , where  $\hat{H}_\beta = \frac{1}{2} \hat{I}^2 + \hat{I}(\pi l + \tau(\beta + t\eta + \eta/2))$  describes the effective Hamiltonian for free evolution between any two kicks separated by a time interval close to the resonance time  $lT_{1/2}$  (where  $l$  is an integer and  $T_{1/2} = \frac{2\pi M}{\hbar G^2}$  is the half-Talbot time). The position and momentum co-ordinates are now represented by  $\theta = Gx \bmod 2\pi$ , and  $\hat{I} = -i\epsilon \frac{d}{d\theta}$ , respectively, and time represented by  $\tau = 2\pi T/T_{1/2}$ , with the parameter  $\epsilon = 2\pi(T/T_{1/2} - l)$  measuring the closeness of the kick period to the primary resonance  $lT_{1/2}$ . Note that  $\epsilon$  appears in the place of Planck's constant in the evolution operator and hence can formally be regarded as  $\hbar$ . Other variables include the quasimomentum  $\beta$ , the scaled kicking strength  $\hat{k} = \epsilon\phi_d$ , and the scaled acceleration  $\eta = Mg'T/(\hbar G)$ . As with the kicked rotor, high-order resonances are expected when  $T$  is a rational fraction ( $a/b$ ) of  $T_{1/2}$  [8,9].

By analogy, for the high-order resonances  $\epsilon$  can be defined as  $\epsilon = 2\pi(T/T_{1/2} - a/b)$  and for small  $|\epsilon|$ , treating  $\epsilon$  as Planck's constant, the dynamics of the kicked accelerator near a higher-order resonance can be described using a mapping [12]

$$\begin{aligned} J_{t+1} &= J_t + \hat{k} \sin(\theta_{t+1}) + \eta\tau + \Delta S_t \\ \theta_{t+1} &= \theta_t + J_t, \end{aligned} \quad (2)$$

where  $J_t = I_t + \tau(\Delta\beta + t\eta + \eta/2) + 2\pi S_t/b$ , and  $\Delta S_t = 2\pi(S_{t+1} - S_t)/b$ . The integers  $S_t$  can take values from 1 to  $b$  and are arbitrary. Thus there are  $b^t$  maps for a given set of experimental parameters. For a periodic orbit with period  $p$ , jumping index  $j$ , satisfying equation

$J_{(t+p)q} = J_{tq} + 2\pi j$ , where  $q$  is an integer satisfying equation  $\Delta S_{t+q} = \Delta S_t$  [12], the average momentum is given by [12]

$$\bar{p}_{\text{QAM}} = -t \frac{\eta\tau}{\epsilon} + \left( 2\pi \frac{j}{p} - \sum_{r=0}^{q-1} \Delta S_r \right) \frac{t}{q}. \quad (3)$$

The QAM with  $j \neq 0$  are termed as higher-order QAM [14]. For the simple case of  $\Delta S_r = 0$ , and primary QAM ( $j = 0$ ), the mean momentum of the periodic orbits is given by only the first term of eq. (3), identical to the ones at primary resonances. The mapping of this simple case is shown for two different higher-order resonances in fig. 3.

The general signature of a quantum resonance of the quantum  $\delta$ -kicked accelerator is expected to be the asymptotic divergence of a QAM's momentum,  $\bar{p}_{\text{QAM}}$ , to infinity as  $\epsilon \rightarrow 0$ , that is, when the kicking period approaches the high-order resonance time. To experimentally observe these quantum resonances we subjected a BEC to pulses of standing wave light as described in detail in [2]. In brief, the BEC was created in an optical trap and consisted of approximately 30000 Rb-87 atoms in the  $F = 1, 5S_{1/2}$  level. After release from the trap, the BEC was kicked by 780 nm light which was 6.8 GHz detuned to the red of the atomic transition. For this detuning and  $\phi_d \sim 2$  (the maximum used in the experiments) the spontaneous emissions per pulse for each atom is negligible at about  $1.8 \times 10^{-3}$ . This light propagated through two acousto-optic modulators (AOMs) to control the initial momentum and the acceleration of the atoms with respect to the standing wave. This was accomplished by driving the two AOMs with different frequencies. The kicking beam was oriented at  $52^\circ$  to the vertical. Overall these parameters gave a value for the half-Talbot time of  $T_{1/2} = 33.15 \mu\text{s}$ . In order to vary the kicking strength  $\phi_d$ , the length of the kicking pulses was adjusted. Typically the pulse length was set at  $1.8 \mu\text{s}$  giving  $\phi_d \approx 1.5$ . The finite pulse length does affect the dynamics of the system, particularly for states having momenta greater than  $\sim 10\hbar G$ . At our pulse lengths, such a state would move a significant fraction ( $\sim 0.6$ ) of the standing wavelength. However, it is still possible to consider this system as a  $\delta$ -kicked rotor but with a reduced  $\phi_d$  [15]. This is one of the factors which makes it difficult to observe high-order resonances since they require a large value of  $\phi_d$  to become visible (see following discussion). The value of  $\phi_d$  was estimated by comparing the relative population of various diffraction orders after one kick. Note that the population in the  $n$ -th state is given in terms of Bessel functions via  $|J_n(\phi_d)|^2$  [16]. The momentum distribution of the BEC was measured by taking an absorption image 8 ms after the completion of the kicking sequence. Finally it should be noted that the mean-field energy was weak enough that it could be ignored, making the Hamiltonian of the  $\delta$ -kicked accelerator a valid approximation.

Figure 1 shows experimental scans of the kicking period across two different high-order resonances. These figures were generated by horizontally stacking the absorption

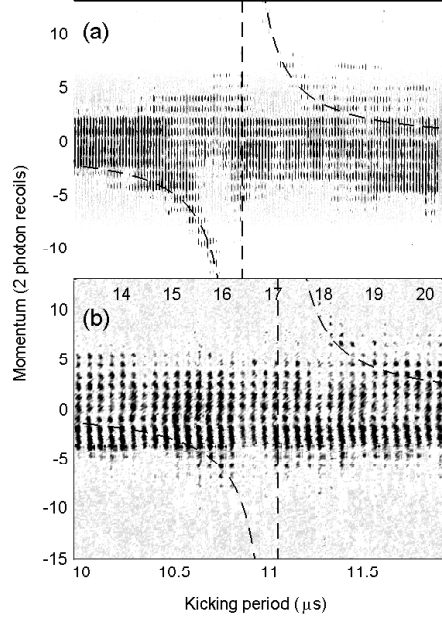


Fig. 1: Horizontally stacked momentum distributions for different kicking periods for (a) 40 kicks across  $(1/2)T_{1/2}$  ( $a=1$  and  $b=2$ ) for the effective acceleration  $g'=6\text{ ms}^{-2}$ , and  $\phi_d=1.4$ ; (b) 30 kicks across  $(1/3)T_{1/2}$  ( $a=1$  and  $b=3$ ),  $g'=4.5\text{ ms}^{-2}$  and  $\phi_d=1.8$ . The initial momentum was chosen such that the part of the mode below the resonance time is populated more strongly in the case of (a) and vice versa in the case of (b). The dashed curve is that of the  $\epsilon$ -classical theory in eq. (3).

images each with a different kick period. The dashed curves are the QAM momenta predicted by the  $\epsilon$ -classical theory of eq. (3). It can be seen that the theory provides a good description of the momentum transfer to the QAM, although the experimental signal is quite weak especially for the  $(1/3)T_{1/2}$  data in fig. 1(b).

To investigate the properties of the QAM about the high-order resonances further, we conducted a series of experiments where kick number was increased at a fixed kicking period close to a resonance. Figure 2(a) is a scan of number of kicks close to  $(2/3)T_{1/2}$ . This hints that the QAM consists primarily of momentum states separated by  $3\hbar G$  (indicated by horizontal arrows). The scan of kick number close to  $(1/2)T_{1/2}$  of fig. 2(b) shows much more clearly that the QAM is composed of momentum states separated by  $2\hbar G$ . These momentum states are again emphasized by horizontal arrows. In contrast, at the Talbot time ( $2T_{1/2}$ ), the QAM includes neighboring

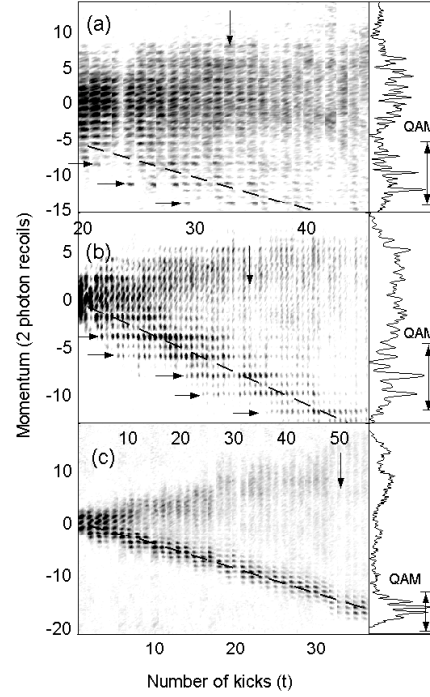


Fig. 2: Horizontally stacked momentum distributions as a function of number of kicks ( $t$ ) for (a)  $T=22.68\text{ }\mu\text{s}$ , which is close to  $(2/3)T_{1/2}$ , (b)  $T=17.1\text{ }\mu\text{s}$ , which is close to  $(1/2)T_{1/2}$ , and (c)  $T=72.4\text{ }\mu\text{s}$  which is close to  $2T_{1/2}$ . Note the different axes for (a), (b) and (c). The horizontal arrows in (a) and (b) show that primarily orders separated by  $b\hbar G$  participate in each of the QAMs. Dashed lines show the position of the QAM predicted by the  $\epsilon$ -classical theory of eq. (3). The end panels show the momentum distribution for 33 kicks (denoted by the downward arrow in the main panels). The value of  $g'=6\text{ ms}^{-2}$  for these experiments. The location of the QAMs are shown by the vertical double arrows.

momentum states as seen from fig. 2(c). The right hand side of each of these figures shows a plot of the population *vs.* momentum at 33 kicks (vertical arrows). Note again the separation of  $b\hbar G$  between the momentum states participating in a QAM. This behavior suggests that the QAM around the high-order resonances can form whenever the momentum orders separated by  $b\hbar G$  rephase during the time between the kicks. This is analogous to what has been postulated to occur (but never directly observed) for the kicked rotor resonances [9], and is consistent with what is known of the fractional Talbot effect [7].



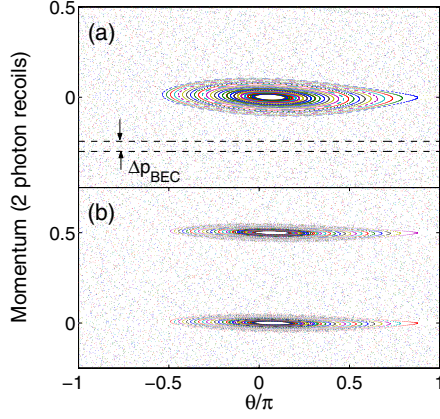


Fig. 3: (Colour on-line) Phase space plot of the map (2) for (a)  $\phi_d = 1.5$ ,  $g' = 6 \text{ ms}^{-2}$  and  $T = 17.1 \mu\text{s}$ , which is close to  $(1/2) T_{1/2}$ , and (b)  $\phi_d = 1.8$ ,  $g' = 4.5 \text{ ms}^{-2}$  and  $T = 22.68 \mu\text{s}$  which is close to  $(2/3) T_{1/2}$ . When a wave packet is trapped in an island, a QAM is formed [13]. The dashed lines in (a) show the width of the BEC.

Given this structure it is now possible to explain why an increased  $\phi_d$  is needed to observe QAMs near resonances with larger  $b$ . Since the range of momentum orders populated by a single kick is approximately proportional to  $\phi_d$ ,  $\phi_d$  must be increased at the high-order resonances so that a single kick can diffract into a range of states comparable to  $b\hbar G$  (the separation between the states participating in the QAM). Recall that the population of a momentum state  $n\hbar G$  is proportional to  $|J_n(\phi_d)|^2$  after a single diffraction event, with the highest population occurring in the state  $n \sim \phi_d$ . Paradoxically the high  $\phi_d$  needed at these large  $b$  resonances can also make it difficult to observe QAMs since the distribution of momentum states that do not participate in a QAM broadens as  $\phi_d$  is increased. This can mask the presence of a QAM in either a scan of kick period or kick number especially in the case of experiments with only a few kicks.

The internal momentum state structure can also affect the initial condition of atoms that can participate in a QAM. To see this we take the formation of a QAM to necessitate that the phase difference between the constituent momentum states  $m\hbar G$  and  $(m-b)\hbar G$  be an integer multiple of  $2\pi$  after the free evolution between the kicks. Following the procedure of [16], along with the result that the momentum of states participating in a QAM increases linearly with time (first term of eq. (3)), we obtain the condition on the initial momentum (in units of  $\hbar G$ ) at which a QAM appears as

$$p_i = \frac{2\pi l'}{\tau b} + \frac{b}{2} - \frac{\eta}{2b}, \quad (4)$$

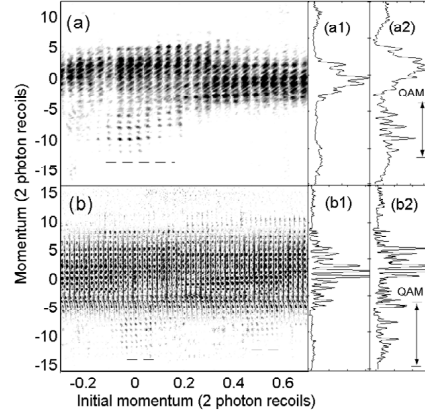


Fig. 4: Horizontally stacked momentum distributions as a function of the initial momentum of the BEC before kicking. (a) 30 kicks with a period of  $17.1 \mu\text{s}$  (close to  $(1/2)T_{1/2}$ ,  $a = 1$ ), and  $g' = 6 \text{ ms}^{-2}$ , (b) 40 kicks with the period of  $22.53 \mu\text{s}$  (close to  $(2/3)T_{1/2}$ ,  $a = 2$ ), and  $g' = 4.5 \text{ ms}^{-2}$ . The position of the modes are indicated by the dashed lines. The panels (a1) and (b1) show the final momentum distribution for initial momenta at which a QAM does not appear. Panels (a2) and (b2) correspond to initial momenta at which a QAM is seen. The momentum range of QAMs is shown as double arrows in (a2) and (b2).

where  $l'$  is an integer. It can be seen that the QAMs in the  $\delta$ -kicked accelerator are spaced in initial momentum by  $\Delta p_i = 2\pi/\tau b \approx 1/a$ . This implies that the islands in the phase space map (which are attributed to the existence of the QAMs [13]) shown in fig. 3 are separated in momentum by  $\hbar G/a$ . Figure 3 shows these phase space islands close to  $(1/2)T_{1/2}$  in fig. 3(a) and  $(2/3)T_{1/2}$  in fig. 3(b). The momentum axes in these maps cover a range of  $1\hbar G$ .

Thus to resolve the structures in phase-space within a unit cell and test the theory of eq. (4), it is necessary that the momentum width be much narrower than  $\hbar G/a$ . In our experiments the BEC had a momentum width of  $0.056 \hbar G$  [17] which makes it an excellent candidate for this task. The size of the BEC in momentum is shown in fig. 3(a) with two dashed lines. In the  $\theta$  direction, BEC stretches across the whole phase space. Figure 4 shows the results from experiments in which the effective initial momentum of the BEC was changed by moving the standing wave using a difference in frequency between the kicking AOMs. This is equivalent to taking the strip shown between the dashed lines in fig. 3(a) and scanning it through the unit cell. The kicking period was near  $(1/2)T_{1/2}$  in fig. 4(a) and  $(2/3)T_{1/2}$  in fig. 4(b). Over a range of  $1\hbar G$  of initial momentum, the QAM appears once at  $(1/2)T_{1/2}$  and twice at  $(2/3)T_{1/2}$ . This demonstrates that the initial momenta at which the modes exist are

33001-p4

separated by  $\hbar G$  in the case of  $(1/2)T_{1/2}$  ( $a = 1$ ) and  $\hbar G/2$  for  $(2/3)T_{1/2}$  ( $a = 2$ ) in agreement with eq. (4).

In conclusion, we have experimentally demonstrated the existence of high-order resonances in the quantum  $\delta$ -kicked accelerator. This was possible through the observation of QAMs near these resonances. The narrow momentum distribution of the BEC allowed us to observe the momentum state structure of the QAMs. It was found that QAMs near high-order resonances have a structure which is reminiscent of that produced by the fractional Talbot effect. Furthermore, we were able to explore the phase space structures predicted by  $\epsilon$ -classical theory of high-order resonances. This work opens the door towards the study of high-order QAMs [14] near high-order resonances. Other interesting questions include the effect of stronger mean-field interactions [18], the enhancement of QAM population using more complex initial states, and the effect of finite pulse length.

#### REFERENCES

- [1] MOORE F. L. *et al.*, *Phys. Rev. Lett.*, **73** (1994) 2974; AMMANN H. *et al.*, *Phys. Rev. Lett.*, **80** (1998) 4111; DENG L. *et al.*, *Phys. Rev. Lett.*, **83** (1999) 5407; WIMBERGER S., GUARNERI I. and FISHMAN S., *Phys. Rev. Lett.*, **92** (2004) 084102; WIMBERGER S. *et al.*, *Nonlinearity*, **16** (2003) 1381; FISHMAN S. *et al.*, *Phys. Rev. Lett.*, **49** (1982) 509; CHAB J. *et al.*, *Phys. Rev. Lett.*, **97** (2006) 264101; WIMBERGER S. *et al.*, *Phys. Rev. A*, **71** (2005) 053404.
- [2] BEHINAEIN G., RAMAREDDY V., AHMADI P. and SUMMY G. S., *Phys. Rev. Lett.*, **97** (2006) 244101.
- [3] OBERTHALER M. K. *et al.*, *Phys. Rev. Lett.*, **83** (1999) 4447.
- [4] DANA I., *Phys. Rev. Lett.*, **73** (1994) 1609; CARVALHO A. R. R. and BUCHLEITNER A., *Phys. Rev. Lett.*, **93** (2004) 204101.
- [5] ARTUSO R., CASATI G., BERGONOV F., REBUZZINI L. and GUARNERI I., *Int. J. Mod. Phys. B*, **8** (1994) 207.
- [6] MOORE F. L., ROBINSON J. C., BHARUCHA C. F., SUNDARAM B. and RAIZEN M. G., *Phys. Rev. Lett.*, **75** (1995) 4598; D'ARCY M. B., GODUN R. M., OBERTHALER M. K., CASSETTARI D. and SUMMY G. S., *Phys. Rev. Lett.*, **87** (2001) 074102.
- [7] BERRY M. V. and BODENSCHATZ E., *J. Mod. Opt.*, **46** (1999) 349; BERRY M. V. and KLEIN S., *J. Mod. Opt.*, **43** (1996) 2139.
- [8] IZRAILEV F. M. and SHEPELYANSKII D. L., *Sov. Phys. Dokl.*, **24** (1979) 996; *Theor. Math. Phys.*, **43** (1980) 553.
- [9] RYU C. *et al.*, *Phys. Rev. Lett.*, **96** (2006) 160403.
- [10] KANEM J. F. *et al.*, *Phys. Rev. Lett.*, **98** (2007) 083004.
- [11] WIMBERGER S. *et al.*, *Phys. Rev. Lett.*, **94** (2005) 130404.
- [12] GUARNERI S. *et al.*, *Phys. Rev. Lett.*, **100** (2008) 234103.
- [13] FISHMAN S., GUARNERI I. and REBUZZINI L., *Phys. Rev. Lett.*, **89** (2002) 084101; *J. Stat. Phys.*, **110** (2003) 911.
- [14] SCHLUNK S. *et al.*, *Phys. Rev. Lett.*, **90** (2003) 124102.
- [15] D'ARCY M. B. *et al.*, *Phys. Rev. E*, **64** (2001) 056233.
- [16] GODUN R. M. *et al.*, *Phys. Rev. A*, **62** (2000) 013411.
- [17] DANA I., RAMAREDDY V., TALUKDAR I. and SUMMY G. S., *Phys. Rev. Lett.*, **100** (2008) 024103.
- [18] REBUZZINI L. *et al.*, *Phys. Rev. A*, **76** (2007) 031603R.

## Experimental Realization of Quantum-Resonance Ratchets at Arbitrary Quasimomenta

I. Dana,<sup>1</sup> V. Ramareddy,<sup>2</sup> I. Talukdar,<sup>2</sup> and G. S. Summy<sup>2</sup><sup>1</sup>*Minerva Center and Department of Physics, Bar-Ilan University, Ramat-Gan 52900, Israel*<sup>2</sup>*Department of Physics, Oklahoma State University, Stillwater, Oklahoma 74078-3072, USA*

(Received 25 April 2007; revised manuscript received 30 August 2007; published 17 January 2008)

Quantum-resonance ratchets associated with the kicked particle are experimentally realized for *arbitrary quasimomentum* using a Bose-Einstein condensate (BEC) exposed to a pulsed standing light wave. The ratchet effect for general quasimomentum arises even though both the standing-wave potential and the initial state of the BEC have a point symmetry. The experimental results agree well with theoretical ones which take into account the finite quasimomentum width of the BEC. In particular, this width is shown to cause a *suppression* of the ratchet acceleration for exactly resonant quasimomentum, leading to a saturation of the directed current.

DOI: 10.1103/PhysRevLett.100.024103

PACS numbers: 05.45.Mt, 03.75.Kk, 05.60.Gg, 37.10.Vz

Understanding quantum transport in classically chaotic systems is a problem of both fundamental and practical importance. A wide variety of interesting quantum-transport phenomena have been discovered in simple but representative quantized models of Hamiltonian dynamics [1]. These phenomena either exhibit fingerprints of classical chaotic transport in a semiclassical regime or are purely quantum in nature. A paradigmatic and realistic class of model systems which has been studied most extensively, both theoretically and experimentally, consists of the periodically kicked rotor and variants of it [1–14]. These systems feature some of the most well-known phenomena in the field of quantum chaos, such as dynamical localization [1], i.e., the quantum suppression of classical chaotic diffusion, and the diametrically opposite phenomenon of *quantum resonance* (QR) [2]. The latter is a purely quantum quadratic growth of the mean kinetic energy in time occurring for special values of an effective Planck constant. The experimental realization of the kicked rotor using atom-optics techniques [3] has led to breakthroughs in the study of quantum chaos. Such experiments actually realize the kicked particle, not the kicked rotor, since atoms move on lines and not on circles like a rotor. However, the two systems can be exactly related due to the conservation of the particle *quasimomentum*  $\beta$  [6,8] (see also below).

An important concept introduced recently in classical and quantum Hamiltonian transport is that of a “ratchet.” This is a spatially periodic system in which, without a biased force, a directed current of particles can be established. Ratchet models were originally proposed as mechanisms for some kinds of biological motors and as nanoscale devices for several applications [15]. In these contexts, the directed current is due to a spatial/temporal asymmetry combined with noise and dissipation. Ratchets based on classical physics have been implemented recently [16]. In a classical Hamiltonian system, dissipation is absent and noise is replaced by deterministic chaos. Here, a directed current of particles in the chaotic sea may arise under asymmetry conditions for a mixed phase space [17]. The

corresponding quantized system may exhibit a significant ratchet behavior even in a fully chaotic regime [10,11,18]. Such a behavior, which occurs in a variant of the kicked rotor and can be related to the underlying classical dynamics, was observed recently in experiments using ultracold atoms [11]. Under *exact* QR conditions, theory predicts a purely quantum ratchet *acceleration*, i.e., a linear increase of the directed current (the mean momentum) in time [12,13]. An experimental observation of this phenomenon on a short time interval was reported quite recently for the usual kicked rotor [14], with  $\beta = 0$ . It is known, however, that the unavoidable experimental uncertainty in  $\beta$  strongly affects QR [6–8], and it is therefore natural to ask how it will affect the QR-ratchet acceleration.

In this Letter, we present an experimental realization of quantum ratchets associated with QR of the kicked particle for *arbitrary* values of the quasimomentum  $\beta$ . The experiments are conducted by exposing a Bose-Einstein condensate (BEC) to a pulsed optical standing wave which creates a potential  $V(x) = V_{\max} \cos(Gx - \gamma)$ . Here,  $x$  is the spatial coordinate along the standing wave,  $G = 4\pi/\lambda$  is the “grating vector,”  $\lambda$  is the light wavelength, and  $\gamma$  is an “offset” phase. The BEC is prepared in an initial state  $\psi_0(x)$  with  $|\psi_0(x)| \propto |\cos(Gx/2)|$ , different from the pure momentum state normally used in quantum-chaos experiments [3–5,7,9,11]. Our experimental results agree well with a very recent general theory of QR ratchets [13], after including in this theory the effect of the finite quasimomentum width  $\Delta\beta$  of the BEC. This width is shown to cause a *suppression* of the QR-ratchet acceleration for exactly “resonant”  $\beta$  [13], leading to a saturation of the directed current. Unlike other kinds of quantum ratchets [10,11,17,18], the QR ratchet exhibits fully *symmetric* features; both  $V(x)$  and  $\psi_0(x)$  have a point symmetry around some center. The directed current for general  $\beta$  depends strongly on the relative displacement between the two symmetry centers, here given by  $\gamma$ . Figure 1 shows the resonant current after 5 standing-wave pulses versus  $\gamma$ . Note that the current direction can be easily controlled

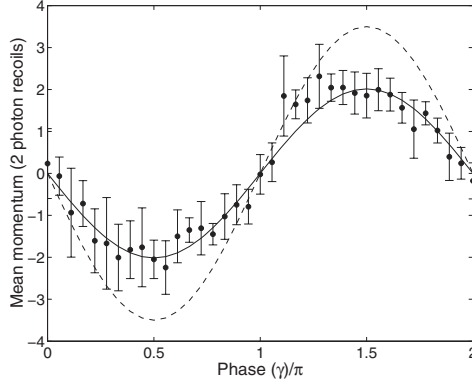


FIG. 1. Mean momentum vs phase angle  $\gamma$  for kicking strength  $k = 1.4$ , kick number  $t = 5$ , and resonant quasimomentum  $\beta = 0.5$ . The filled circles and associated error bars are from the experiment. The solid line corresponds to the theory (3) for a BEC with width  $\Delta\beta = 0.056$ . The dashed line corresponds to the ideal ( $\Delta\beta = 0$ ) theory (1).

by  $\gamma$  and that the current vanishes for  $\gamma = 0$  (coinciding symmetry centers).

We start by summarizing the basic theory (see more details in Refs. [6,8,13]). Using dimensionless quantities, the quantum kicked particle is described by the general Hamiltonian  $\hat{H} = \hat{p}^2/2 + kV(\hat{x})\sum_t \delta(t' - t\tau)$ , where  $(\hat{p}, \hat{x})$  are momentum and position operators,  $k$  is the kicking strength,  $V(x)$  is an arbitrary periodic potential,  $\tau$  is the kicking period, and  $t'$  and  $t$  are the continuous and “integer” times. The units are chosen so that the particle mass is 1,  $\hbar = 1$ , and the period of  $V(x)$  is  $2\pi$ . The translational invariance of  $\hat{H}$  in  $\hat{x}$  implies the conservation of the quasimomentum  $\beta$ ,  $0 \leq \beta < 1$ , in the time evolution of a Bloch wave packet  $\exp(i\beta x)\psi(x)$ . Here,  $\psi(x)$  is a  $2\pi$ -periodic function, so that one can consider  $x$  as an angle  $\theta$ . Introducing the corresponding angular-momentum operator  $\hat{N} = -id/d\theta$ , the time evolution of  $\psi(\theta)$  in one period  $\tau$  is given by  $\hat{U}_\beta\psi(\theta)$ , where  $\hat{U}_\beta = \exp[-ikV(\hat{\theta})]\exp[-i\tau(\hat{N} + \beta)^2/2]$ . The latter operator describes a “ $\beta$ -kicked rotor” which is related to the kicked particle at fixed  $\beta$  by  $\hat{p} = \hat{N} + \beta$ ; i.e.,  $\beta$  is the “fractional” part of the particle momentum. QR of a  $\beta$ -kicked rotor is a quadratic growth of the mean kinetic energy at sufficiently large times  $t$ :  $\langle\psi_t|\hat{N}^2/2|\psi_t\rangle \sim Dt^2$ , where  $\psi_t(\theta) = \hat{U}_\beta^t\psi_0(\theta)$  is an evolving wave packet and  $D$  is some coefficient. This behavior will generally occur provided two conditions are satisfied [8]: (a) The effective Planck constant  $\tau/(2\pi)$  is a rational number  $l_0/q_0$ , where  $(l_0, q_0)$  are coprime integers; (b)  $\beta$  is also a rational number  $\beta_r$  characterized by two integers  $(r, g)$  defined as follows:  $g$  is the smallest integer such that  $r = (\beta_r + gq_0/2)gl_0$  is

integer. Then, the resonant quasimomentum  $\beta = \beta_r$  can be written as  $\beta = \beta_{r,g}$ .

We shall focus on the case of integer  $\tau/(2\pi) = l_0$  ( $q_0 = 1$ ), corresponding to the “main” QRs. In this case, the time evolution of wave packets  $\psi_t(\theta)$  under  $\hat{U}_\beta$  can be exactly calculated for arbitrary potential  $V(\theta) = \sum_m V_m \exp(-im\theta)$  and for any  $\beta$  [8]. One can then evaluate the current  $\langle\hat{p}\rangle_t$ , i.e., the mean momentum of the evolving Bloch wave. Using  $\langle\hat{p}\rangle_t = \langle\hat{N}\rangle_t + \beta$ , where  $\langle\hat{N}\rangle_t = \langle\psi_t|\hat{N}|\psi_t\rangle$ , the change in the current relative to its initial value is given by  $\Delta\langle\hat{p}\rangle_t = \langle\hat{N}\rangle_t - \langle\hat{N}\rangle_0$ . This change is a measure of the ratchet effect induced by the kicking. Exact results for  $\Delta\langle\hat{p}\rangle_t$  can be derived for general  $\psi_0(\theta)$  [13], but we shall restrict ourselves here to the simplest initial wave packet giving ratchet effects:  $\psi_0(\theta) = [1 + \exp(-i\theta)]/\sqrt{4\pi}$ . The arbitrary potential  $V(\theta)$  can be written, up to a real factor, as  $V(\theta) = \cos(\theta - \gamma) + V_2(\theta)$ , where  $V_2(\theta)$  contains only harmonics of order  $m \geq 2$ . Then, by applying the general exact result (17) in Ref. [13] to our system (corresponding to  $w = 0$  and  $T = 1$  in [13]), we find for the initial wave packet above that

$$\Delta\langle\hat{p}\rangle_t = \frac{k \sin(\tau_\beta t/2)}{2 \sin(\tau_\beta/2)} \sin[(t+1)\tau_\beta/2 - \gamma], \quad (1)$$

where  $\tau_\beta = \pi l_0(2\beta + 1)$ . Because of the simple choice of  $\psi_0(\theta)$ , this result is completely independent of  $V_2(\theta)$ . Thus, without loss of generality, henceforth we take  $V(\theta) = \cos(\theta - \gamma)$ . The denominator in (1) vanishes if  $\tau_\beta = 2\pi r$  for some integer  $r$ . This corresponds precisely to a resonant value of  $\beta = \beta_{r,g} = r/l_0 - 1/2 \bmod(1)$ , with  $g = 1$ . For  $\beta = \beta_{r,1}$ , Eq. (1) reduces to a linear growth in time  $t$ , a ratchet acceleration:  $\Delta\langle\hat{p}\rangle_{t,r} = -(k/2)\sin(\gamma)t$ .

In an experimental realization of QR ratchets using a kicked BEC, the small but finite initial momentum width of the BEC can be important. Here, we consider a mixture of quasimomenta  $\beta'$ , having a Gaussian distribution with average  $\beta$  and standard deviation  $\Delta\beta$ :  $\Gamma_{\beta,\Delta\beta}(\beta') = (\Delta\beta\sqrt{2\pi})^{-1} \exp\{-(\beta' - \beta)^2/[2(\Delta\beta)^2]\}$ . For small  $\Delta\beta$ , this is a good approximation of the actual initial momentum distribution [19]. The average of (1) over  $\beta = \beta'$  with distribution  $\Gamma_{\beta,\Delta\beta}(\beta')$  can be exactly calculated:

$$\langle\Delta\langle\hat{p}\rangle_t\rangle_{\Delta\beta} = \frac{k}{2} \sum_{s=1}^t \sin(\tau_\beta s - \gamma) \exp[-2(\pi l_0 \Delta\beta s)^2]. \quad (2)$$

Unlike (1), the expression (2) tends to a well-defined finite value as  $t \rightarrow \infty$ , for all  $\beta$ . In particular, for resonant  $\beta = \beta_{r,1}$  with  $\tau_\beta = 2\pi r$ , Eq. (2) reduces to

$$\langle\Delta\langle\hat{p}\rangle_t\rangle_{r,\Delta\beta} = -\frac{k}{2} \sin(\gamma) \sum_{s=1}^t \exp[-2(\pi l_0 \Delta\beta s)^2]. \quad (3)$$

The result (3) implies a suppression of the ratchet acceleration above, which is recovered as  $\Delta\beta \rightarrow 0$ . In practice,

for sufficiently small  $\Delta\beta$ , the value of  $\langle\Delta\langle\hat{p}\rangle_t\rangle_{\Delta\beta}$  for  $\beta$  close to  $\beta_{r,1}$  is much larger than that for generic  $\beta$ , except when  $|\sin(\gamma)|$  is very small.

It should be noted that both the potential  $V(\theta) = \cos(\theta - \gamma)$  and the initial wave packet  $\psi_0(\theta) = [1 + \exp(-i\theta)]/\sqrt{4\pi}$  have a point symmetry:  $V(2\gamma - \theta) = V(\theta)$  (inversion around  $\theta = \gamma$ ) and  $\psi_0^*(-\theta) = \psi_0(\theta)$  (inversion around  $\theta = 0$  accompanied by time reversal). The results (1)–(3) depend on the relative displacement  $\gamma$  between the symmetry centers of  $V(\theta)$  and  $\psi_0(\theta)$ . For  $\gamma = 0$ , the system is “symmetric” and there is no resonant ratchet effect,  $\langle\Delta\langle\hat{p}\rangle_t\rangle_{r,\Delta\beta} = 0$ . At fixed  $k$ ,  $|\langle\Delta\langle\hat{p}\rangle_t\rangle_{r,\Delta\beta}|$  is largest for  $\gamma = \pm\pi/2$ , values of  $\gamma$  which may be viewed as corresponding to “maximal asymmetry” situations. The direction of the change (3) in the current is given by the sign of  $-\sin(\gamma)$ . We shall henceforth use  $l_0 = 1$ , corresponding to the “half-Talbot time” so that the only resonant value of  $\beta$  is  $\beta = 0.5$ . It is easy to see that  $\langle\hat{p}\rangle_0 = \langle\hat{N}\rangle_0 + \beta = 0$  for  $\beta = 0.5$  and then  $\Delta\langle\hat{p}\rangle_t = \langle\hat{p}\rangle_t$ .

Our experiments were carried out using the all-optical BEC apparatus described in Ref. [5]. After creating a BEC of  $\sim 50\,000$   $^{87}\text{Rb}$  atoms in a focused  $\text{CO}_2$  laser beam, we applied a series of optical standing-wave pulses from a diode laser beam (6.8 GHz red detuned from the 780 nm laser cooling transition) propagating at  $52^\circ$  to the vertical. Through an ac-Stark shift, the standing wave changed the energy of the atoms by an amount proportional to the light intensity. The resulting spatially periodic phase modulation of the BEC wave function acted as a phase grating. Each of the two counterpropagating laser beams which comprised the standing wave passed through an acousto-optic modulator (AOM) driven by an arbitrary waveform generator. This enabled us to control the frequency and phase of each of the beams. Adding two counterpropagating waves differing in frequency by  $\Delta f$  results essentially in a standing wave that moves with a velocity  $v = 2\pi\Delta f/G$ , where  $G$  is the grating vector. The initial momentum or quasimomentum  $\beta$  of the BEC relative to the standing wave is proportional to  $v$ . Thus, by varying  $\Delta f$ , we could set arbitrarily the value of  $\beta$  and also compensate for the effect of the gravitational acceleration along the standing wave (the experiments were done in a free-falling frame).

In order to prepare the initial state, the first standing-wave pulse was relatively long, having a duration of  $38\ \mu\text{s}$ . This pulse Bragg diffracted the atoms into a superposition of two plane waves [20]:  $|\psi_0\rangle = [|P=0\rangle + |P=\hbar G\rangle]/\sqrt{4\pi}$ , where  $P$  is the nonscaled momentum. The second and subsequent pulses of the standing wave were short enough to be in the Raman-Nath regime. These pulses diffracted the atoms into a wide spread of momentum states and enabled the realization of a kicked-rotor system. The value of the kicking strength  $k$  was measured by subjecting the BEC to one kick and comparing the populations of various diffraction orders; we used  $k \sim 1.4$ . By varying the phase of the RF waveforms driving the AOMs,

we were able to shift the position of the standing wave for the kicked rotor relative to the standing wave used in the Bragg-state preparation. This is the phase  $\gamma$  in Eqs. (1)–(3). Finally, in order to probe the momentum distribution, we waited 8 ms and then imaged the atoms in absorption. Measurements of the initial momentum width of the BEC using a time-of-flight technique gave an upper bound to  $\Delta\beta$  of 0.1. The slow expansion of the BEC and the finite resolution of our imaging system made it difficult to measure this quantity more precisely.

We have performed a comprehensive experimental study of the mean momentum of the BEC as function of several variables. Error bars for all the data were accurately determined by repeated measurements of the mean momentum at fixed values of the parameters. The results are presented in Figs. 1–3 and are compared with the theory above. These figures show the dependence of the mean momentum on the phase  $\gamma$  for  $t = 5$  and resonant  $\beta = 0.5$  (Fig. 1), its dependence on  $t$  for  $\gamma = \pi/2$  and  $\beta = 0.5$  (Fig. 2), and the dependence of the mean-momentum change on  $\beta$  for  $t = 5$  and  $\gamma = \pm\pi/2$  (Fig. 3). The solid line in the figures corresponds to Eq. (2) or Eq. (3). The dashed line in Figs. 1 and 3 corresponds to the nonaveraged theory (1). We can see that the experimentally determined mean momentum in all the figures is well fitted by the theory (2) or (3) for the same value of the width  $\Delta\beta$ ,  $\Delta\beta = 0.056$ . This value of  $\Delta\beta$  is also consistent with what can be measured directly using time-of-flight. These facts indicate good agreement of the experimental results with the QR-ratchet theory above. Thus, the clear saturation of the mean momentum in Fig. 2 provides experimental evidence for the suppression of the resonant ratchet acceleration. The

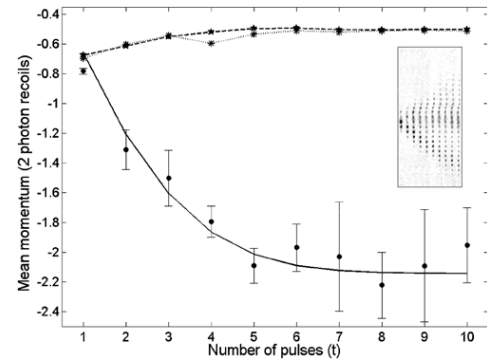


FIG. 2. Mean momentum vs kick number  $t$  for  $k = 1.4$ ,  $\gamma = \pi/2$ , and  $\beta = 0.5$ . The filled circles and error bars are experimental data, and the solid line corresponds to Eq. (3) ( $\Delta\beta = 0.056$ ). The dashed and dotted lines are the classical mean momentum  $\langle p_t \rangle$  with average taken over two different initial ensembles in phase space (see text for more details). The inset shows the time-of-flight images of the BEC vs  $t$ .



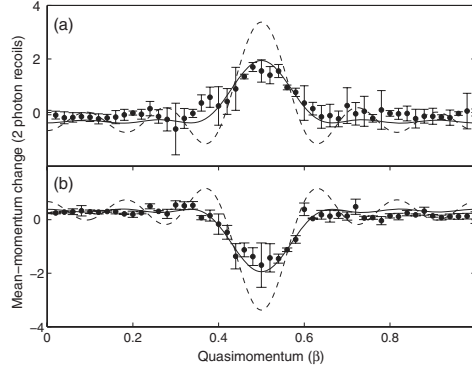


FIG. 3. Mean-momentum change after  $t = 5$  kicks vs  $\beta$  for  $k = 1.4$  and (a)  $\gamma = -\pi/2$ , (b)  $\gamma = \pi/2$ . The filled circles and error bars are experimental data; the dashed and solid lines correspond, respectively, to Eqs. (1) and (2) ( $\Delta\beta = 0.056$ ).

inset in Fig. 2 plots the time-of-flight images of the kicked BEC as time increases. Note that the distribution of the momentum states is not symmetric and is weighted towards the negative diffraction orders, as expected from the mean-momentum values.

It is instructive to compare the behavior of the quantum mean momentum in Fig. 2 with that of its closest classical analogue. This is  $\langle p_t \rangle$ , where  $p_t$  is the classical momentum at time  $t$ , given by a standard map, and  $\langle \rangle$  denotes average over an ensemble of initial conditions ( $p_0, x_0$ ) whose distribution in phase space is the same as that featured by the quantum averages in (3). Thus, the distribution function of  $x_0$  is  $\phi(x_0) = \cos^2(x_0/2)/\pi$ , equal to the probability density  $|\psi_0(x)|^2$  for the initial wave packet;  $p_0$  is distributed like  $\langle \hat{p} \rangle_0 = \langle \hat{N} \rangle_0 + \beta'$ , where  $\langle \hat{N} \rangle_0 = -0.5$  and the distribution of  $\beta'$  around  $\beta = 0.5$  is the Gaussian  $\Gamma_{\beta, \Delta\beta}(\beta')$  above with  $\Delta\beta = 0.056$ . One has  $\langle p_0 \rangle = \langle \langle \hat{p} \rangle_0 \rangle_{r, \Delta\beta} = 0$ . The results for  $\langle p_t \rangle$  are plotted in Fig. 2 (dashed line), showing a saturation to a value clearly *different* from the quantum one. In fact, this classical saturation is *not* due to averaging over  $p_0$  or  $\beta'$ , as in the quantum case, but to the relaxation of the initial nonuniform distribution  $\phi(x_0)$  to an almost uniform one in phase space, which is fully chaotic for  $k = 1.4$ . The transient nonuniformity during the relaxation process causes  $\langle p_t \rangle$  to acquire its nonzero saturated value. To show explicitly that the average over  $p_0$  is classically not essential, we plot in Fig. 2 also  $\langle p_t \rangle$  with the average taken over an ensemble with constant  $p_0 = 0$  and with  $x_0$  distributed as above (dotted line). We see that  $\langle p_t \rangle$  saturates to the same value. All this demonstrates that the experimental results in Fig. 2, as well as those in Figs. 1 and 3, reflect *purely* quantum phenomena for a nonsmall value of the effective Planck constant,  $\tau/(2\pi) = 1$ .

In conclusion, we have experimentally realized QR ratchets for arbitrary quasimomentum  $\beta$ . These purely quantum ratchets are unique in their strong dependence on a *conserved* quantum entity ( $\beta$ , see Fig. 3) and in their fully *symmetric* features on which they also depend strongly through the phase  $\gamma$  (Fig. 1). The consideration of general  $\beta$  is necessary to account for the finite width  $\Delta\beta$  of the BEC. We have shown that this width is the main reason for the suppression of the resonant ratchet acceleration, a distinctive feature of ideal QR ratchets [12,13]. A fingerprint of this acceleration for finite  $\Delta\beta$  is the pronounced ratchet effect around resonant  $\beta$  (Fig. 3). To increase further the resonant directed current,  $\Delta\beta$  has to be decreased below the value used in this work. We hope to achieve this in the future by improving our present experimental setup.

I.D. was partially supported by the Israel Science Foundation (Grant No. 118/05).

- [1] *Quantum Chaos, Between Order and Disorder*, edited by G. Casati and B. Chirikov (Cambridge University Press, Cambridge, 1995), and references therein.
- [2] F.M. Izrailev, Phys. Rep. **196**, 299 (1990), and references therein.
- [3] F.L. Moore *et al.*, Phys. Rev. Lett. **73**, 2974 (1994).
- [4] R.M. Godun *et al.*, Phys. Rev. A **62**, 013411 (2000); S. Schlunk *et al.*, Phys. Rev. Lett. **90**, 054101 (2003); Z.-Y. Ma *et al.*, Phys. Rev. Lett. **93**, 164101 (2004).
- [5] G. Behinaein *et al.*, Phys. Rev. Lett. **97**, 244101 (2006).
- [6] S. Wimberger, I. Guarneri, and S. Fishman, Nonlinearity **16**, 1381 (2003).
- [7] M.B. d'Arcy *et al.*, Phys. Rev. E **69**, 027201 (2004).
- [8] I. Dana and D.L. Dorofeev, Phys. Rev. E **73**, 026206 (2006); **74**, 045201(R) (2006).
- [9] C. Ryu *et al.*, Phys. Rev. Lett. **96**, 160403 (2006).
- [10] G.G. Carlo *et al.*, Phys. Rev. A **74**, 033617 (2006).
- [11] P.H. Jones *et al.*, Phys. Rev. Lett. **98**, 073002 (2007).
- [12] E. Lundh and M. Wallin, Phys. Rev. Lett. **94**, 110603 (2005).
- [13] I. Dana and V. Roitberg, Phys. Rev. E **76**, 015201(R) (2007). This Letter considers the kicked particle in the presence of gravity, characterized by coprime integers  $(w, T)$ ; the special case of zero gravity, treated in this Letter, corresponds to  $w = 0$  and  $T = 1$ .
- [14] M. Sadgrove *et al.*, Phys. Rev. Lett. **99**, 043002 (2007).
- [15] P. Reimann, Phys. Rep. **361**, 57 (2002); R.D. Astumian and P. Hänggi, Phys. Today **55**, No. 11, 33 (2002).
- [16] C. Robilliard, D. Lucas, and G. Grynberg, Appl. Phys. A **75**, 213 (2002); M. Schiavoni *et al.*, Phys. Rev. Lett. **90**, 094101 (2003); R. Gommers, M. Brown, and F. Renzoni, Phys. Rev. A **75**, 053406 (2007).
- [17] H. Schanz, T. Dittrich, and R. Ketzmerick, Phys. Rev. E **71**, 026228 (2005).
- [18] J. Gong and P. Brumer, Phys. Rev. Lett. **97**, 240602 (2006).
- [19] K.B. Davis *et al.*, Phys. Rev. Lett. **75**, 3969 (1995).
- [20] M. Kozuma *et al.*, Phys. Rev. Lett. **82**, 871 (1999).

Sub-Fourier Characteristics of a  $\delta$ -kicked-rotor Resonance

I. Talukdar, R. Shrestha, and G. S. Summy

*Department of Physics, Oklahoma State University, Stillwater, Oklahoma 74078-3072, USA*  
(Received 7 April 2010; revised manuscript received 25 May 2010; published 28 July 2010)

We experimentally investigate the sub-Fourier behavior of a  $\delta$ -kicked-rotor resonance by performing a measurement of the fidelity or overlap of a Bose-Einstein condensate exposed to a periodically pulsed standing wave. The temporal width of the fidelity resonance peak centered at the Talbot time and zero initial momentum exhibits an inverse cube pulse number ( $1/N^3$ )-dependent scaling compared to a  $1/N^2$  dependence for the mean energy width at the same resonance. A theoretical analysis shows that for an accelerating potential the width of the resonance in acceleration space depends on  $1/N^3$ , a property which we also verify experimentally. Such a sub-Fourier effect could be useful for high precision gravity measurements.

DOI: 10.1103/PhysRevLett.105.054103

PACS numbers: 05.45.Mt, 05.60.Gg, 06.30.Gv, 37.10.Vz

The quantum  $\delta$ -kicked-rotor (QDKR) has proved to be an excellent testing ground for theoretical and experimental studies of chaos in the quantum domain [1]. An experimental version of this system in the form of the kicked particle is achieved by exposing cold atoms to  $N$  pulses of an off-resonant standing wave of light [1,2]. Ever since its realization, the QDKR has revealed a rich variety of effects including dynamical localization [3], quantum accelerator modes [4,5], quantum ratchets [6,7], and quantum resonances [2,8,9]. Such resonances appear for pulses separated by rational fractions of a characteristic time called the Talbot time and can be observed as sharp peaks in the mean energy of the system [10]. The width of these peaks has been found to scale as  $1/N^2$ , a sub-Fourier effect attributed to the nonlinear nature of the QDKR and explained using a semiclassical picture [11]. Away from the resonances, dynamical localization sets in, characterized by the quantum suppression of classical momentum diffusion beyond a “quantum break time” [3]. This property, unique to quantum dynamics in the chaotic regime, was utilized to discriminate between two driving frequencies of the QDKR with sub-Fourier resolution [12].

High-precision measurements using quantum-mechanical principles have been carried with atom interferometers for many years [13]. Such devices were used to determine the Earth’s gravitational acceleration [14], fine structure constant  $\alpha$  [15], and the Newtonian constant of gravity [16]. The promise of the QDKR as a candidate for making these challenging measurements has begun to be realized [17]. Recently a scheme was proposed for measuring the overlap or fidelity between a near-resonant  $\delta$ -kicked-rotor state and a resonant state via application of a tailored pulse at the end of a rotor pulse sequence [18]. It predicted a  $1/N^3$  scaling of the temporal width of the fidelity peak. In this paper we report on the observation of such fidelity resonance peaks and their sub-Fourier nature. Figure 1 illustrates a plot of the fidelity (fraction of atoms in the zeroth order momentum state) vs pulse period obtained by the application of an overlap pulse at

the end of five rotor kicks. For comparison, we also plot the mean energy of the rotor sequence. It can be seen that even for relatively few kicks the fidelity peak is significantly narrower. We also investigated the sensitivity of this fidelity resonance to an accelerating rotor. As will be seen, our calculations indicate that the width of the fidelity peak vs acceleration decreases at a sub-Fourier rate of  $1/N^3$ . We confirm this result with experiments.

The dynamics of a periodically kicked atom in the presence of a linear potential is described by the quantum  $\delta$ -kicked accelerator (QDKA) Hamiltonian

$$\hat{H} = \frac{\hat{p}^2}{2} + \frac{\eta}{\tau} \hat{X} + \phi_d \cos(\hat{X}) \sum_{i=1}^N \delta(t' - i\tau). \quad (1)$$

$\hat{p}$  is the momentum (in units of two photon recoils,  $\hbar G$ ) that an atom of mass  $M$  acquires from short, periodic

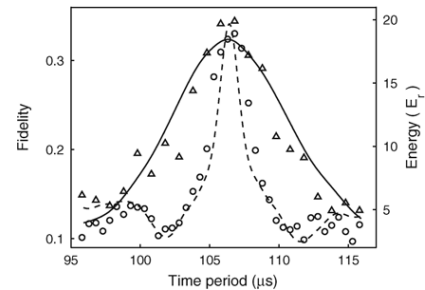


FIG. 1. Experimentally measured fidelity distribution (circles) due to five kicks of strength  $\phi_d = 0.8$  followed by a  $\pi$  phase shifted kick of strength  $5\phi_d$ . The mean energy (triangles) of the same five kick rotor is shown for comparison. Numerical simulations of the experiment for a condensate with momentum width  $0.06\hbar G$  are also plotted for fidelity (dashed line) and mean energy (solid line). The amplitude and offset of the simulated fidelity were adjusted to account for the experimentally imperfect reversal phase.

pulses of a standing wave with a grating vector  $G = 2\pi/\lambda_G$  ( $\lambda_G$  is the wavelength of the standing wave).  $\hat{X}$  is position in units of  $G^{-1}$  and  $\eta = Mg'T/\hbar G$ ,  $g'$  being its acceleration between pulses separated by  $T$ , the pulse period.  $\phi_d = \Omega^2 \Delta t / 8\delta_L$  represents the kicking strength of a pulse of length  $\Delta t$ ,  $\Omega$  is the Rabi frequency, and  $\delta_L$  the detuning of the kicking laser from the atomic transition.  $t'$  is the continuous time variable and  $\tau = 2\pi T/T_{1/2}$  is the scaled pulse period.

For the case  $\eta = 0$ , Eq. (1) reduces to the usual QDKR Hamiltonian [2]. For now we restrict ourselves to this situation. Primary quantum resonances are seen for pulses separated by integer multiples of the half-Talbot time,  $T_{1/2} = 2\pi M/\hbar G^2$  or  $\tau = 2\pi$ . Adjacent momentum orders evolve phases which are integer multiples of  $2\pi$  during this time period resulting in a quadratic growth in the rotor mean energy,  $\langle E \rangle = 2E_r \phi_d^2 N^2$ , where  $E_r = \hbar^2 G^2 / 8M$  is the photon recoil energy. The width of the mean energy around the resonance time was found to decrease as  $1/(N^2 \phi_d)$  [9,11].

In order to demonstrate the role of the relative phase deviations of the contributing momentum states near such a resonance, a “fidelity” test for the QDKR was proposed in Ref. [18]. In this scheme, a kick changed in phase by  $\pi$  and carrying a strength of  $N\phi_d$  is applied at the end of the  $N$  rotor kicks. The fidelity is then defined as  $F = |\langle \beta | U_r U^N | \beta \rangle|^2$  where  $U = \exp(-i\frac{\tau}{2}\hat{p}^2) \times \exp[-i\phi_d \cos(\hat{X})]$  describes the one period evolution,  $U_r = \exp[iN\phi_d \cos(\hat{X})]$  is the overlap pulse, and  $\beta$  is the fractional part of the momentum.  $F$  therefore gives the probability of the revival of the initial state and is measured by the fraction of atoms which have returned to the initial zero momentum state. Using a perturbative treatment, it was shown that near the resonance at the Talbot time,  $\tau = 4\pi$ , the fidelity is [18]

$$F(\epsilon, \beta = 0) \simeq J_0^2\left(\frac{1}{12}N^3\phi_d^2\epsilon\right), \quad (2)$$

where  $\epsilon = \tau - 4\pi$ . The width of such a peak in  $\epsilon$  therefore changes to  $1/(N^3\phi_d^2)$ , displaying a stronger sub-Fourier dependence on the number of kicks than the mean energy.

Our experiment is performed by producing a Bose-Einstein condensate of 20 000 Rb87 atoms in the  $5S_{1/2}$ ,  $F = 1$ ,  $m_F = 0$  level in an optical trap [5,19]. After being released from the trap, the condensate is exposed to a horizontal standing wave created by two beams of wavelength  $\lambda = 780$  nm light detuned 6.8 GHz to the red of the atomic transition. The wave vector of each beam was aligned  $\theta = 52^\circ$  to the vertical. This created a horizontal standing wave with a wavelength of  $\lambda_G = \lambda/2 \sin\theta$  and a corresponding Talbot time of 106.5  $\mu$ s. Two acousto-optic modulators controlled the pulse lengths as well as the relative frequencies of the kicking beams enabling the control of the acceleration and initial momentum of the standing wave with respect to the condensate. The kicking

pulse length was  $\Delta t = 0.8 \mu$ s with a  $\phi_d \approx 0.6$ . For the last kick the phase of one of the acousto-optic modulators rf driving signal was changed by  $\pi$  which shifted the standing wave by half a wavelength. In order to keep this final overlap pulse within the Raman-Nath regime we varied the intensity rather than the pulse length to create a kick strength of  $N\phi_d$ . This was done by adjusting the amplitudes of the rf waveforms driving the kicking pulse. Dephasing primarily due to vibrations made the reversal process inconsistent for  $N > 6$  [20]. To reduce this, the standing wave at each kick was shifted by half a wavelength with respect to the previous kick. That is, the summation in Eq. (1) becomes  $\sum_{t'=1}^N (-1)^{t'-1} \delta(t' - t\tau)$ . This had the effect of shifting the Talbot time resonance to  $T_{1/2}$ . Consequently the reduced experimental time led to much improved results. Following the entire kicking sequence we waited 8 ms for the different momentum orders to separate before the atoms were absorption imaged.

From the time-of-flight images fidelity  $F$  is measured as the fraction of atoms which have reverted back to the zeroth order momentum state, that is  $F = P_0/\sum_n P_n$  where  $P_n$  is the number of atoms in the  $n$ th momentum order. To facilitate the analysis of the data, all of the resonance widths ( $\delta\epsilon$ ) were scaled to a reference kick number of  $N = 4$ . That is, we define a scaled fidelity width  $\Delta\epsilon = \delta\epsilon/\delta\epsilon_{N=4}$  for each scaled kick number  $N_s = N/4$  and recover  $\log\Delta\epsilon = -3 \log N_s$  using Eq. (2). For each kick, a scan is performed around the resonance time. To ensure the best possible fit of the central peak of the fidelity spectrum to a Gaussian, the time is scanned between values which make the argument of  $J_0^2$  of Eq. (2)  $\approx 2.4$  so that the first side lobes are only just beginning to appear. Figure 2(a) plots the logarithm of the FWHM for four to nine kicks scaled to the fourth kick. A linear fit to the data gives a slope of  $-2.73 \pm 0.19$  giving a reasonable agreement with the predicted value of  $-3$  within the experimental error. As seen in the same figure, the results are close to the numerical simulations which take into account the finite width of the initial state of  $0.06\hbar G$  [7]. We also compared the resonance widths of the kicked-rotor mean energy  $\langle E \rangle$  to that of the fidelity widths. As in the fidelity, the plotted values  $\Delta\langle E \rangle$  have been normalized to that of the fourth kick. On the log scale, the width of each peak gets narrower with the kick number with a slope of  $-1.93 \pm 0.21$  [Fig. 2(a)] in agreement with previous results [9,21]. As a further test of Eq. (2), the variation in the widths of the fidelity and mean energy peaks were studied as a function of  $\phi_d$ . Figure 2(b) shows the fidelity width changing with a slope of  $-1.96 \pm 0.3$ , close to the predicted value of  $-2$ . This again scales faster than the mean energy width which decreases with a slope of  $-0.88 \pm 0.24$  (the theoretical value being  $-1$ ).

The resonances studied here appear for pulses separated by the Talbot time and an initial momentum state of  $\beta = 0$ .



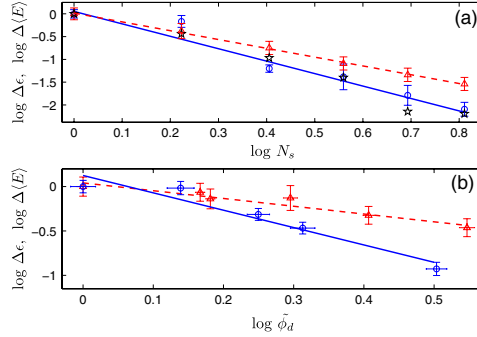


FIG. 2 (color online). Experimentally measured fidelity (circles) and mean energy (triangles) widths (FWHM) as a function of (a) the number of pulses, and (b) the kicking strength  $\phi_d$  scaled to  $\phi_d$  of the first data point. In (a), the data are for four to nine kicks in units normalized to the fourth kick. Error bars in (a) are over three sets of experiments and in (b)  $1\sigma$  of a Gaussian fit to the distributions. Dashed lines are linear fits to the data. Stars are numerical simulations for an initial state with a momentum width of  $0.06\hbar G$ .

Away from this resonant  $\beta$ , phase changes in the amplitudes of the different momentum orders lead to a fidelity which depends on the initial momentum as  $F(\epsilon = 0, \beta) = J_0^2[2\pi\phi_d N(N+1)\beta]$  [18]. The peak width in  $\beta$  space is thus expected to change as  $1/[N(N+1)]$  around  $\beta = 0$ , as against a  $1/N$  scaling of the mean energy width [9]. To verify this, the initial momentum of the condensate with respect to the standing wave was varied and the kicking sequence applied. The experimentally measured widths  $\Delta\beta = \delta\beta/\delta\beta_{N=4}$  in Fig. 3(a) display a scaling of  $\Delta\beta \propto [N(N+1)]^{-0.92}$  close to the theoretical value.

For an initial state  $|\beta + n\rangle$ , the wave function acquires a nonzero phase during the free evolution even at the Talbot time. Therefore the final kick performs a velocity selective reversal, preferentially bringing back atoms closer to an initial momentum of  $\beta = 0$ . This is similar to the time-reversed Loschmidt cooling process proposed in Refs. [22,23], although in that technique a forward and reverse path situated on either side of the resonant time was used in order to benefit from the chaotic dynamics. To observe this effect, the current scheme offers an experimental advantage in terms of stability due to the reduced length of the pulse sequence. Here, only a single pulse performs the velocity selection at the end, whereas in the Loschmidt technique  $N$  phase reversed kicks separated by a finite time are used. Figure 4 demonstrates the reduction of the momentum distribution width. Accompanying this decrease is a drop in the peak height. Our simulations and the results of Ref. [23] predict that for the case of a non-interacting condensate, this should remain constant. In addition to interactions, we expect experimental imper-

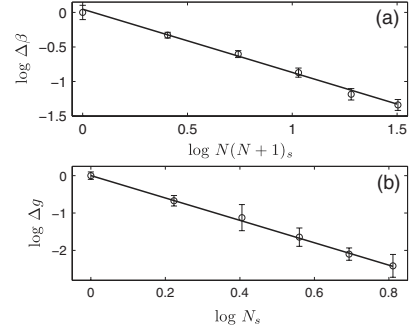


FIG. 3. (a) Variation of the fidelity peak width around  $\beta = 0$  as a function of kick number  $N(N+1)_s = N(N+1)/20$  scaled to the fourth kick. The straight line is a linear fit to the data with a slope of  $-0.92 \pm 0.06$ . Error bars as in Fig. 2(b). (b) Dependence of the acceleration resonance peak width on  $N$  in units scaled to the fourth kick. Error bars are over three sets of experiments.

fections in the fidelity sequence to play a role in the smaller peak densities with increasing kick numbers. We performed the same experiment 4.5 ms after the Bose-Einstein condensate was released from the trap when the mean field energy had mostly been transformed to kinetic energy in the expanding condensate. A similar reduction in the momentum width of the reversed state, along with a decrease in the peak density, was observed.

We now investigate the behavior of fidelity in the presence of acceleration, i.e.  $\eta \neq 0$ . The state of the QDKA Eq. (1) after  $N$  kicks is  $|\psi(N\tau)\rangle = \sum_n c_n |n + \beta\rangle$  where  $n$  is the integer part of momentum  $\hat{P}$ . The expansion coefficients  $c_n$  are  $c_n(\epsilon, \beta, \eta) = \langle n + \beta | \hat{U}_{g_N} \cdots \hat{U}_{g_2} \hat{U}_{g_1} | \beta \rangle$ .  $\hat{U}_{g_i} = \exp[-i\frac{\tau}{2}(\hat{p} + t\eta + \frac{\eta}{2})^2] \exp[-i\phi_d \cos(\hat{X})]$  is the  $i$ th kick evolution operator in the freely falling frame obtained after a gauge transformation of the Hamiltonian (1) which restores the conservation of quasimomentum  $\beta$  [24]. Close to the resonances, we have  $F(\epsilon, \beta, \eta) \approx |\sum_n J_n^2(N\phi_d) \exp(-i\Theta_n)|^2$ , where  $\Theta_n = \frac{\partial\theta_n}{\partial\epsilon}|\epsilon + \frac{\partial\theta_n}{\partial\beta}|\beta + \frac{\partial\theta_n}{\partial\eta}|\eta$  describes the effect of deviations from resonance on the coefficients  $c_n$ . Using a procedure detailed in Ref. [18], one can show that  $\frac{\partial\theta_n}{\partial\eta}|_{(\epsilon=\beta=\eta=0)} = \frac{\partial c_n}{\partial\eta}|_{(\epsilon=\beta=\eta=0)} = -4\pi n N^2/3$ , where we have kept terms in  $N^2$ . Finally we arrive at the fidelity in the presence of acceleration,

$$F(\eta, \epsilon = \beta = 0) = J_0^2\left(\frac{4\pi}{3}N^3\phi_d\eta\right). \quad (3)$$

Thus the width of such a peak centered at the resonant zero acceleration should drop as  $1/N^3$ . In order to verify the above result, the standing wave was accelerated during the application of the pulses. This acceleration was scanned

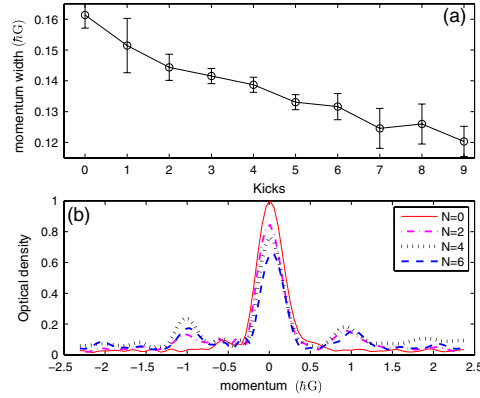


FIG. 4 (color online). (a) Momentum width of the reversed zeroth order state as a function of kick number. Error bars are an average over three experiments. (b) Optical density plots for the initial state [(red) solid curve] and kick numbers 2 [(magenta) dot-dashed curve], 4 [(black) dotted curve], and 6 [(blue) dashed curve] after summation of the time-of-flight image along the axis perpendicular to the standing wave.

across the resonant zero value and readings of the fidelity collected. Since a typical value of the half width at half maximum is  $\eta = 0.05$  for  $N = 4$  (corresponding to an acceleration of  $4 \text{ m/s}^2$ ), the perturbative treatment of acceleration on fidelity used above is justified. Figure 3(b) plots the experimental data for four to nine kicks, where the widths of the peaks decrease with a slope of  $-3.00 \pm 0.23$  in excellent agreement with the theory.

In conclusion, we performed experimental measurements of the fidelity widths of a  $\delta$ -kicked-rotor state near a quantum resonance. The width of these peaks centered at the Talbot time decreased at a rate of  $N^{-2.73}$  comparable to the predicted exponent of  $-3$ . By comparison, the mean energy widths were found to reduce only as  $N^{-1.93}$ . Furthermore, the fidelity peaks in momentum space changed as  $[N(N+1)]^{-0.92}$ , also consistent with theory. The reversal process used in the fidelity experiments led to a decrease in the momentum distribution of the final zeroth order state by  $\sim 25\%$  (for  $N = 9$ ) from the initial width. The sub-Fourier dependencies of the mean energy and fidelity observed here are characteristic of the dynamical quantum system that is the QDKR [18]. The narrower resonances of the fidelity scheme could be exploited in locating the resonance frequency with a resolution below the limit imposed by the Fourier relation. This can help determine the photon recoil frequency ( $\omega_r = E_r/\hbar$ ) which together with the photon wavelength enables measurement of the fine structure constant with a high degree of precision [15,17]. We also demonstrated a  $N^{-3}$  dependence of the resonance width in acceleration space in accordance with the extended theory. The sensitivity of an atom-inter-

ferometer-based gravimeter scales as the square of the loop time, hence the pursuit of large area interferometers to improve accuracy [14]. By comparison, the fidelity is responsive to the gravitational acceleration  $g$  with the cube of the “time”  $N$ , leading to the possibility of higher precision measurements. One could perform a fidelity measurement on a freely falling condensate exposed to kicks accelerating at the local value of  $g$  (to realize  $\eta \ll 1$ ). Variation in  $g$  would then manifest itself as a shift of the resonant acceleration. A parts per billion precision [14] would require a judicious selection of the parameters ( $N$ ,  $\phi_d$ ,  $T$ ), for instance ( $150, 10, 16T_{1/2}$ ). Such a resolution, though not feasible in the current setup without addressing stability-related issues, could be possible with future refinements.

This work was supported by the NSF under Grant No. PHY-0653494.

- [1] *Quantum Chaos, Between Order and Disorder*, edited by G. Casati and B. Chirikov (Cambridge University Press, Cambridge, 1995), and references therein.
- [2] F. L. Moore *et al.*, *Phys. Rev. Lett.* **73**, 2974 (1994).
- [3] J. Ringot *et al.*, *Phys. Rev. Lett.* **85**, 2741 (2000).
- [4] M. K. Oberthaler *et al.*, *Phys. Rev. Lett.* **83**, 4447 (1999).
- [5] G. Behinaein *et al.*, *Phys. Rev. Lett.* **97**, 244101 (2006).
- [6] M. Sadgrove *et al.*, *Eur. Phys. J. D* **45**, 229 (2007).
- [7] I. Dana *et al.*, *Phys. Rev. Lett.* **100**, 024103 (2008).
- [8] F. M. Izrailev, *Phys. Rep.* **196**, 299 (1990).
- [9] C. Ryu *et al.*, *Phys. Rev. Lett.* **96**, 160403 (2006).
- [10] S. Wimberger, I. Guarneri, and S. Fishman, *Phys. Rev. Lett.* **92**, 084102 (2004).
- [11] S. Wimberger *et al.*, *Nonlinearity* **16**, 1381 (2003).
- [12] P. Szriftgiser *et al.*, *Phys. Rev. Lett.* **89**, 224101 (2002).
- [13] *Atom Interferometry*, edited by P. R. Berman (Academic, San Diego, 1997).
- [14] J. M. McGuirk, M. J. Snadden, and M. A. Kasevich, *Phys. Rev. Lett.* **85**, 4498 (2000); K. J. Hughes, J. H. T. Burke, and C. A. Sackett, *Phys. Rev. Lett.* **102**, 150403 (2009); T. Lévêque *et al.*, *Phys. Rev. Lett.* **103**, 080405 (2009).
- [15] D. S. Weiss, B. C. Young, and S. Chu, *Phys. Rev. Lett.* **70**, 2706 (1993); M. Cadoret *et al.*, *Phys. Rev. Lett.* **101**, 230801 (2008).
- [16] J. B. Fixler *et al.*, *Science* **315**, 74 (2007).
- [17] A. Tonyushkin and M. Prentiss, *Phys. Rev. A* **78**, 053625 (2008).
- [18] P. McDowall *et al.*, *New J. Phys.* **11**, 123021 (2009).
- [19] M.-S. Chang *et al.*, *Phys. Rev. Lett.* **92**, 140403 (2004).
- [20] For our parameters, decoherence due to spontaneous emission is expected to be important beyond  $\sim 35$  kicks.
- [21] S. Wimberger *et al.*, *Phys. Rev. A* **71**, 053404 (2005).
- [22] J. Martin, B. Georgeot, and D. L. Shepelyansky, *Phys. Rev. Lett.* **100**, 044106 (2008).
- [23] J. Martin, B. Georgeot, and D. L. Shepelyansky, *Phys. Rev. Lett.* **101**, 074102 (2008).
- [24] S. Fishman, I. Guarneri, and L. Rebuzzini, *Phys. Rev. Lett.* **89**, 084101 (2002).

## VITA

Ishan Talukdar

Candidate for the Degree of

Doctor of Philosophy

Dissertation: TRANSPORT AND RESONANCES IN KICKED BOSE-EINSTEIN  
CONDENSATES

Major Field: Physics

Biographical:

Personal Data: Born in Dibrugarh, Assam, India on March 15, 1978, the son  
of Kanteswar and Mohini Talukdar.

Education:

Received the Bachelor of Science degree from University of Delhi, Delhi,  
India, 2001, in Physics

Received the Master of Science degree from University of Delhi, Delhi,  
India, 2003, in Physics

Received the Master of Science degree from Oklahoma State University,  
Stillwater, Oklahoma, USA, 2006, in Physics

Completed the requirements for the degree of Doctor of Philosophy with a  
major in Physics Oklahoma State University in December, 2010.

Name: Ishan Talukdar

Date of Degree: December, 2010

Institution: Oklahoma State University

Location: Stillwater, Oklahoma

Title of Study: TRANSPORT AND RESONANCES IN KICKED BOSE-EINSTEIN  
CONDENSATES

Pages in Study: 121

Candidate for the Degree of Doctor of Philosophy

Major Field: Physics

Scope and Method of Study: A purpose of this research was to study the scaling behavior of resonances of a periodically kicked quantum system. Specifically, a model known as a quantum  $\delta$ -kicked rotor (QDKR) was implemented with a  $^{87}\text{Rb}$  Bose-Einstein Condensate. Two variants of this system, a quantum  $\delta$ -kicked accelerator (QDKA) and a quantum ratchet, were also realized experimentally and used to study quantum transport. Furthermore, experiments were undertaken to introduce mean-field interactions in these systems through an Optical Feshbach resonance.

Findings and Conclusions: An overlap or fidelity measurement between a resonant and an off-resonant state of the QDKR yielded a scaling that was dependent on the cube of the measurement time, in units of kicks. Such a sub-Fourier behavior was also calculated to appear in the presence of an acceleration, and was verified experimentally. Quantum accelerator modes were observed in the QDKA and a detailed study of the parameter dependencies of three higher order resonances was done. The modes were explained with two models: a wavefront rephasing model and a quasi classical analysis. A quantum ratchet was realized at a QDKR resonance and the dependence of the directed momentum current on the momentum of the initial state investigated. Finally, photoassociation spectroscopy was performed on a  $^{87}\text{Rb}$  Bose-Einstein condensate for the  $1_g$  and  $0_g^-$  long range molecular states to realize an Optical Feshbach resonance.

Dr. Gil Summy

ADVISOR'S APPROVAL: \_\_\_\_\_